Theses and Dissertations

Spring 2019

Ship airwakes in waves and motions and effects on helicopter operation

Gregory M. Dooley
University of Iowa

Follow this and additional works at: https://ir.uiowa.edu/etd

Part of the Mechanical Engineering Commons

This thesis is available at Iowa Research Online: https://ir.uiowa.edu/etd/6727

Recommended Citation

Dooley, Gregory M.. "Ship airwakes in waves and motions and effects on helicopter operation." MS (Master of Science) thesis, University of Iowa, 2019.
https://doi.org/10.17077/etd.g8l4-38g6

SHIP AIRWAKES IN WAVES AND MOTIONS AND EFFECTS ON HELICOPTER
OPERATION

by

Gregory M. Dooley

A thesis submitted in partial fulfillment
of the requirements for the Master of Science
degree in Mechanical Engineering in the
Graduate College of
The University of Iowa

May 2019

Thesis Supervisors: Professor Pablo M. Carrica
Adjunct Assistant Professor Juan E. Martin

To my family.

ACKNOWLEDGEMENTS

I would like to thank my advisor Professor Carrica for giving me the opportunity to study such an interesting and dynamic topic. Also, thank you to Professor Carrica and Dr. Juan E. Martin for their immense guidance and support, which I believe greatly improved my overall contribution to this work. I would also like to acknowledge the US Office of Naval Research who provided the funding for this research.

Thank you to the faculty and my fellow students in the Mechanical Engineering Department at the University of Iowa for all the academic support and knowledge I have gained during my time here. Also, thank you to my family who have been nothing but supportive and encouraging during my academic career.

ABSTRACT

This thesis focuses on the effects of wave-induced motions on the airwake of a ship and on the operation of a helicopter in the airwake. While the topic is broad, efforts are concentrated on understanding fundamentals of the ship's airwake structure at varying Reynolds (Re) numbers without motions, using available experimental data for validation of the computational fluid dynamics (CFD) methodology used, and on studying the effects of waves and motions on the airwake of a ship and a helicopter operating above a ship's flight deck in full-scale. The static ONR Tumblehome (ONRT) ship geometry with a solid boundary representative of the free surface is simulated at three different Re numbers, $3.2x10^4$, $1x10^6$, and $1.3x10^8$. Validation is performed against experimental measurements at model-scale Re=$1x10^6$. Full-scale simulations of the ONRT are carried out in head winds and regular waves approximately equivalent to conditions seen at sea states 3 and 6. Effects of waves and motions are isolated for both sea states using simulations with combinations of waves and motions, waves and no motions, no waves with motions, and no motions or waves. A triple velocity decomposition is conducted in order to quantify changes in the airwake due to motions and waves. The operation of rotorcraft in the ONRT airwake is analyzed using one-way and two-way coupling approaches. The one-way coupling approach uses the velocity field data from the full-scale ONRT simulations and disk actuator theory to calculate thrust fluctuations for three different rotor sizes. The results of the one-way coupling approach show that the smallest rotor is much more affected by small scale turbulence, while small scale fluctuations are filtered out by larger rotor diameters. In the two-way coupling approach, a helicopter based on the Sikorsky SH-60 hovering above the flight deck is simulated, including explicitly moving grids to discretize the main rotor, tail rotor, and fuselage. This method captures the effects of the interaction between the rotor downwash and the

ONRT airwake. The study shows that for the mild conditions of sea state 3 the motions have little effect on the airwake behavior. At sea state 6 the airwake behavior is significantly altered, which is reflected in the resulting forces on the helicopter body operating in this condition.

PUBLIC ABSTRACT

This thesis focuses on the effects of wave-induced motions on the airwake of a ship and on the operation of a helicopter in the airwake. While the topic is broad, efforts are concentrated on understanding fundamentals of the ship's airwake structure at varying scales without motions, using available experimental data for validation of the computational fluid dynamics methodology used, and on studying the effects of waves and motions on the airwake of a ship and a helicopter operating above a ship's flight deck in full-scale. The static ONR Tumblehome (ONRT) ship geometry with a solid boundary representative of the free surface is simulated at three different scales. Full-scale simulations of the ONRT are carried out in head winds and regular waves. The operation of rotorcraft in the ONRT airwake is analyzed using one-way and two-way coupling approaches. The one-way coupling approach uses the velocity field data from the full-scale ONRT simulations and disk actuator theory to calculate thrust fluctuations for three different rotor sizes. The results of the one-way coupling approach show that the smallest rotor is much more affected by small scale turbulence, while small scale fluctuations are filtered out by larger rotor diameters. In the two-way coupling approach, a helicopter hovering above the flight deck is simulated. The study shows that for the mild conditions the motions have little effect on the airwake behavior. Higher amplitude waves significantly alter the airwake behavior, which is reflected in the resulting forces on the helicopter body operating in this condition.

TABLE OF CONTENTS

LIST OF TABLES

LIST OF FIGURES

x

xiii

Chapter 1. INTRODUCTION & LITERATURE REVIEW

1.1 Introduction & Motivation

Today flight operations behind a ship are common place, making the study of ship airwake behavior of greater importance. Aircraft typically operate in the region behind the superstructure of a ship during launch and recovery operations, which may result in elevated levels of airflow instabilities due to the interaction between a ship's superstructure and the surrounding airflow. These flow instabilities may result in dangerous flight conditions and an increase in pilot workload. The operation of aircraft in the region near the ship is known as the dynamic interface (DI) and is characterized by time dependent velocity fluctuations and gradients induced by the interaction between the ship's geometry and surrounding airflow. Currently, at sea trials are used to test the DI and determine safe operating envelopes for a specific ship and aircraft. The DI is ship and aircraft dependent and heavily influenced by the ship geometry resulting in a different DI for all ships with at sea flight operations. Larger rotor craft operating in a region close to the ship have the ability to modify the airwake and thus the DI. The objective of this work is to enhance our knowledge of the aerodynamic interactions between ship and aircraft. This information can then be used to make informed decisions about the quantitative implementation of the dynamic interface in pilot simulators with the goal of providing more realistic training conditions and ultimately improving real world safety.

The ship motions and operating conditions (wind-over-deck and seas) are the main contributors to the airwake behavior as well as aircraft performance (aerodynamics and lift induced flow) when considering the coupling between the ship airwake and aircraft wake. Full-scale at-sea trials would be able to include all these factors but are difficult to control/characterize, might not cover all conditions of interest, and are also inherently expensive

1

to conduct. Model-scale experiments may experience scaling effects and typically ignore the interaction between ship motions and aerodynamics. This leads to an opportunity for high fidelity, full-scale computational fluid dynamics (CFD) simulations to offer a cost-effective alternative to physical experiments. CFD offers the capability to conduct a basic analysis of all the aerodynamic drivers mentioned as well as use the data to develop reduced order models to simplify the modeling process and reduce computational expense.

1.2 Literature Review

1.2.1 Analysis of the airwake

Much effort has been focused on the analysis of the airwake for static ships using both computational and experimental methods at model- and full-scales. Polsky (2002) studied the effect of Reynolds number on the flow field of an LHA-class US Navy ship and was able to conclude that results could be scaled linearly for a range of Reynolds numbers at the same wind angle with some Reynolds dependence seen in the frequency content of the two cases studied. However, the study range of Reynolds numbers is much smaller than what is typically done when going from model- to full-scale experiments or simulations. Buchholz et al. (2018) used the ONRT geometry to study the effect of Reynolds number on the flow over the deck. The work identified robust structures at low Reynolds numbers that are maintained at larger model- and full-scale Reynolds numbers. While the underlying structures were robust, changes in the relative strength of the vortical structure was also observed. Polsky et al. (2007) used the Navier-Stokes solver Cobalt to analyze the flow field over the landing deck of a US Navy DDG Arleigh Burke Class Flight II-A destroyer. Initial results showed the effect the proximity to the upstream and downstream boundary have with CFD consistently predicting high speed flow on the port side of the ship which was resolved by moving the upstream Riemann invariant boundary condition one

2

ground board length away. Overall, the CFD simulations agree well with the wind tunnel data with an error of 3.5-10% for different angles of attack. Many computational studies have been done investigating the airwake of the simple frigate shape (SFS2). Forrest & Owen (2010) used detached eddy simulations (DES) to simulate wind tunnel experiments done by the National Research Council of Canada. The study showed that DES is capable of resolving the dominant flow features found in the region of the flight deck by experimentation. The DES simulations were also capable of matching the shedding frequencies and turbulent power measured in the wind tunnel experiments. A more recent study done by Sydney et al. (2016) used particle image velocimetry (PIV) to analyze the turbulent flow of the SFS2 airwake. The study showed that each of the backward facing steps generated a shear layer as well as a region of recirculation which has significant three-dimensional variations. Also shown is the effect of upstream turbulence on the flow over the flight deck with the forward-facing step of the SFS2 creating the highest magnitude of turbulent kinetic energy and is carried into the flight deck region. Li et al. (2016) also used the SFS2 geometry and wind tunnel data to compare the capabilities of DES and LES models to simulate the airwake. It was concluded that both DES and LES are superior to RANS and that DES is capable of accurately modeling the flow separation seen in experiments at a reduced computational cost to LES.

Less work has been done to investigate the effects of ships motions on the airwake behavior. The Australian DSTO (Arney 1994a, 1994b) conducted field campaigns in order measure ship motions and the airwake over the flight deck for multiple wind-over-deck velocities. The data gathered was to be used to update the condition of a simulation model used to model the dynamic interface between a helicopter and ship. Recent experiments by Sydney et al. (2017) studied how ship orientation and motions affect the airwake of the SFS2. The study

3

showed that motion-induced flow altered the distribution of turbulence over the flight deck and that the orientation (pitch) significantly modified the size of the downstream airwake.

1.2.2 Helicopter in airwake

Coupling ship airwakes and helicopters can be done in a one-way or two-way coupling approach. One-way coupling uses a helicopter model that is subject to the velocity fields obtained from airwake simulations that do not include the helicopter. Two-way coupling approaches include the ship and helicopter in the same simulation and resolve the interaction between the ship airwake and the helicopter induced flow. Crozon et al. (2014) evaluated a superposition approach which linearly adds the flow field fluctuations for a ship and actuator disk in forward motion separately. This is still considered a one-way coupling approach as the ship and helicopter model are simulated separately. The superposition method resulted in an over prediction of rotor inflow velocity by 50% and stronger rotor tip vortices in comparison to the same actuator disk model operating in the flight deck region. Both actuator disk approaches were then compared to two-way coupling with the same ship and actuator disk model simulated together. It was found that for a rotor operating in close proximity to a ship a two-way coupling approach it is necessary to accurately resolve the coupling effects between the rotor and ship airwake. Forsythe et al. (2018) used the CFD code Kestrel along with the Navy's simulation tool CASTLE to simulate a UH-60 landing on a ship which includes rotor model (blade element) and ship effects (i.e. two-way coupling). The simulation consists of a guided-missile frigate in 25 knots head winds with the UH-60 approaching from a ¼ mile away and landing on the flight deck of the ship. It was observed during the landing process structures generated by the ship's superstructure are ingested into the front of the rotor. One-way and two-way coupling approaches were conducted, oscillations of ±1 degree in pitch and roll were seen for the two-way

4

coupling that were not seen in the one-way coupling when the helicopter was hovering above the flight deck. Thedin et al. (2018) used a one-way coupling approach to model the flight dynamics of a UH-60 Black Hawk helicopter operating in the airwake of SFS2 and a realistic atmospheric boundary layer (ABL). The helicopter flight dynamics were resolved using the flight simulation code GENHEL-PSU and both approach/landing and hovering scenarios were simulated. It was found that ABL fluctuation can increase pilot workload during these scenarios.

Limited work has been completed that directly simulates a helicopter rotor operating in a ship airwake. Crozon et al. (2014) simulated a five-bladed Sea King rotor operating in the airwake of a Canadian Patrol Frigate (CPF) to compute the loads and compare the results to the actuator disk simulation discussed previously. It was found that the collective actuation needs to increase 20% to maintain the thrust due to the increased inflow and cyclic changes of 7% are also needed when operating over the flight deck. In a more recent publication Crozon et al. (2018) simulated a full discretized Sea King helicopter, including tail rotor and fuselage, along with an autopilot to compute a landing maneuver over the flight deck of a CPF. This is the first computation of a fully coupled CFD of the dynamic interface between a ship and helicopter. The resulting autopilot activity and trajectory of the helicopter suggest that the airwake does influence the helicopter.

1.3 Summary of Work

The purpose of this study is to characterize the flow over the ONR Tumblehome (ONRT) and quantify the effects of wave-induced motions, in addition to the resulting forces on a generic helicopter operating over the flight deck. In Chapter 3, static, single-phase model-scale simulations are used to validate the CFD solver. Experimental data collected in a water channel is used for comparison and a grid study, consisting of three different levels of refinement, was

5

completed. Grid dependence is investigated by analyzing reattachment points in multiple regions of flow separation. The experimental results presented in this chapter were completed by Austin Krebill and Prof. James Buchholz at the University of Iowa. For information on the experimental methods used refer to Buchholz et al. (2018) and Dooley et al. (2019). The static simulations are also used to characterize the flow for a range of Reynolds numbers. Low Reynolds number analysis allows for the identification of structures at higher Reynolds numbers where increased turbulence obscures larger robust structures.

In order to achieve the overall goal of quantifying the effects of flow non-linearities generated through the interaction between waves and motions, full-scale, two-phase flow simulations are performed. The contributions of motions and waves are studied separately by comparing the flow fields of simulations with motions and waves, with motions and no waves, without motions and with waves, and without motions and waves. The effects of motions and waves are then quantified using ensemble averaging and a triple velocity decomposition. Two different sea states (SS) with corresponding wind speeds are studied, SS3 and SS6, in order to measure the effects of varying conditions. All the results decomposing the ONRT airwake are presented in Chapter 4.

In Chapter 5, the resulting forces on a helicopter operating in the airwake of the ONRT are studied using one-way and two-way coupling approaches. One-way coupling is used to analyze the thrust response of three different rotor sizes operating above the flight deck. The one-way coupling approach uses the flow field data from the full-scale, two-phase simulations presented in Chapter 4 in order to calculate the predicted thrust of a characterized rotor operating in a given location. The two-way coupled simulations are performed using a fully discretized generic helicopter, main and tail rotors included, hovering over the flight deck of the ONRT

www.manaraa.com

advancing in waves. These simulations resolve the interaction between the rotor downwash and the airwake of the ship.

Chapter 2. NUMERICAL METHODS

All simulations are performed using the general purpose CFD code REX. REX is an unsteady Reynolds-Averaged Navier-Stokes (URANS) or detached eddy simulation/delayed eddy simulation (DES/DDES) solver, which is being continually developed by Pablo Carrica's research group at the University of Iowa.

The full system of nonlinear governing equations is solved using a partitioned approach in which each variable is solved consecutively at each time step in the following order: liquid turbulence, level-set, liquid momentum and pressure to convergence, then air turbulence, and air momentum/pressure (Li & Carrica 2018). All the equations are non-dimensionalized using a using a reference velocity U_o (e.g. ship speed, free stream velocity, etc.) and a characteristic length L (e.g. ship length, rotor diameter, etc.). The subscript "0" represents the absolute dimensional value of any property. Both the air and water are treated as incompressible and the mass and momentum conservation are preserved using Equations (1) and (2), respectively.

$$\nabla \cdot U = 0 \tag{1}$$

$$\frac{\partial(\rho_f U)}{\partial t} + \nabla \cdot (\rho_f U U) = -\nabla \hat{p} + \nabla \cdot \left[Re_{eff,f}^{-1} (\nabla U + \nabla U^T) \right] \tag{2}$$

where:

$f = w$ or $f = a$ indicates water or air

$\hat{p} = p + \frac{\rho_f z}{Fr^2} + \frac{2}{3}\rho_f k$ is the dimensionless piezometric pressure

$p = \frac{p_{abs}}{\rho_{o,f} U_o^2}$ is the dimensionless pressure

$\rho_f = \frac{\rho_{f,abs}}{\rho_{0,w}}$ is the dimensionless density ($\rho_w = 1$)

$Re_f = \frac{\rho_{0,f} U_0 L}{\mu_{0,f}}$ is the Reynolds number of fluid f

$Re_{eff,f}^{-1} = \frac{1}{Re_f} + \nu_t$ is the effective Reynolds number

ν_t is the turbulent viscosity obtained from a turbulence model

$Fr = \frac{U_{ship}}{\sqrt{gL}}$ is the Froude number (calculated using U_{ship} as it only applies to the water side)

The governing equations are discretized using a control volume/finite difference approach on a collocated grid in space. The convective terms are discretized using a linear upwind scheme which is fourth-order accurate except in the near wall regions where it is second-order accurate. Diffusion and temporal terms are discretized using second-order central difference and second-order backwards Euler schemes, respectively.

Turbulence is modeled and the turbulent kinetic energy ν_t is resolved in each phase using a DDES model based on Menter's shear transport two-equation model (Menter 1994). In this model the turbulent kinetic energy k and the specific dissipation rate ω are solved and RANS and LES (large eddy simulation) regions of the flow are determined based on the size of the grid spacing with respect to the modeled scale of the turbulence. RANS modeling is done using Menter's blended k-ε/k-ω approach where the blending function works to apply the k-ε model in the near-wall wall region and then systematically switches to the k-ω model in the wake region in order to take advantage of each model's strengths (Menter 1994). In regions of large flow separation where the length scale of turbulence containing energy increases LES is used. For a more complete explanation of the turbulence modeling techniques implemented in REX please refer to Xing et al. (2010), Li et al. (2018), and Martin et al. (2018).

REX uses an unsteady single-phase level set approach to model free surface flows. The single-phase level set function used by REX to resolve the location of the free surface is:

$$\frac{\partial \phi}{\partial t} + \mathbf{v} \cdot \nabla \phi = 0 \tag{3}$$

where ϕ is the distance to the interface function which is positive in water and negative in air. Two phase air/water flow is resolved in a semi-coupled fashion with the water solution ignoring the air using zero-shear and atmospheric pressure conditions while the air solver uses the water solution as an immersed boundary to enforce a no-slip condition at the free surface. This approach is not intended to be used for problems where it is important to resolve the stress induced by the air on the water surface (i.e. wind-induced wave generation). For a full description of the single-phase level set approach refer to Carrica et al. (2007a).

Waves are imposed explicitly as initial and inlet boundary conditions in water (Carrica et al. 2007b),

$$\phi(x, y, z, t) = a\cos(kx - 2\pi ft) - z(x, y) \tag{4}$$

$$U(x, y, z, t) = U_0 + \frac{a}{Fr^2}\sqrt{k}e^{kz}\cos(kx - 2\pi ft) \tag{5}$$

$$W(x, y, z, t) = \frac{a}{Fr}\sqrt{k}e^{kz}\sin(kx - 2\pi ft) \tag{6}$$

$$p(x, y, z, t) = \frac{a}{Fr^2}e^{kz}[\cos(kx_{2\pi ft}) - \frac{1}{2}\frac{a}{k}e^{kz} \tag{7}$$

where:

$k = \frac{2\pi}{\lambda}$ is the wavenumber

$f = \frac{1}{\lambda} + \frac{1}{Fr\sqrt{2\pi\lambda}}$ is the encounter frequency

REX uses multiblock curvilinear structured body-fitted grids with dynamic overset capabilities which allows for local refinement where needed. Dynamic overset capabilities allow for the computations of large-scale motions. Grid overlap and domain connectivity information (DCI) is computed by the codes Suggar or Suggar++ (Noack & Boger, 2009). Parallel processing

10

is done using MPI-based domain decomposition, each grid can be split into multiple blocks based on user directives and each block is assigned a processor.

REX allows for either prescribed or predicted motions in all six degrees of freedom. Ship motions are predicted using an implicit approach with a hierarchy of bodies, as described in Carrica et al. (2007b, 2010). The earth fixed coordinate system is used as an inertial reference frame in which the fluid motion equations are computed. A non-inertial coordinate system is attached to each body based on its principal axes of inertia in which the rigid body equations are solved. Forces and moments on the bodies are originally computed in the same reference system of the fluid motion equations and then projected into the ship coordinate system. For cases where overlapping grids are used to define the geometry's surfaces, USURP is used to calculate the weights for each grid point to be used when integrating the forces on the body (Boger & Dreyer 2006).

For post-processing, Q-criterion is used to visualize the vortical structures generated in the simulated flow. The Q-criterion is defined as the regions of flow where the vorticity magnitude is greater than that of the rate-of-strain tensor (Hunt et al. 1988). The D-criterion is also used to visualize structures, which uses iso-surfaces to approximate tubes with equal distance to the vortex core (Carrica & Li 2017).

11

Chapter 3. STRUCTURE OF SHIP AIRWAKE

3.1 Simulation Design and Setup

3.1.1 Simulation setup

The airwake of the static ONRT geometry is resolved for a range of Reynolds numbers with a solid boundary at the waterline, representative of the free surface. This geometry is the same as the full ship geometry discussed further in §4.1.1, however, with only the air side being modeled. The two lower Reynolds numbers, $3.2\text{x}10^4$ and $1\text{x}10^6$, are representative of model-scale experiments and $Re=1.3\text{x}10^8$ corresponds to a full-scale prototype geometry. All Reynolds numbers studied were simulated with at least two different grids with systematic levels of refinement. For the intermediate Reynolds number ($Re=1\text{x}10^6$) a third intermediate grid was included to conduct a grid study. The complete simulation matrix can be seen in Table 1. The grid structure is the same throughout and is refined by a factor of $\sqrt{2}$ in each direction for each level of refinement. The wall spacing is such that $y^+ < 1$ for the coarse grid at the intermediate Reynolds number. Based on this the wall spacing for all the grids at the $3.2\text{x}10^4$ and $1\text{x}10^6$ Reynolds numbers satisfy the $y^+ < 1$ condition. Since the same grids are used for the full-scale simulations ($Re = 1.3\text{x}10^8$), a three-zone wall function is used resulting in wall spacing in the range $20 < y^+ < 40$ for the three different grids used (Bhushan et al. 2009). The dimensionless time step is adjusted based on grid refinement. In order to achieve a CFL=$U\Delta t/\Delta x \leq 1$ the dimensionless time steps were set based on the free stream velocity ($U=1$) and the grid spacing in the airwake region for each of the three grids.

Table 1: Simulation matrix.

Grid	Size	$\Delta t^* (L/U_o)$	Reynolds number
Coarse	19M	1×10^{-3}	3.2×10^4
			1×10^6
			1.3×10^8
Medium	54M	7.07×10^{-4}	1×10^6
Fine	154M	5×10^{-4}	3.2×10^4
			1×10^6
			1.3×10^8

3.1.2 Grid design
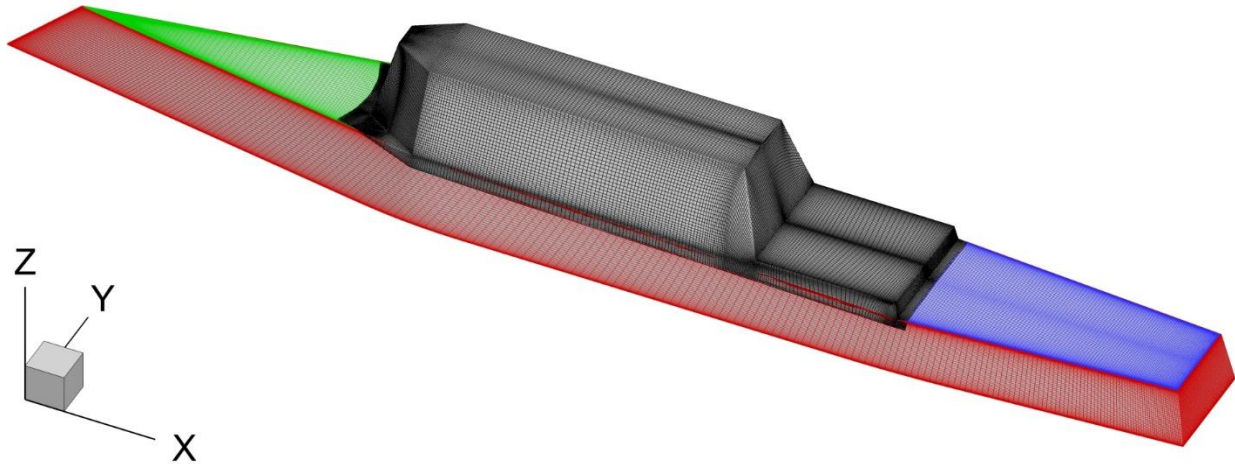
Figure 1: Overset grid topology (coarse) for static single-phase simulations.

The ONRT grid system for the static, single-phase simulations consists of six structured blocks, including: four different body fitted grids covering the hull and superstructure, one Cartesian airwake refinement, and one Cartesian background grid. The topology of the body fitted grids is shown in Figure 1. Table 2 includes all the dimensions for the fine grid system, notice that majority of the points are clustered in the airwake refinement grid as this is the main area of interest and turbulent flow. The Cartesian background grid is significantly coarser than the airwake refinement as flow upstream of the ship is mostly uniform and flow further downstream of the stern of the ship is not of interest for this study. The Cartesian airwake refinement and background grid, shown in Figure 2, maintain the same wall spacing discussed in §3.1.1 at the solid boundary ($z=0$) plane in order to resolve the development of the boundary

13

layer; this is similar to the experimental setup which includes a base plane. The inlet and exit

boundary conditions are imposed in the background grid and are located one ship length from the

bow and stern of the ship, respectively.

Table 2: Fine grid system used for all static single-phase simulations.

Grid	Dimensions	Size
Hull	1201 x 101 x 121	14.7M
Bow	241 x 101 x 121	2.9M
Stern	241 x 51 x 181	2.2M
Superstructure	631 x 51 x 337	10.8M
Airwake Refinement	1201 x 361 x 251	108.8M
Background	301 x 181 x 151	8.2M
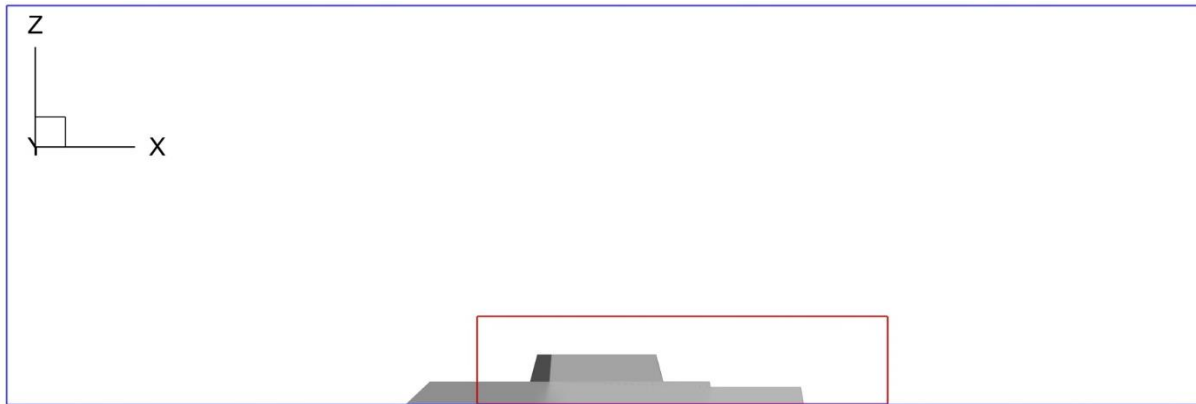
Figure 2: Location of background (blue) and airwake refinement (red) Cartesian grids.

3.2 Reynolds Number Analysis

3.2.1 Low Reynolds number dye visualization

Low Reynolds number results are presented first to describe the salient flow features of

the ONRT airwake. As it is discussed in the following sections, the flow structures observed at

this condition change as the Re increases; however, the visualization at low Re allows for a

general understanding of the flow that is minimally affected by turbulence. Prior to the

description of the dye visualization results, an overview of the mean flow based on CFD results

is presented in Figure 3. The general velocity profile in the symmetry plane and a horizontal

plane at mid-height of the superstructure show multiple regions of detached flow. Each upstream

14

detached zone (at the junction of the bow and the superstructure; above and to the sides of the superstructure) results in the periodical shedding of vortices that as are transported downstream and interact creating even more complex structures. The boundary layers (BL) over the superstructure reattaches at approximately one third of the superstructure length; it is found that the reattachment distance becomes shorter as Re increases. Iso-lines for $|u| = 0.9U$ that is, 90% of the freestream velocity, show that the thickness of the BLs continue to decrease before reaching its downstream back face, where they become separated again. The recirculation region behind the superstructure is complex as it combines the effects of a three-dimensional backward facing step with additional steps downstream, as well as other flow features originating in the flared geometry of the ship bow and sides. An example of the complexity of the flow is the expansion of the recirculating region shown in Figure 3 at the second backward facing step (hangar). The bottom panels in Figure 3 show several streamlines for the mean flow originating from approximately the centerplane upstream of the model. The counter rotating streamwise vortices are generated at the edge joining the bow and hull and at the intersection of the superstructure and bow. These vortices span the length of the ship and remain outside of the recirculation zone behind the superstructure. The low-pressure zone behind the superstructure results in the low speed flow near the boundary layer of the ship being pulled in the recirculation region. Streamlines show that the secondary back step results in the formation of new streamwise vortices that extend the length of the flight deck.

15
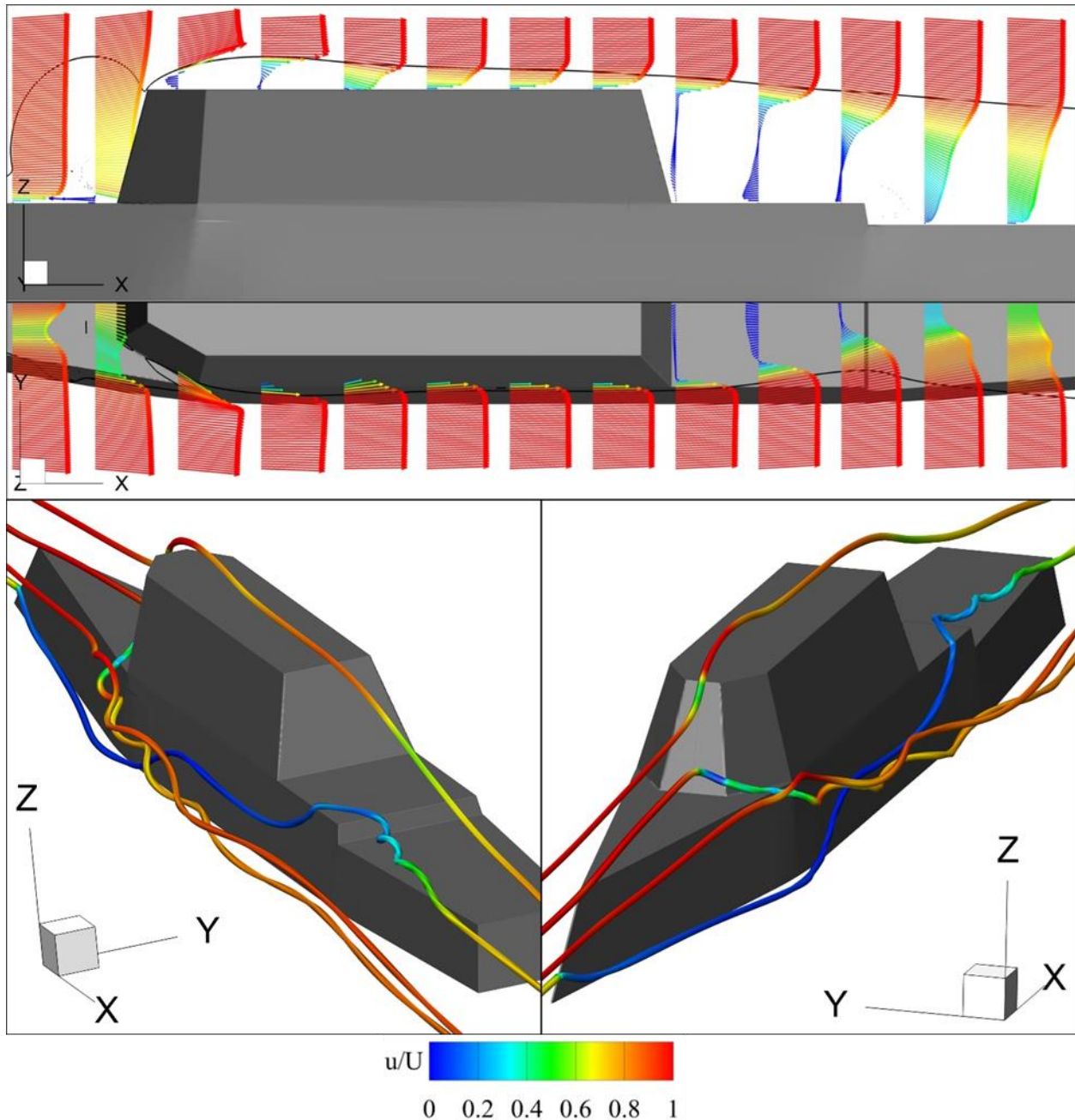
Figure 3: Mean flow at Re = 3.2×10^4. Top: center plane velocity field; Center: z/L = 0.07 plane (approximately mid superstructure height); Bottom panels show two views of instantaneous streamlines originating from approximately the centerplane upstream of the model.

Figure 4 contains low Re dye visualizations of the wake and CFD results (fine grid) of

the instantaneous flow field shown by iso-surfaces of Q-criterion. Q-criterion is used to try and

compare the structures resolved using CFD to the dye visualization, where dye is dissolving from

the front facet and both bow edges. The dye visualization results show hairpin vortices being

16

periodically shed from the separated region on top of the superstructure which traverse the centerline of the ship. These vortices are resolved in the CFD solutions but dissipate faster in the streamwise direction. It is possible that the hairpin vortices seen traveling all the way to the flight deck region in the experimental results no longer maintain significant energy and are simply remnant dye structures being convected downstream. This would explain why CFD does not show them traveling as far downstream, however numerical dissipation is also a possibility. Hairpin vortices are also periodically shed from the separated region where the front facets meet the sides of the superstructure. These vortices travel low length of the superstructure and then are pulled into the low-pressure region behind the superstructure and have the potential to affect the flow dynamics in this region. CFD resolves these vortices along the sides of the superstructure with other smaller scale structures being shed as well.
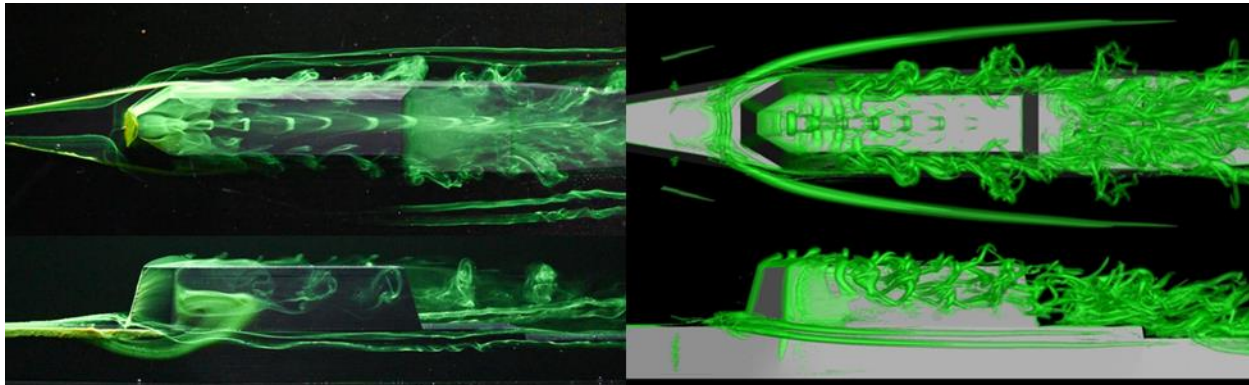
Figure 4: Dye visualization (experimental, left) and Q-criterion iso-surfaces (CFD, right), for Re $= 3.2 \times 10^4$.

3.2.2 Reynolds number dependence

Three different Reynolds numbers were simulated in order to analyze the effect it has on the flow structures and determine to what degree low/moderate Re number simulations and experiments can be used to model full-scale flow structures. Figure 5 shows that instantaneous flow structures increase in complexity as Re number increases. The characteristic hairpin vortices along the sides of the superstructure for the low Re number (Re=3.2×10^4) are no longer

17

present at the highest Re number (Re=1.3x10^8). It was found that the separation bubble in this region contracts as Re number increases and results in the disappearance of the hairpin vortices in this region, shown in Figure 6. Separated flow on the top of the superstructure shows the same behavior with the detached region contracting as Re number increases. At the higher Re numbers the overall strength of the adverse pressure gradient increases but the size of the low-pressure, detached zone decreases. The necklace vortices generated at the bow and front of the superstructure can be seen throughout all Re number solutions but do decay much faster for the higher Re number cases. The breakdown of these structures results in the loss of them in the mean flow solution; the grid dependence of this break down is discussed in the next section. Coherent structures seen in the flight deck region for the low Re number case are no longer distinguishable for the higher Re cases due to the introduction of smaller scale, broadband structures, showcasing the advantages of using low Re simulations for identifying larger robust structures.
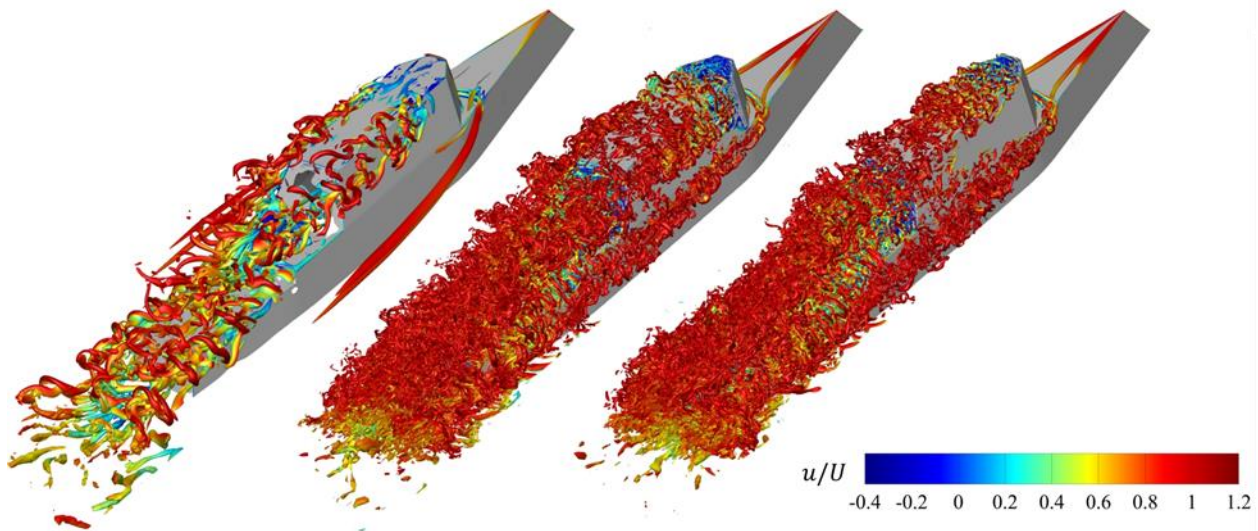
Figure 5: Iso-surfaces of D-criterion 0.001 for Re of 3.2x10^4 (left), 1x10^6 (middle), and 1.3x10^8 (right) colored by streamwise velocity using the fine grid.

18
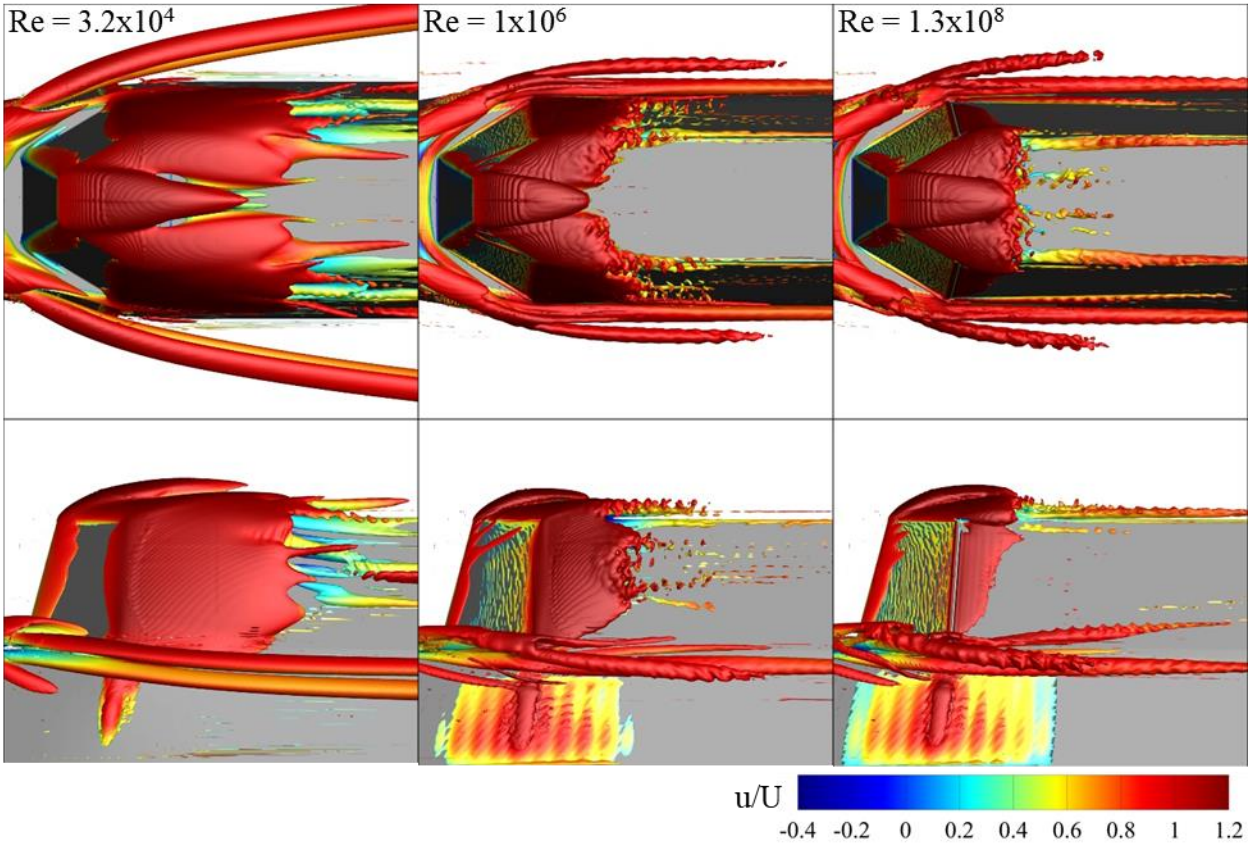
Figure 6: Iso-surfaces of Q-criterion colored by average streamwise velocity for three different Re numbers (3.2×10^4, 1×10^6, and 1.3×10^8) at the front of the superstructure.

Figure 7 shows the mean and RMS fluctuations of velocity in the streamwise and vertical direction in the centerplane of the flight deck region. The shear layer shed from the top of the superstructure can be seen in the streamwise velocity profile extending into the flight deck region for all Re numbers. The flow reattachment point can be seen extending much further down the flight deck for the low Re case, with the point moving closer to the second back facing step as Re increases. There is also an additional reattachment point from the second back facing step for the higher Re solutions. It can be seen that the transition between the low speed flow of the shear layer and free stream velocity is much more gradual for the low Re case. This is also shown in the vertical direction as the downward flow of the recirculation zone behind the superstructure extends further into the flight deck region for the low Re case. The overall strength of the

19

recirculation zone can be seen increasing for the higher Re number cases as the high vertical

velocity flow along the back-facing step increases from $0.1U$ (Re=3.2x10^4) to $0.2U$

(Re=1x10^6/1.3x10^8). Overall, the intermediate Re and high Re number cases are very similar in

mean flow behavior in this region. Significant increases in RMS of streamwise and vertical

velocity fluctuations can be seen for the higher Re cases, especially in the region directly behind

the superstructure. Increases from $0.15U$ for the low Re case to >$0.2U$ for the higher Re cases

can be seen in both directions. It should be noted that the mean flow field and magnitude of

fluctuations become more similar across all Reynolds numbers farther down the flight deck,

which is important as it is the main area of interest for flight operations.
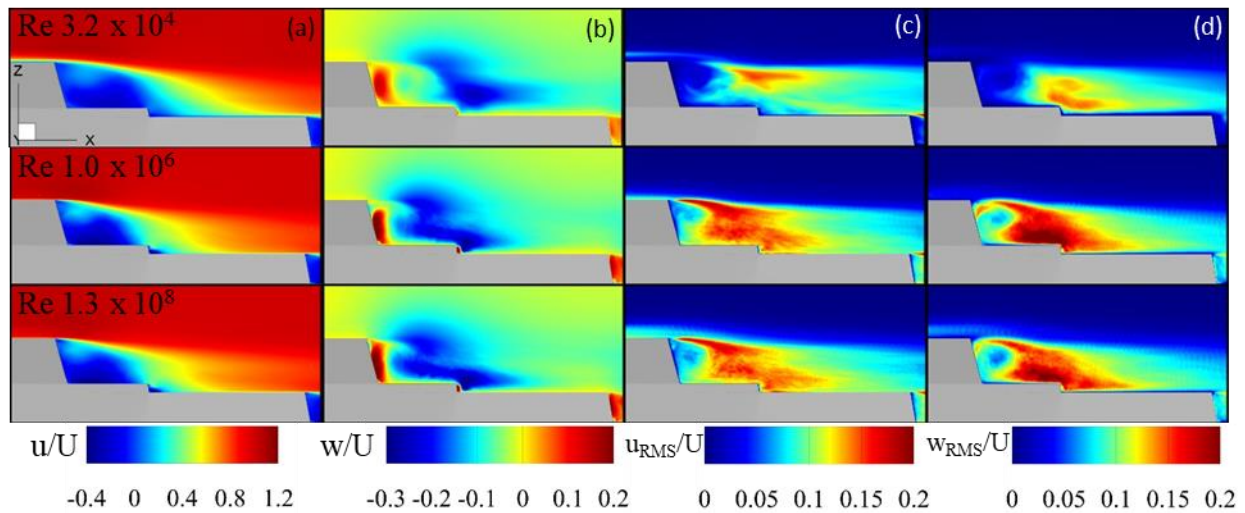
Figure 7: Mean streamwise (a) and vertical (b) velocity and RMS of velocity fluctuations for streamwise (c) and vertical (d) directions for three different Reynolds numbers. Results shown from fine grid.

Line plots of the results shown in Figure 7 for two different locations along the back deck

are shown in Figure 8. The point x/L=0.708 is approximately located at the midpoint between the

back of the superstructure and the second back facing step and the x/L=0.883 point is near the

midpoint between the second back facing step and the stern of the ship (i.e. center of flight deck).

Velocity and RMS of velocity fluctuations profiles at x/L=0.708 show that the low Re simulation

20

differs significantly from the model-scale and full-scale Re number simulations in the recirculation region behind the superstructure. The increase in RMS of velocity fluctuations seen at z/L=0.12-0.15 for the full-scale Re is due to the high level of RMS generated at the front of the superstructure being convected into the flight deck region, this is similar to the results reported in Sydney et al. (2016). At x/L=0.883 the low Re simulation still shows differences in the streamwise velocity profile with a larger boundary layer and the negative vertical velocity is about -0.03U larger in the region close to the flight deck. The RMS of velocity fluctuations match very well across all Re numbers at this location, with only slight difference seen in the boundary layer region and the shear layer region where flow transitions in to the free stream.
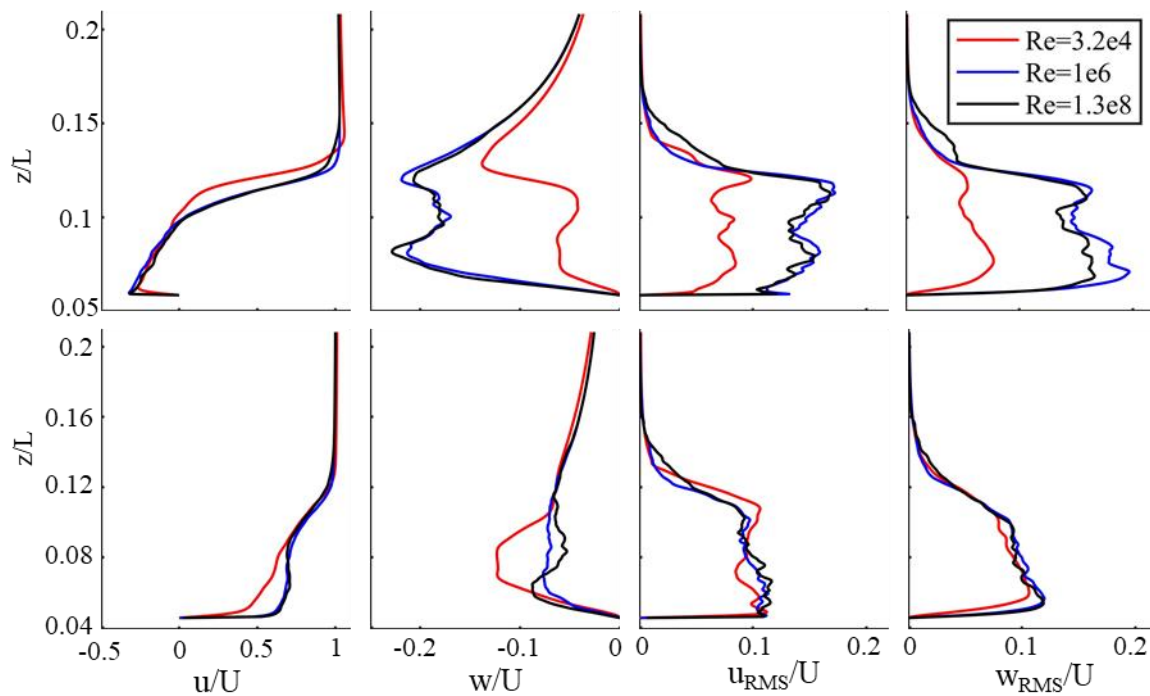
Figure 8: Line plots of mean velocities and RMS of velocity fluctuations from the fine grid for three different Re numbers (3.2x10^4, 1x10^6, and 1.3x10^8). Top x/L = 0.708; Bottom x/L = 0.883.

3.3 Grid Dependence

3.3.1 Mean flow

The mean flow field was obtained by averaging solutions over an integer number of ship lengths traveled by a moving fluid particle. This is obtained by using the inverse of the non-dimensional time step ($t^* = t\frac{L}{U}$) to get the number of time steps per ship length traveled. Five, seven, and nine ship lengths were used for the coarse, medium, and fine grid averages, respectively. The frequency at which volume solutions were saved was adjusted so that each of the simulations with different levels of grid refinement saved the same number of solutions (100) per ship length traveled by a fluid particle. Figures 9 and 10 show the mean flow structures of the three different Re numbers tested for two different grid sizes using the Q-criterion. Overall, the coarse and fine solutions for Re=3.2x10^4 are very similar with slight differences seen in the recirculation zone behind the superstructure and the separated region at the front of the superstructure. The pair of coherent streamwise necklace vortices generated at front of the ship are still prevalent in all the averages but the effect of resolved smaller scale structures in the fine grids is shown. At Re=1x10^6 and 1.3x10^8 the necklace vortices break down quickly and are no longer present in the region near the back deck. Instantaneous solutions at these Re numbers for the coarse grid show two strong coherent necklace vortices traversing the length of the ship as opposed to what is shown in Figure 5. The same behavior is observed in the two V-shaped streamwise vortices generated over the flight deck of the ship and in the shear layers generated off the sides and top of the back face of the superstructure.
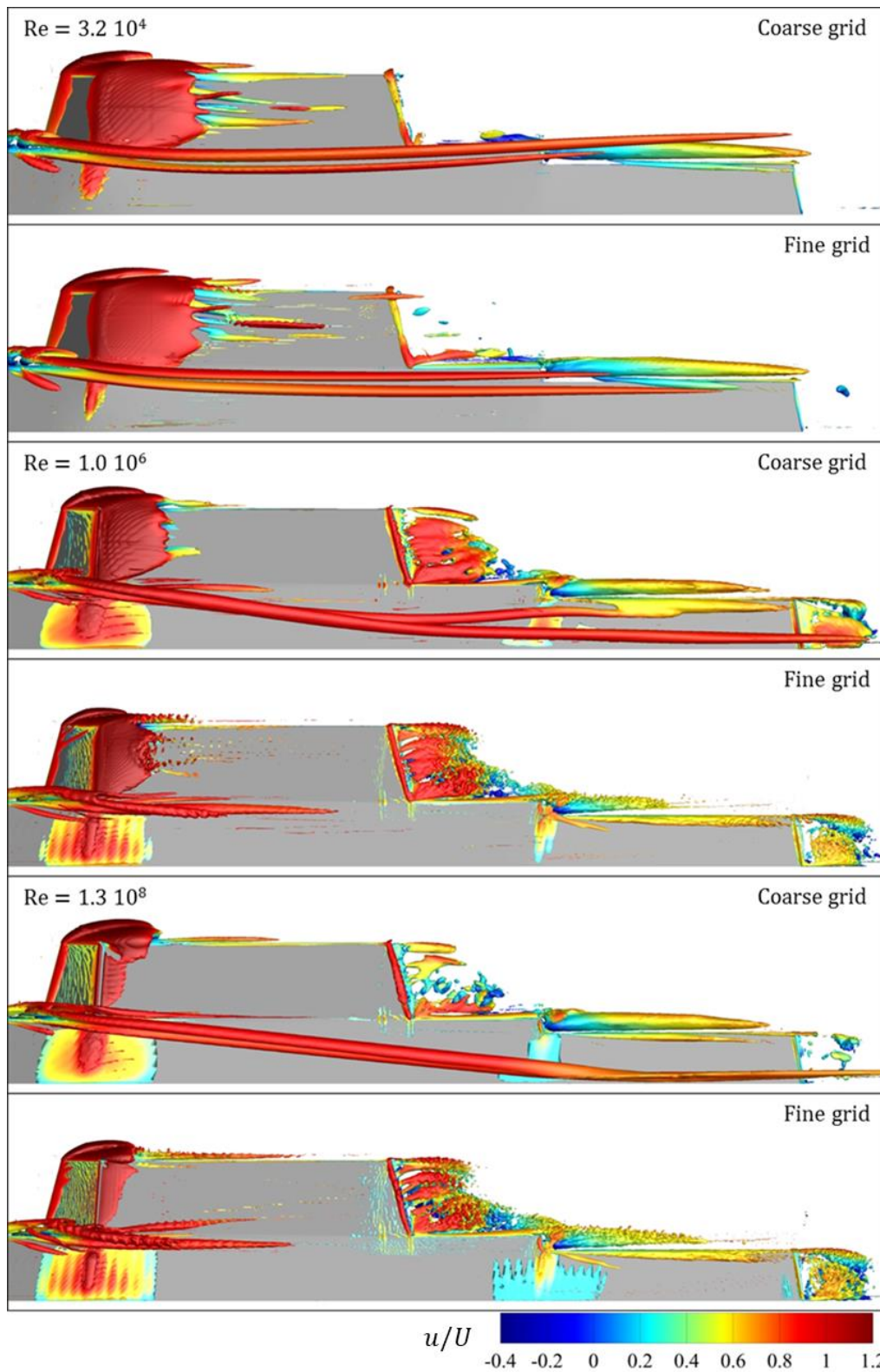
Figure 9: Iso-surfaces of Q-criterion colored by average streamwise velocity for three different Re numbers (3.2×10^4, 1×10^6, and 1.3×10^8) and two grid refinements (side view).

23
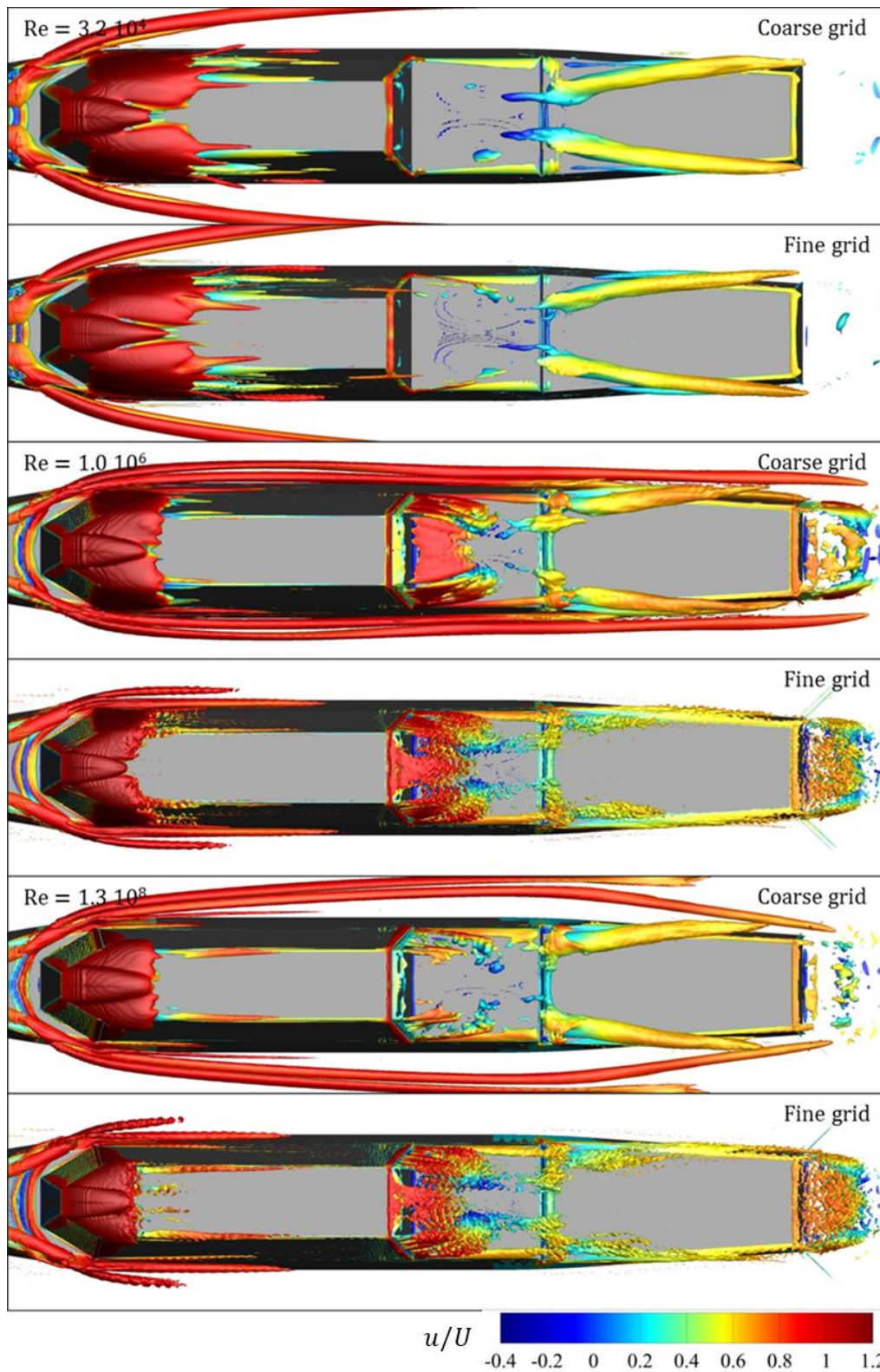
Figure 10: Iso-surfaces of Q-criterion colored by average streamwise velocity for three different Re numbers (3.2×10^4, 1×10^6, and 1.3×10^8) and two grid refinements (top view).

3.3.2 Comparison to experimental data

CFD results were compared to PIV experimental data at the model-scale Re=1x10^6 using

three different grid sizes. The centerplane (y=0) flow field in the region over the back deck of the

ship is shown in Figure 11, the gaps in the experimental results are due to the decreased field of

view resulting from the camera angles as well as a structural beam in the water channel where

the experiments were conducted (Dooley et al. 2019). Qualitative comparison of the CFD to the

experimental results shows that the velocity field in the streamwise direction matches well, with

slight differences seen in the transitions between the shear layer and the free stream flow. Larger

discrepancies are seen in the vertical velocity direction, especially in the recirculation region

behind the superstructure where CFD under predicts how far the downward flow is carried in the

flight deck region. Comparing the RMS of the velocity fluctuations in each direction also reveal

difference between CFD and experiments, as CFD tends to over predict the level of velocity

fluctuations in both directions for all grid sizes.
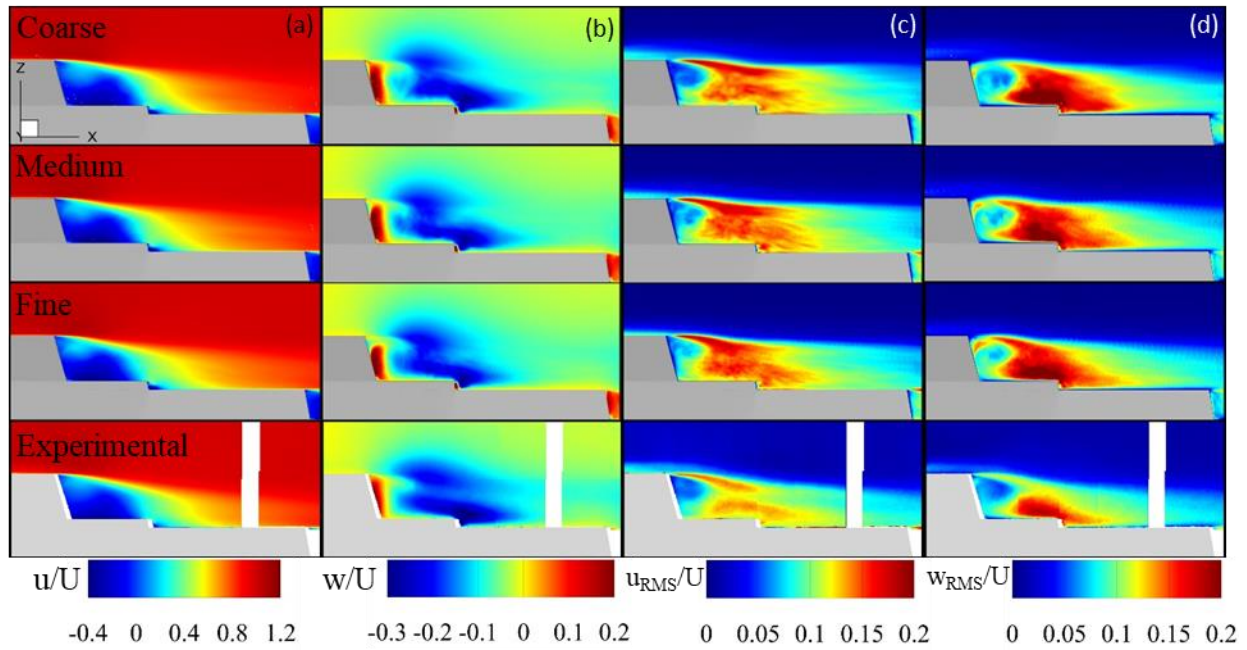
Figure 11: Mean streamwise (a) and vertical (b) velocity and RMS of velocity fluctuations for
streamwise (c) and vertical (d) directions at the centerplane, Re = 1x10^6, for different grid
refinements with experimental PIV results.

25

Velocity profiles were extracted in two different locations over the flight deck, these are the same locations described in §3.2.2. As mentioned previously, good agreement is seen in the streamwise velocity profile at both locations. Grid refinement does appear to increase the accuracy of CFD results at the location x/L=0.883 in the region of z/L=0.05-0.09. At this location the CFD results also show a more gradual transition to free stream flow at z/L=0.09-0.12. The under prediction of downward velocity by CFD in the flight deck region discussed previously can be seen clearly in the vertical velocity profile at x/L=0.883. Grid refinement at both locations for the vertical velocity profile does not appear to improve the accuracy of CFD. The over prediction of velocity fluctuations by CFD can be seen in the both directions at x/L=0.883, CFD differs from the experimental results by almost 50% in some vertical locations. The experimental results also contain far field RMS of approximatley 2.8% and 1.7% for streamwise and vertical velocity, respectively, while the CFD simulations were done with out any free stream turbulence. Spatial variability seen in the RMS of velocites profiles for CFD show that a longer time series would need to be resolved in order to achieve better convergence. Overall, the trend of the velocity fluctuations is resolved well by CFD, with similar increases seen in the shear layer region directly behing the top edge of the superstructure. The RMS of velocity also matches the experimental results much better in the flight deck region (x/L=0.883), which is the main area of concern for this specific study. It is believed that CFD is more accurate in this region as the flow is less chaotic and three dimensional which leads to more steady flow features, which are easier to resolve using CFD.
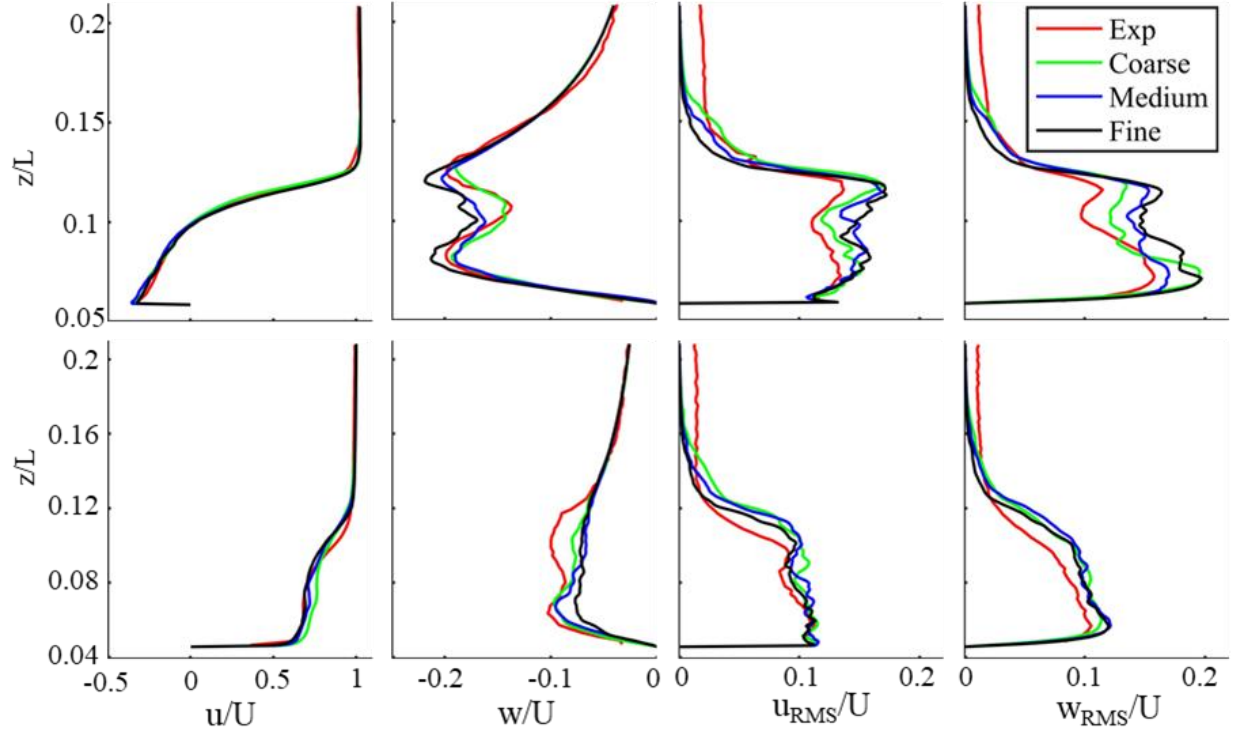
Figure 12: Top $x/L = 0.708$; Bottom $x/L = 0.883$, Re = 10^6, for three different levels of grid refinement.

As discussed previously the largest difference seen in the mean velocity field between CFD and experiments was in the vertical direction, this difference was analyzed further by computing the confidence interval (CI) at both locations in x/L in order to estimate the uncertainty. The CI was computed using the formula

$$\pm t_{v,95}\frac{S_u}{\sqrt{N}} \tag{8}$$

where:

$t_{v,95}$ is the t score at the 95% cumulative probability level

S_u is the standard deviation of the series

N is the number of samples ($v=N$-1)

The CI is plotted at various locations in z/L for all grid sizes and overall the grids show similar levels of uncertainty throughout. The highest levels of uncertainty correspond to regions of

27

increased velocity fluctuations. When taking uncertainty into consideration the CFD results do match the experiments better in some regions, specifically the region closer to the deck at x/L=0.708, with the coarse grid CI overlapping the experimental results at all locations where it is plotted. In regions where the CI of the CFD does not agree with the experimental measurements, overlap could be achieved with the consideration of experimental uncertainty.
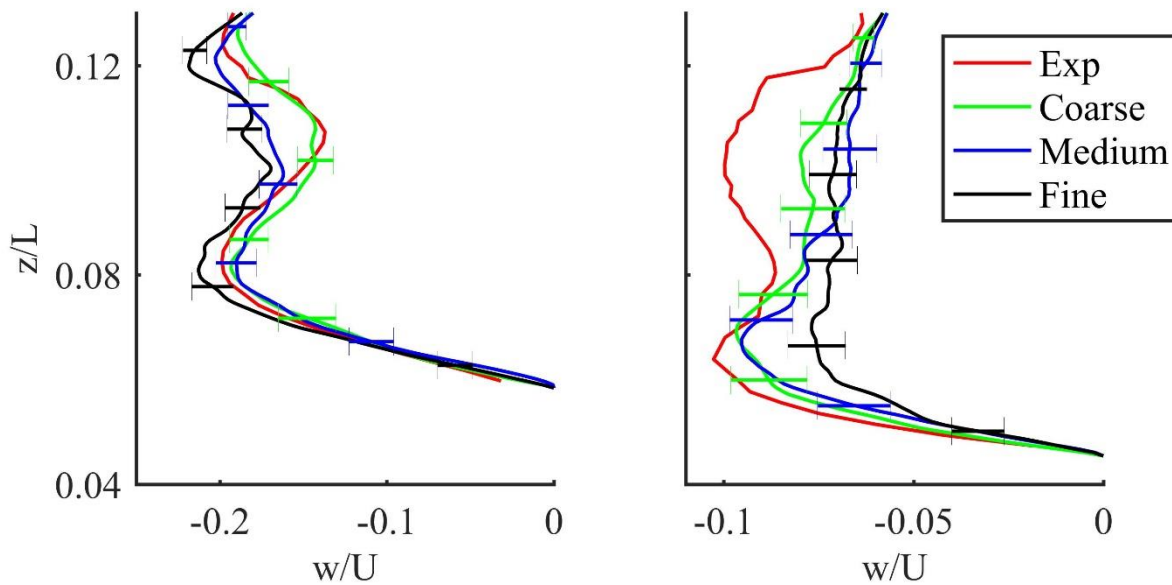
Figure 13: Line plot of vertical velocity profile at two different points (x/L=0.708 and 0.883) with the 95% confidence interval shown for each of the three grids.

In order to further investigate the difference seen in velocity fluctuations (RMS), probability density functions (PDF) of the velocity time history at six different positions were computed and compared to the experimental results, shown in Figure 14. The point at (x/L=0.708, z/L=0.125) is near the shear layer shed from the top of the superstructure which is associated with high levels of fluctuations so any discrepancy in the location of the shear layer would significantly impact the level of fluctuations at this location. It can be seen that by refining the grid, CFD fluctuations more closely match the experiments in both the streamwise and vertical directions. At (0.883, 0.1) Laser Doppler Velocimetry (LDV) data was also provided for comparison, the similarity of the PIV data to the LDV data gives some reference for the accuracy

28

of the PIV results. Overall, it can be seen that the CFD results over predict the velocity

fluctuations when compared to the experiments, specifically in regions of increased fluctuations

(i.e. near the shear layer). It is believed at this time that the over prediction is due to the

turbulence model being used, which would require additional simulations in order to confirm.
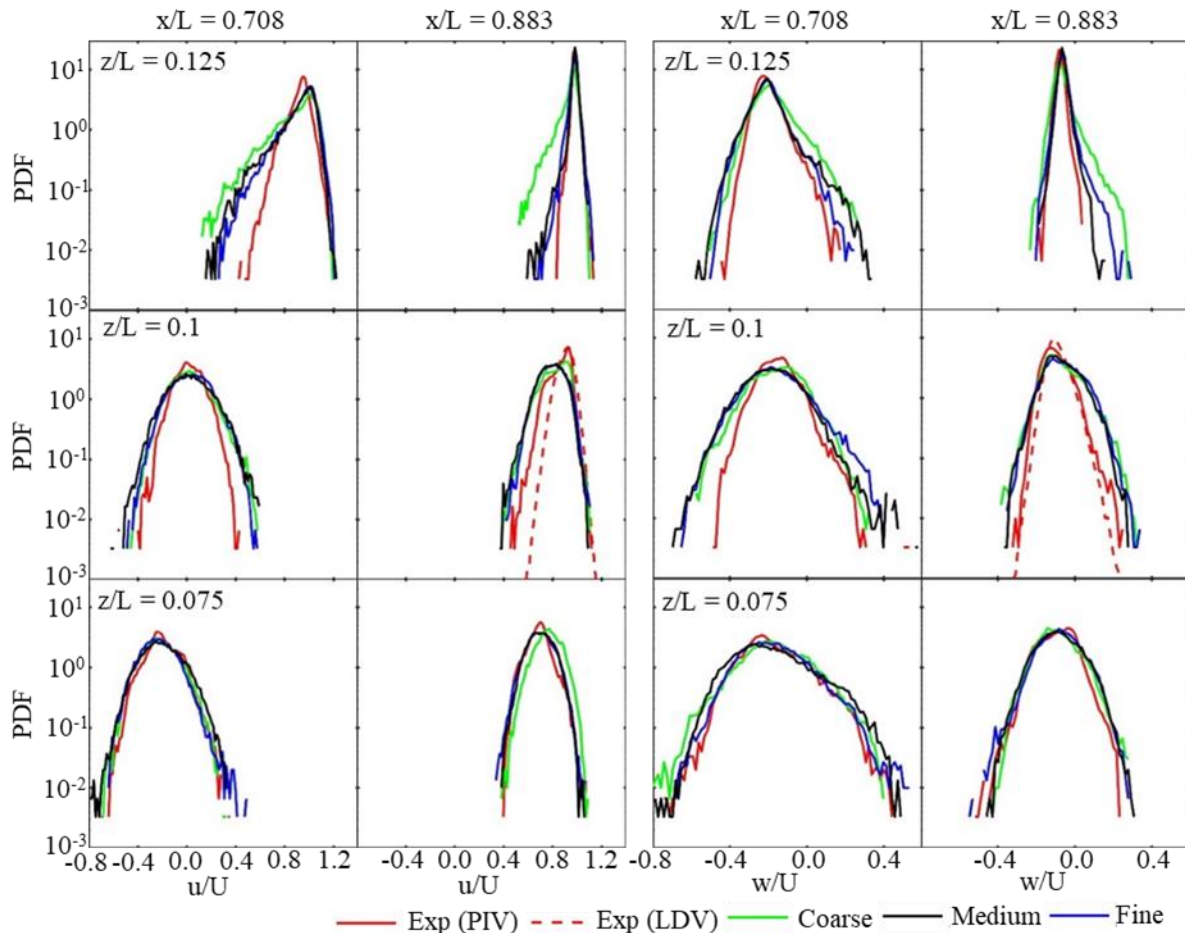
Figure 14: Probability distribution functions for horizontal (left columns) and vertical (right) velocity at six different locations in the symmetry plane (x/L = 0.708, 0.883).

Grid convergence was analyzed by comparing five different reattachment points for all

three grids at Re=1×10^6. The reattachment points consist of three points in the y/L=0 (symmetry)

plane, one on the top of the superstructure (SS) and two in the aft region, one behind each of the

back-facing steps (RZ1 and RZ2). The other two points are on the port side of the superstructure

in the *z*-plane at *z/L*=0.1 and 0.12. Figure 15 shows the regions of flow separation where the reattachment points described were predicted.
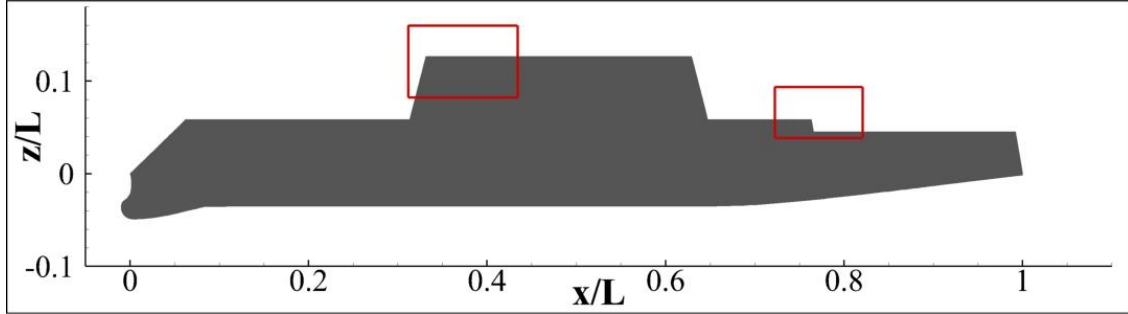
Figure 15: Flow separation regions where various reattachment points were calculated to analyze grid convergence at Re=1x10^6.

Table 3 contains the reattachment lengths at all locations described previously for each of the three grids. The table also contains the difference in reattachment locations between the medium and coarse grid and the fine and medium grid defined as

$$\varepsilon 12 = medium - coarse \tag{9}$$

$$\varepsilon 23 = fine - coarse \tag{10}$$

A calculated value such as reattachment point is determined to be monotonically converging with increased levels of refinement for 0<Rg<1, where

$$Rg = \frac{\varepsilon 23}{\varepsilon 12} \tag{11}$$

Using this methodology, the results show convergence for three of the five points analyzed, both points in the *z*-plane and the point behind the second back facing step in the *y*=0 plane. Looking at ε12 and ε23 for the two points that do not show convergence the increase in magnitude of ε23, which results in the classification of diverging, is relatively small in comparison to the grid spacing. Grid spacing in the streamwise direction in the region of the superstructure and the back deck is 5x10^{-4} and 10^{-3}, respectively, for the fine grid. The increase in ε23 for both points is equivalent to roughly 2-6 fine grid points and does not show any significant change that would

30

lead to the conclusion that the solution is highly grid dependent. These points also reside in areas of highly unsteady flow making the prediction of the reattachment point more time and space dependent. The detached region on the top of the superstructure experiences strong periodic shedding which occurs at a frequency of approximately 12 times per ship length, this periodic shedding may make the convergence of the reattachment point in this region highly time dependent. Also, both points that show divergence are in the symmetry plane (y=0) of the ONRT geometry which may be affected by any antisymmetric behavior in the mean flow solution between grids based on poor convergence in time.

Table 3: Reattachment lengths at five different locations for the coarse, medium, and fine grid at Re=1×10^6.

Grid	y/L=0			z-plane	
	SS	RZ1	RZ2	z/L=0.1	z/L=0.12
Coarse (1)	0.42972	0.74606	0.782206	0.43963	0.43254
Medium (2)	0.41781	0.74751	0.78408	0.42782	0.42324
Fine (3)	0.40266	0.74407	0.78436	0.42387	0.41682
ε12	-0.01192	0.00145	0.00187	-0.01181	-0.0093
ε23	-0.01515	-0.00344	0.00028	-0.00395	-0.00642
Rg	1.27204	-2.3753	0.14946	0.33446	0.69032

31

4.1 Simulation Design and Setup

4.1.1 Geometry and conditions
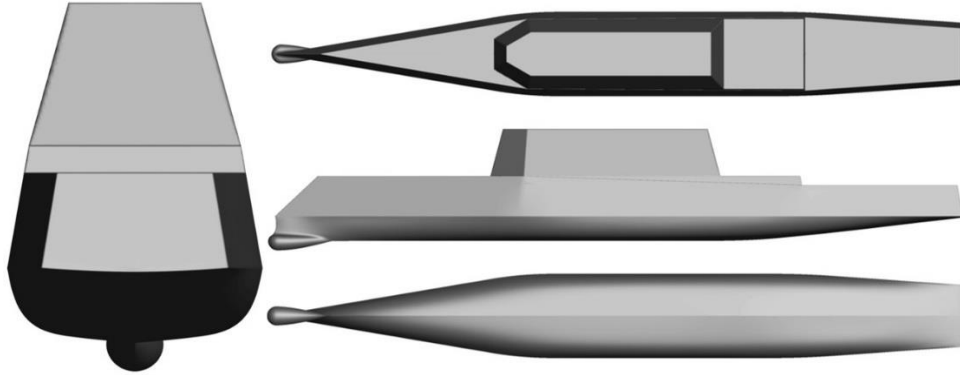
Figure 16: ONR Tumblehome geometry (DTMB model 5613).

The ONR Tumblehome geometry (DTMB model 5613) shown in Figure 16 was used for all simulations. This geometry is a research version of the U.S. Navy Zumwalt-class guided missile destroyer DDG-1000. The unconventional design of the Zumwalt-class is the result of trying to minimize its radar cross section and is part of a current trend of developing more stealth surface combatants. The barehull model used in this study does not include the bilge keels, rudders or any other appendages, helping reduce the computational costs of the simulations. For a list of relevant physical properties of the ONRT geometry refer to Table 4.

Table 4: ONRT full-scale dimensions.

Length (L, m)	154
Draft (m)	5.5
Beam (m)	18.78
Displacement ($Tons$)	8507
Longitudinal center of gravity (X_{cg}, m aft of FP)	79.52
Vertical center of gravity (Z_{cg}, m above WL)	2.153
Pitch moment of inertia (K_{yy}/L)	0.246

The study was conducted for wind speeds of 15 and 35 knots, representative of sea states (SS) 3 and 6 in the North Atlantic (Lewis 1989). Table 5 contains the particulars for the two

different sea states tested. For all cases the ship is advancing against the wind and waves (head seas) at 15 knots. Typically, sea states are defined based on irregular waves with a spectra of wavelengths and periods. The sea conditions were assumed to be fully developed, in which the waves are developed over large distances and periods of time. Computations were performed using regular head waves with an amplitude based on the significant wave height of the corresponding sea state as well as a period close to the most probable modal wave period.

Table 5: Regular wave properties for two simulated conditions.

Sea State (SS)	3	6
U_{Wind} (knots)	15	35
Wave Encounter Freq. (Hz)	0.134	0.113
Wave Amplitude (m)	0.625	2.5
Wave Length (m)	184.8	240.1

The complete simulation matrix is shown in Table 6. The case description refers to the bodies present during the simulation. The study of the airwake was performed under four scenarios for each wind speed: no ship motions or waves (baseline, NM/NW), no ship motions and with waves (NM/WW), with ship motions and no waves (WM/NW), with ship motions and waves (WM/WW). In all cases with motions and waves the ship is free to sink and trim, resulting in pitching and heaving motions when advancing through waves. Cases labeled 'baseline' have no imposed head waves but still maintain the same wind speed and resolve the characteristic Kelvin waves as the ship advances. The predicted ship motions obtained from the motions and waves case were imposed for the case with motions and no waves.

33

Table 6: Simulation matrix for studying effects of waves and motions on airwake flow.

Case	U_{Ship} (knots)	U_{Wind} (knots)	Relative Speed (knots), Re	Motions/Waves	Case Name
ONRT	15	15	30 1.6×10^8	No Motions/No Waves	Baseline: NM/NW/15$_S$
				Predicted/SS3	WM/WW/15$_S$
				No Motions/SS3	NM/WW/15$_S$
				Imposed/No Waves	WM/NW/15$_S$
		35	50 2.6×10^8	No Motions/No Waves	Baseline: NM/NW/35$_S$
				Predicted/SS6	WM/WW/35$_S$
				No Motions/SS6	NM/WW/35$_S$
				Imposed/No Waves	WM/NW/35$_S$

4.1.2 Simulation design

The overset grid topology used for the simulations is shown in Figure 17 and each of the grid dimensions/sizes are in Table 7. Due to computational costs a grid study was not performed, thus the grids were designed based on previous experience for similar problems where grid studies were conducted. The ONRT simulation grid system consists of six structured blocks: two body fitted grids for the starboard and port sides of the hull, one body fitted grid for the superstructure, one Cartesian free surface refinement, one Cartesian airwake refinement, and one Cartesian background grid used to impose boundary conditions. These grids are considerably finer than the finest grid system used in the grid studies by Carrica et al. (2007b) to compute pitch and heave in the surface combatant DTMB 5512, and by Sadat-Hosseini et al. (2011) for ONRT in following waves. The airwake refinement grid has approximately the same spacing as the medium grid used in Chapter 3 for the grid study of the static airwake flow over ONRT, which compared favorably with PIV experiments especially in the flight deck region. For the cases with motions the only grids that are free to pitch and heave are the ship body fitted grids (port hull, starboard hull, superstructure) all other grids are static aside from the imposed forward

34

motion. Due to the scale of the problem the grid wall spacing is such that $20<y^+<100$, to resolve

the boundary layer a three-zone wall function is used (Bhushan et al. 2009).
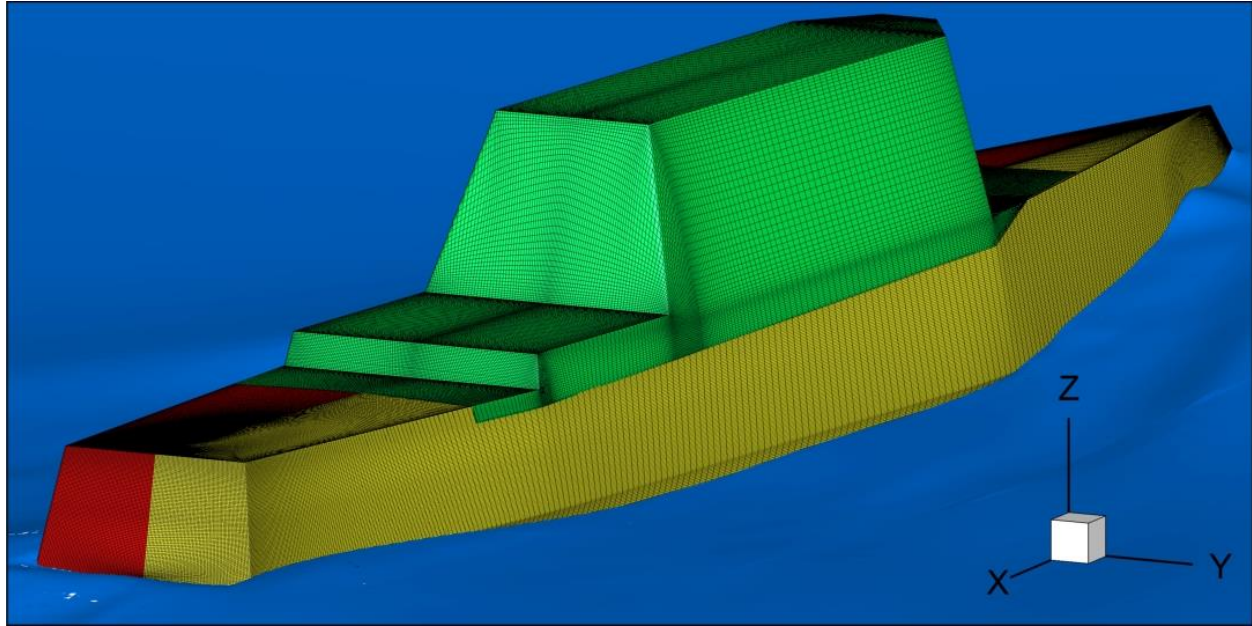
Figure 17: Overset grid topology for the ONRT geometry.

Table 7: Grid system used for the ONRT Simulations.

Grid	Dimensions	Reference Frame	Size
Port Hull	397 x 121 x 207	Ship	9.9M
Starboard Hull	397 x 121 x 207	Ship	9.9M
Superstructure	329 x 101 x 169	Ship	5.6M
Airwake Ref.	739 x 245 x 152	Earth	27.5M
Free Surface Ref.	384 x 92 x 140	Earth	4.9M
Background	256 x 179 x 239	Earth	10.9M

All quantities are non-dimensionalized using the reference values of the ship length

L=154 m and an arbitrary velocity of U=12.861 m/s (25 knots). The simulations are computed

using the Earth system frame of reference where the ship moves with respect to the ocean and

the wind and waves move in the direction opposite to that of the ship's forward motion (head

seas). Wind and wave boundary conditions are imposed at the inlet of the background grid,

located one ship length in front of the ship's bow.

The dimensionless time step was set based on the wave encounter frequency in order to resolve each encounter period by an integer number of solutions that could easily be used to decompose different phases. The average dimensionless time step was approximately 1.5×10^{-3}, which results in each wave encounter period being resolved by an integer number of time steps, 400 (SS3) or 480 (SS6). Volume solutions were recorded every five time steps, producing 80 or 96 volume solutions per encounter period. After the ship reaches a periodic response, an additional 32 to 37 encounter periods were simulated and used for analysis. This number of encounter periods resolved was limited due to the expensive nature of these simulations, the average total CPU time for each run was roughly 100,000 hours. Notice that proper statistics would require hundreds or thousands of encounter periods, which would result in extremely costly computations since wave encounter periods are roughly 8s in full-scale for normal conditions, thus requiring thousands of dimensional seconds of simulations. This translates to months of wall clock CPU time per simulation.

4.2 Ship Motions

The predicted ship motions for waves in SS3 and SS6 conditions are shown in Figure 18, all motions are measured at the ship's center of gravity. It can be seen that the pitching and heaving motions are dominated by the first harmonic of the encounter frequency. Under ideal conditions with a long wave the heave motion would lag the pitching motion by 90°, with pitch peaking at maximum wave slope and heave peaking at the crest. The wavelengths are $\lambda=1.2L$ and $\lambda=1.559L$ for SS3 and SS6, respectively, resulting in the ship piercing the waves to some extent instead of contouring them. This leads to a deviation from the long wave motion behavior. Figure 18 shows that this lag is closer to but still less than 90° for the SS6 case which has a longer wavelength than the SS3 case. The displacements at the center of the flight deck reach

36

peak-to-peak values of 1.5 m and 6 m for SS3 and SS6, respectively. For phase 0 degrees, when the wave crest is at the bow of the ship, the wave trough is located at $\lambda/2=0.6L$ and 0.78L for SS3 and SS6, respectively. At phase 180 degrees the trough and crest reverse positions. Figure 18 shows that the mid-flight deck, located at approximately $x/L=0.88$, will see the crest passing at phases of approximately 260 and 200 degrees for SS3 and SS6, respectively, almost coincident with the peak in flight deck displacement.
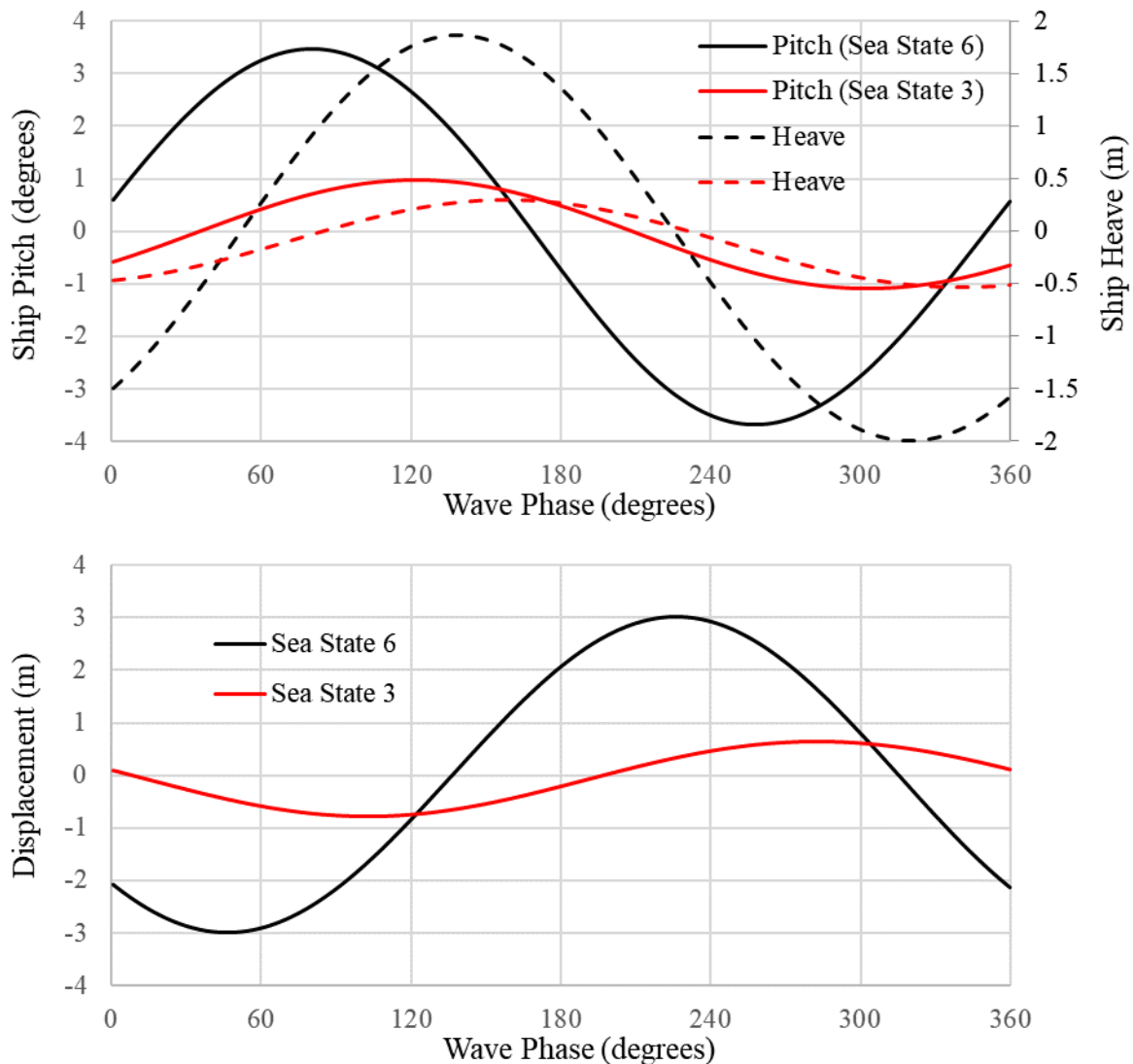
Figure 18: Ship pitch and heave through one wave encounter period (top) for SS3 (WM/WW/15$_S$) and SS6 (WM/WW/35$_S$) conditions, and ship displacement at mid-flight deck (bottom). The wave phase is defined as 0° when the wave peak is at the bow of the ship. Motions are measured at the ship's center of gravity.

4.3 Effects of Waves and Motions on Airwake flow

In order to quantitatively evaluate how motions and waves affect the airwake of the ship the velocity field is decomposed as

$$u = <u_T>(t) + u' = <u_{BL}> + <\Delta u_T>(t) + u' \tag{12}$$

where: $<u_{BL}>$ is the average velocity for the baseline condition with no motions or waves, $<\Delta u_t>(t)$ is the phase-averaged velocity deviation with respect to $<u_{BL}>$ and the wave encounter period T, $<\Delta u_T> = <u_T>(t) - <u_{BL}>$, and u' are the turbulent fluctuations. $<u_T>(t)$ is the phase-averaged velocity for the cases with motions, valid for $0 \leq t \leq T$ or $0 \leq \frac{360t}{T} \leq 360$ in degrees. For this analysis the phase is defined as zero when the wave crest is at the bow of the ship. The RMS values of interest for the decomposition in Equation (12) are u_{RMS}, the RMS of the total fluctuations, $<u_T>_{RMS}$, related fluctuations directly attributed to motions and/or waves and u'_{RMS}, resulting from turbulent fluctuations. Other interesting quantities are the RMS of the phase-locked fluctuations, corresponding to variations in velocity at a point when the ship is in the phase ($u_{T,RMS}(t)$), and the RMS of the baseline condition without motions or waves ($u_{BL,RMS}$). The change in RMS for any periodic conditions with motions and/or waves respect to the baseline condition is then

$$\Delta u_{RMS} = u_{RMS} - u_{BL,RMS} \tag{13}$$

The RMS fluctuations of the velocity in Equation (12) can be decomposed as

$$u_{RMS}^2 = <u_T>_{RMS}^2 + u'_{RMS}^2 + 2<(u_T - \bar{u})u'> \tag{14}$$

where $2<(u_T - \bar{u})u'> = \frac{1}{T_i}\int_0^{T_i}(<u_T> - \bar{u})u'dt$ is the cross correlation between the periodic fluctuations and the turbulent fluctuations and T_i is the integration time covering an integer number of encounter periods. If $<(u_T - \bar{u})u'>$ is neglected, the RMS of the velocity fluctuations for a case with motions and waves can be approximately reconstructed from the

38

results of a simulation without waves motions or waves (baseline computation) and the RMS of the periodic fluctuations with motions and waves as

$$u_{RMS,R} = \sqrt{<u_T>_{RMS}^2 + u'^2_{BL,RMS}} \tag{15}$$

with $u_{RMS,R}$ the reconstructed total RMS. Similar definitions apply for the other velocity components.

An example velocity decomposition for a point 30 ft above the mid-flight deck location is shown in Figure 19. The streamwise velocity signals for the baseline case with no motions or waves (NM/NW/35$_S$, u_{BL}) and for SS6 (WM/WW/35$_S$, u) are shown in the top panel, displaying both periodic and turbulent fluctuations. The center panel shows the mean of the baseline velocity ($<u_{BL}>$) and the phase-averaged velocity ($<u_T>$), which exhibits periodic fluctuations as the ship moves in waves. Note that the time averages of these two quantities are not equivalent. The turbulent component ($u' = u - <u_T>$), shown in the bottom panel, displays larger fluctuations when $<u_T>$ is lower, as the wake of the superstructure and its turbulent structures pass through the test point. This correlation between $<u_T>$ and u' results in some level of error in the approximation given by Equation (15) which needs to be evaluated to determine its importance.
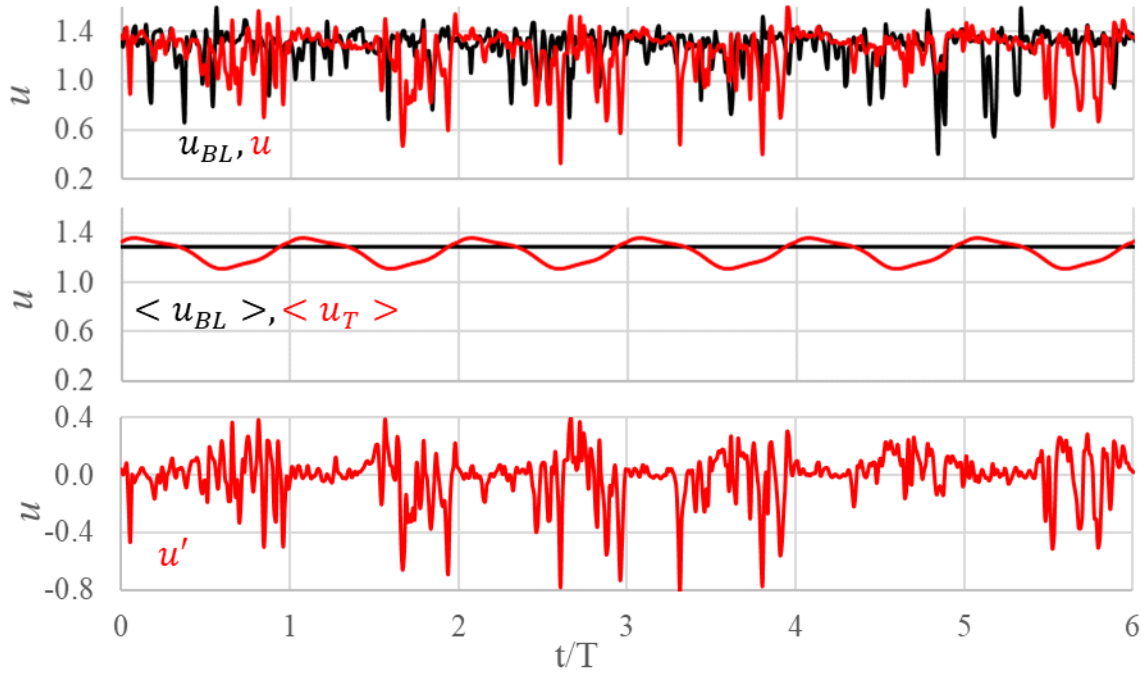
Figure 19: Velocity decompostion at a point 30 ft above the mid-flight deck location for ONRT advancing at 15 knots in 35 knots wind in waves with motions (NM/NW/35$_S$ and WM/WW/35$_S$).

4.3.1 Instantaneous flow fields
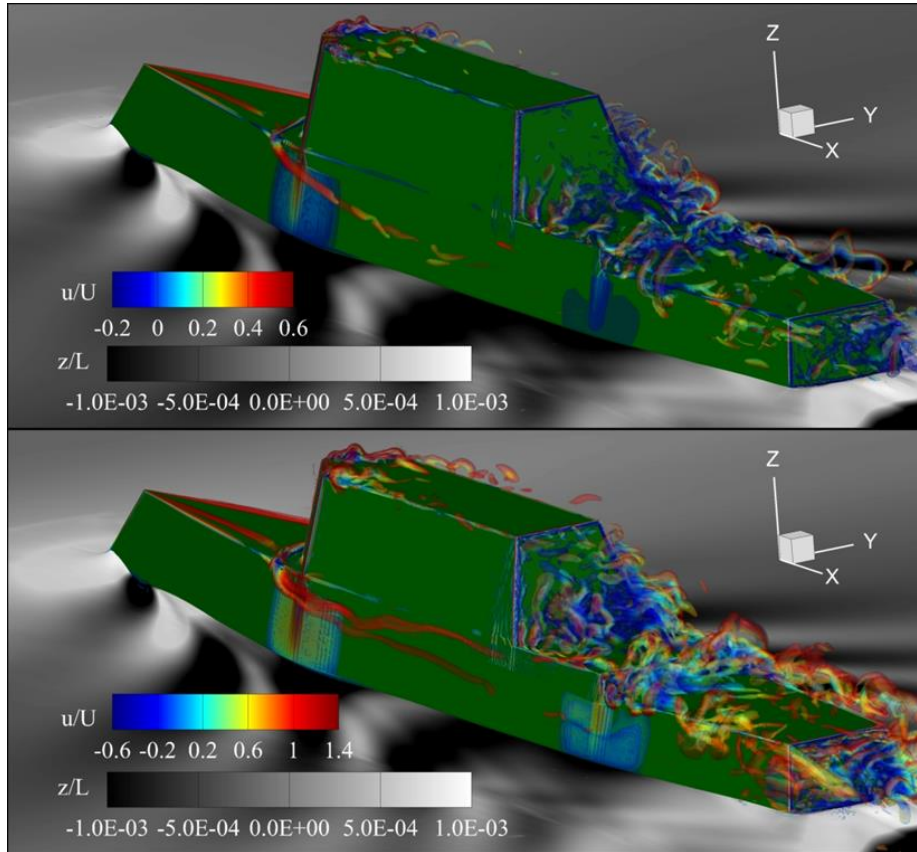
Figure 20: Instantaneous view of ONR Tumblehome advancing at 15 knots into 15 knots (NM/NW/15$_S$, top) and 35 knots (NM/NW/35$_S$, bottom) head wind. Vortical structures are shown as iso-surfaces of Q=5000, 20000, 50000 and 150000 with different levels of translucency.

Figure 20 shows instantaneous views of the ONRT advancing at 15 knots in calm water with uniform 15 (NM/NW/15$_S$, SS3) and 35 (NM/NW/35$_S$, SS6) knots head wind. Short Kelvin waves can be observed which are consistent with a low Froude number (Fr=0.1985). These two conditions are considered the baseline for each of the sea state conditions with no motions or waves. The vortical structures shown are similar to those discussed in §3.2 for ONRT in calm water at Reynolds numbers ranging from Re = 3.2x10^4 to 1.3x10^8, and also agree with the discussions in Buchholz et al. (2018) as the relative strength of the vortical structures are affected by the Reynolds number but overall patterns are maintained. The characteristic streamwise necklace vortices generated from the edges of the bow and the intersection between the bow and

41

the superstructure are clearly visible. These counter rotating streamwise vortices remain intact until reaching areas of more turbulent flow causing them to break down. The necklace vortices exhibit periodic behavior for the case with motions (WM/WW/35$_S$), as shown in Figure 21. Along the bow, the vertical velocity induced by the motions appears to counter the roll up due to the pressure differential between the bow and the hull. Moving past the junction between the bow and the superstructure the necklace vortices are affected by the ship motions and the moving free surface. At the 0 degree phase, when the wave peak is located at the bow, one of the vortices is pulled towards the free surface and at the 90 degrees phase (crest slightly upstream of mid ship) both vortices are pushed higher by the induced vertical velocity. The larger region of separation seen behind the superstructure is persistent throughout the wave encounter period, but its reattachment and strength are modulated by the ship motions, which can potentially affect the operation and control of aircraft operating in the ship airwake.
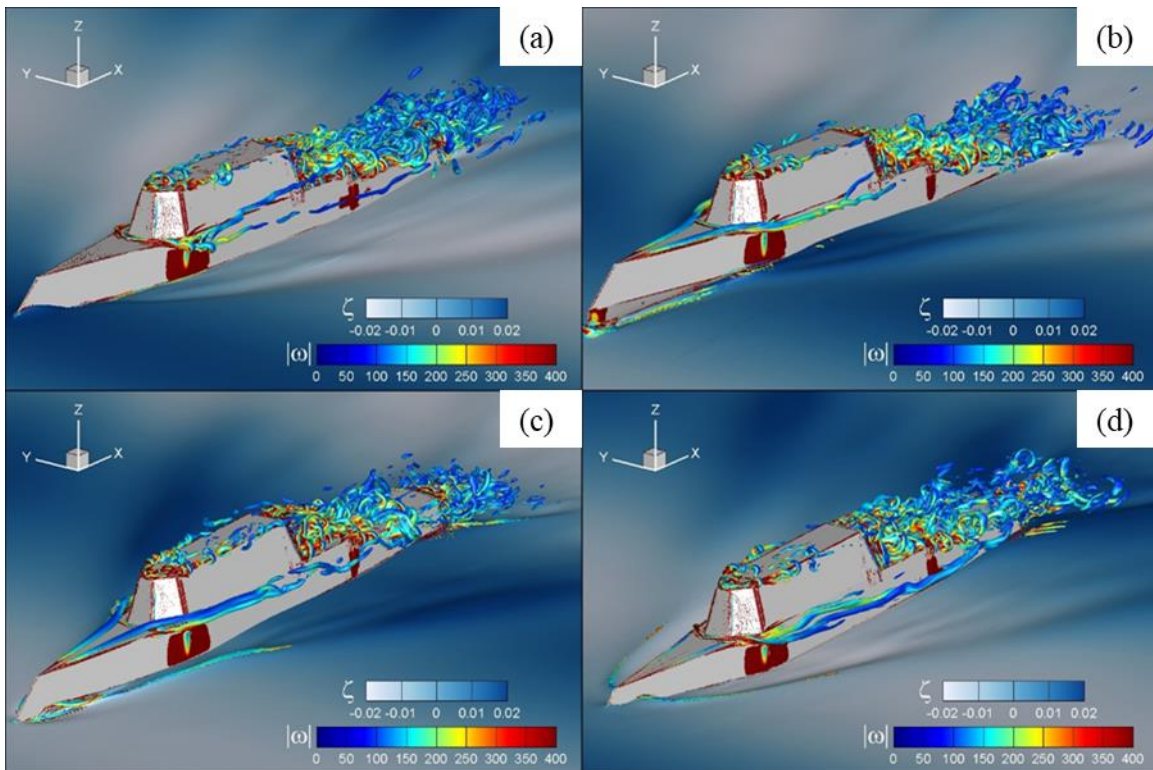
Figure 21: ONRT advancing at 15 knots in 35 knots wind in waves with motions (WM/WW/35$_S$). Phases are 0 degrees (a), 90 degrees (b), 180 degrees (c) and 270 degrees (d).

42

4.3.2 Averaged flow fields

The mean and RMS fluctuations of the velocities shown in Equation (12) on the center plane of the ONRT advancing at 15 knots in 15 and 35 knots head winds are presented in Figures 22 and 23, respectively. These figures include the four combinations of active or inactive waves and motions. All results are shown in the Earth reference system, and thus some regions near the solid body are fluid locations only part of the time; these regions are not considered, and an envelope for the ship is shown.

For the case with 15 knots head wind the waves and motions are mild and thus the effects on the mean and RMS fluctuations of the flow are limited, though noticeable. The shape of the recirculation zone can be seen in the average streamwise velocity (u), and with the addition of motions the transition between low speed to freestream flow is smoothed. Also, a slight increase in vertical velocity (w) can be seen near the end of the flight deck where the vertical motions of the ship are highest. By compring the no motions with waves case (NM/WW/15$_S$) to the with motons and no waves case (WM/NW/15$_S$) it can be seen that the area of strongest negative vertical velocity behind the superstrcuture decreases in size for the case with motions. It is assumed this is caused by the upward velocity induced by the pumping of the ship deck and periodic interactions between the boundary layer of the ships geometry and the flow in this region. The RMS of velocity fluctuations are very consistent throughout all cases especially in the streawise direction, with only slight differences visible in the recirculation region and near the stern. For example, in the vertical direction RMS magnitudes in the recirculation region can be seen decreasing slightly and increased levels appear in the region closer to the stern for the cases with motions.

43
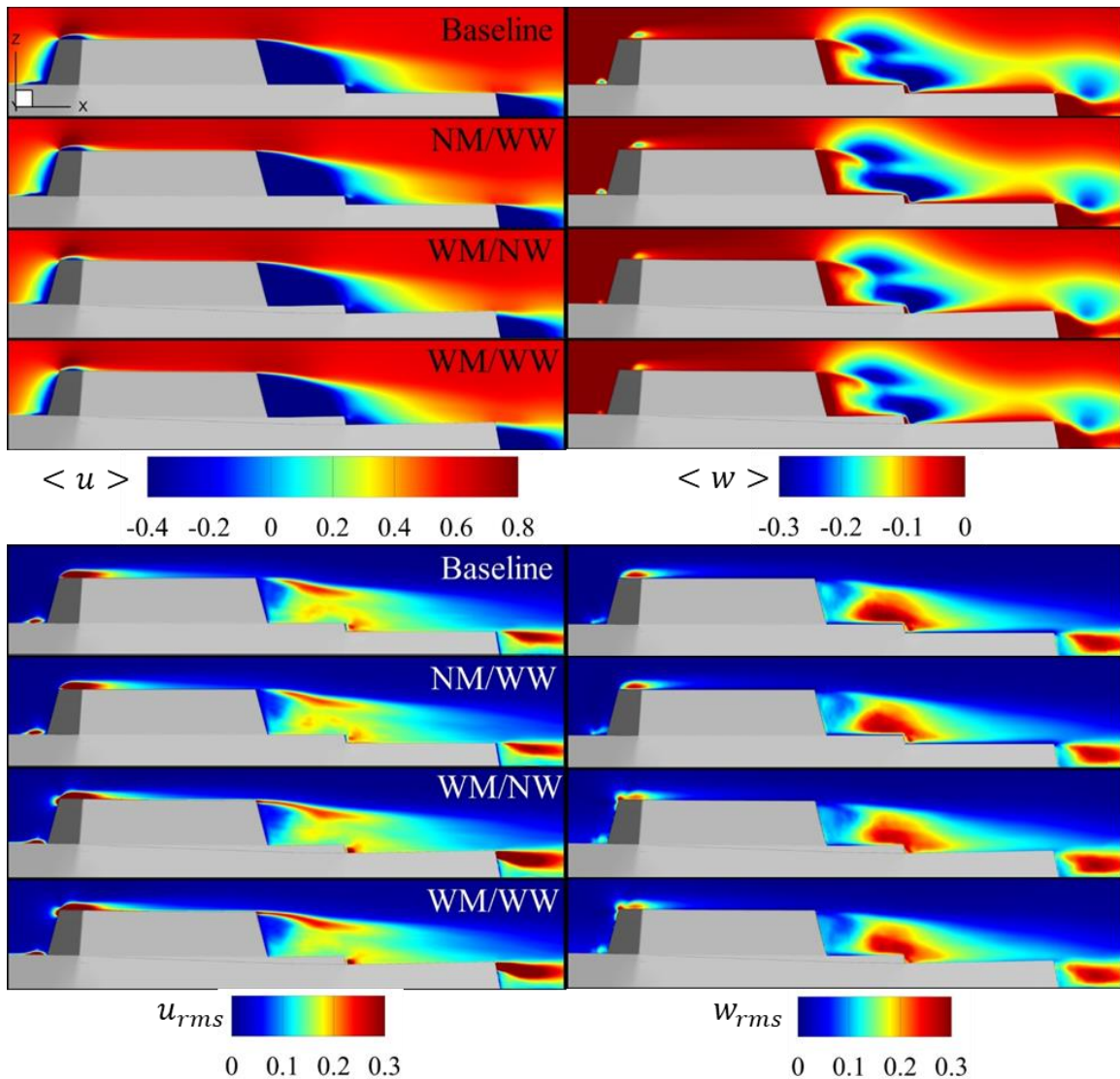
Figure 22: Mean (top) and total fluctuation RMS (bottom) for streamwise (left) and vertical (right) velocities for ONRT advancing at 15 knots in 15 knots wind with and without waves and/or motions (NM/NW/15s, NM/WW/15s, WM/NW/15s, and WM/WW/15s).

Effects of motions are considerably stronger for 35 knots wind, the most noticeable being the massive increase in streamwise RMS fluctuations directly behind the top of the superstructure. As the shear layer moves with the ship motions the region downstream the top of the superstructure is exposed to free stream flow and low speed recriculation flow periodically, dramtically increasing the level of velocity fluctuations in this region. This also results in what appears to be a thickening of the shear layer for the cases with motions due to periodic changes

44

in the location of the superstructure and thus the shear layer. The same effect can be seen more dramtically in the shear layer shed from the stern of the ship as well. Interestingly, the area of high streamwise RMS behind the superstructure appears to reach farther in to the flight deck region for the case with only motions (WM/NW/35$_S$) than for the case with motions and waves (WM/NW/35$_S$), suggesting that the waves damp the streamwise fluctuations. By comparing the baseline (NM/NW/35$_S$) to the case with only waves (NM/WW/35$_S$) the region of high streamwise RMS in the shear layer can be seen increasing in size with the addition of waves. This means that the RMS fluctuations from waves and motions must work in counter phase of eachother as the overall streamwise RMS decreases when they are added together. Many of the same consequences of motions mentioned for the SS3 case can be seen in the SS6 condition with increased magnitude. For example, the transition between the shear layer and the free stream flow is smoothed significantly for the cases with motions. Also, the addtion of motions (WM/NW/35$_S$ and WM/WW/35$_S$) increases the average vertical velocity, particularly in the region near the stern, leading to an increase in vertical velocity of about $0.1U$. Also similar to the SS6 condition, the motions decrease the size of the region with the most negative vertical velocity behind the superstrcuture and close to the back facing step. Lastly, regions of higher RMS fluctuations in the vertical direction extend further down the flight deck and also higher in the vertical direction for the cases with motions.
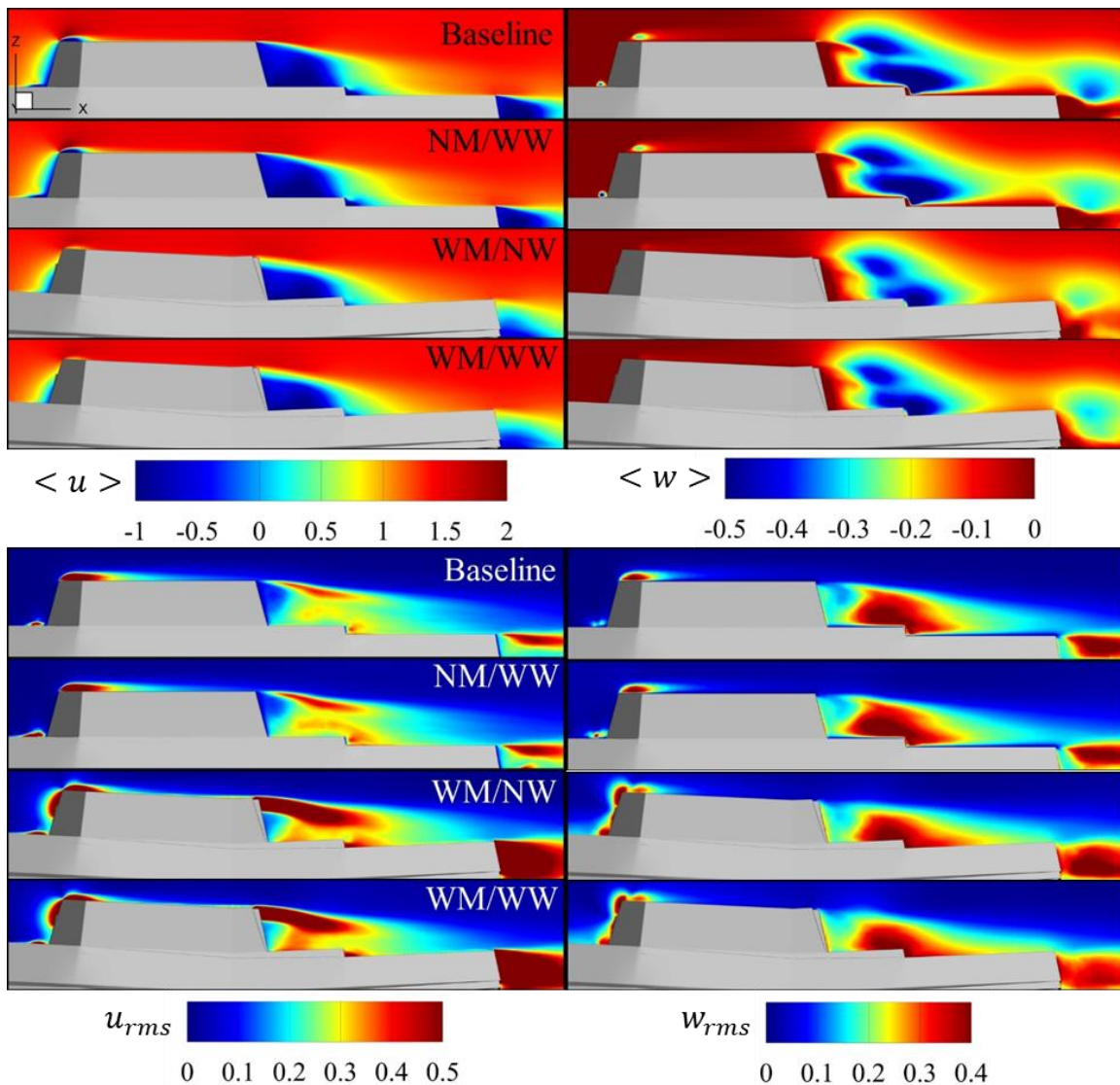
Figure 23: Mean (top) and total fluctuation RMS (bottom) for streamwise (left) and vertical (right) velocities for ONRT advancing at 15 knots in 35 knots wind with and without waves and/or motions (NM/NW/35s, NM/WW/35s, WM/NW/35s, and WM/WW/35s).

Figures 24 and 25 show the phase-averaged streamwise and vertical velocities on the centerplane for SS6 and SS3, respectively. Figure 24 shows that the location of the shear layer between the recirculation zone and the free stream moves along the length of the flight deck as the ship pitches. This region moves lower in the earth coordinate system when the bow is up at phase 90 degrees and higher during the pitch down motion at phase 270 degrees. It is believed this due to do the tangential velocity induced by the flight deck boundary layer as well as the

angle of the top of the superstructure. For positive pitch the flight deck slope is negative so flow moving tangentially to the flight deck has a negative vertical component in the earth coordinate system, and the opposite occurs for negative pitch. This phenomenon is expected and was reported in the experimental results of Sydney et al. (2017) for SFS2 and will cause periodic changes in streamwise velocity for an aircraft operating above the deck. The largest effect seen in the phase averages of the vertical velocity is in the region closest to the flight deck. When the flight deck is rising between 55 and 235 degrees of phase (see Figure 18), the vertical deck velocity imposes a solid boundary condition with an upward velocity, and conversely a downward velocity when the flight deck is receding. The motions are much smaller for SS3 as shown in Figure 25, so the effects are less significant. At phases 90 and 270 degrees the shear layer between the recirculation zone and the free stream velocity does not appear to move lower or higher as it did for SS6, as the motions appear to be too small to induce this behavior. Some change in the shear layer can be observed in phases 0 and 270 degrees as it appears to extend further down the flight deck. In the vertical velocity direction, there is some effect near the flight deck from the ship moving up and down, again this effect is much smaller than that seen in SS6. It is speculated that the phases between the two seas do not show the exact same trends due to the fact that both the wave amplitude and length are different, affecting amplitude, frequency and phase of the motions.

47

Figure 24: Phase-averaged streamwise (left) and vertical (right) velocities for the four quarter phases for ONRT advancing at 15 knots in 35 knots wind in waves with motions (WM/WW/35s). The baseline condition is shown at the bottom (NM/NW/35s).

Figure 25: Phase-averaged streamwise (left) and vertical (right) velocities for the four quarter phases for ONRT advancing at 15 knots in 15 knots wind in waves with motions (WM/WW/15s). The baseline condition is shown at the bottom (NM/NW/15s).

48

The phase-averaged deviation from the baseline $< \Delta u_T >$ and $< \Delta w_T >$ are shown in Figures 26 and 27 for SS6 and SS3, respectively. The deviations can be used to measure the effect waves and motions have on the mean flow, and represent a first order correction for dynamic interface simulators if motion effects are added linearly. For SS6 the largest effect seen in the streamwise velocity is in the variable shear layer on top of the superstructure. The region that reaches the flight deck experiences fluctuations in the order of $\pm 0.15U$ or ± 3.75 knots. In the same region of the flight deck, fluctuations of $\pm 0.2U$ are seen in the vertical direction, but only very close to the flight deck and quickly dissipate in the areas above it. The region directly behind the superstructure experiences the largest deviation from the baseline, greater than $\pm 0.25U$, but are of lesser importance in the interest of flight operations. For SS3 the deviations are much smaller throughout and do not appear to extend as far into the flight deck regions as those shown for SS6. Figure 27 shows that for SS3 the largest deviation is experienced at the 270 degree phase, coincident with the largest mid-flight deck motion (Figure 18). The deviations at this phase reach levels seen in the SS6 case but occur in the region near the superstructure and very close to the flight deck. At the 180 degrees phase where the deck displacement rate is close to its maximum an increase of roughly $0.06U$ in the vertical direction is predicted, this is significantly less than the $0.2U$ seen for SS6. The deviations that extend into the flight deck region are typically less than $\pm 0.1U$ or ± 2.5 knots for the SS3 conditions. It is also believed that some of the mild velocity deviations seen for SS3 can be associated with turbulent fluctuations due to the limited number of periods computed and used for phase-averages. Effects from motions and waves are isolated using a different approach in §4.3.2 as well.
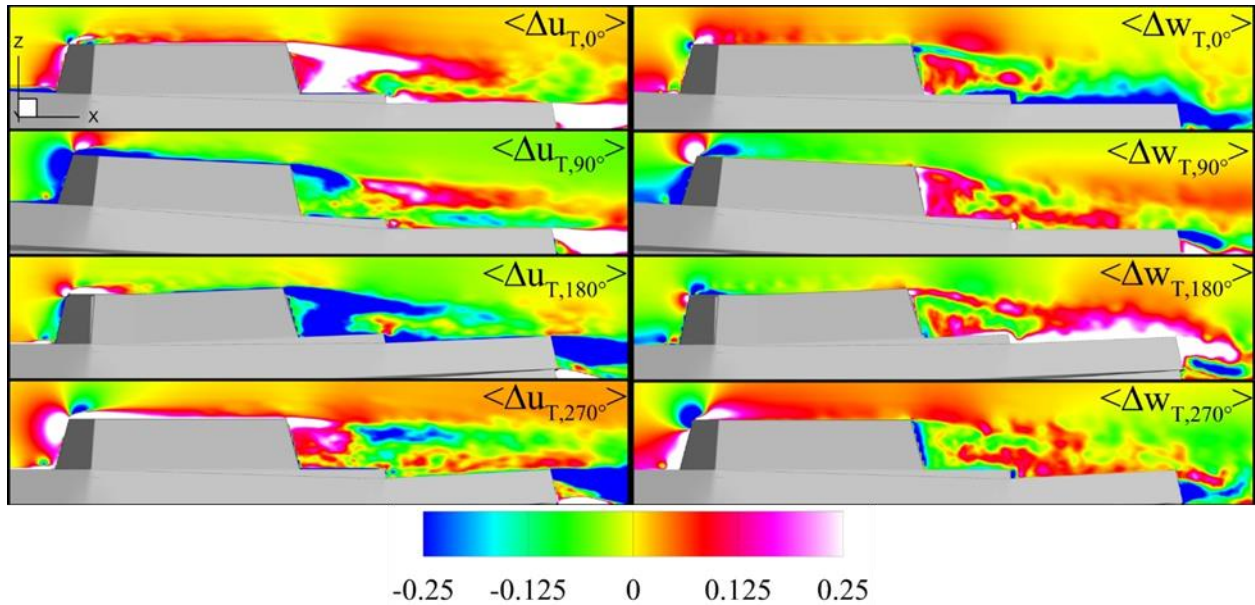
Figure 26: Phase-averaged mean streamwise and vertical velocity deviations from baseline for ONRT advancing at 15 knots in 35 knots wind, with waves and motions (WM/WW/35s, SS6).
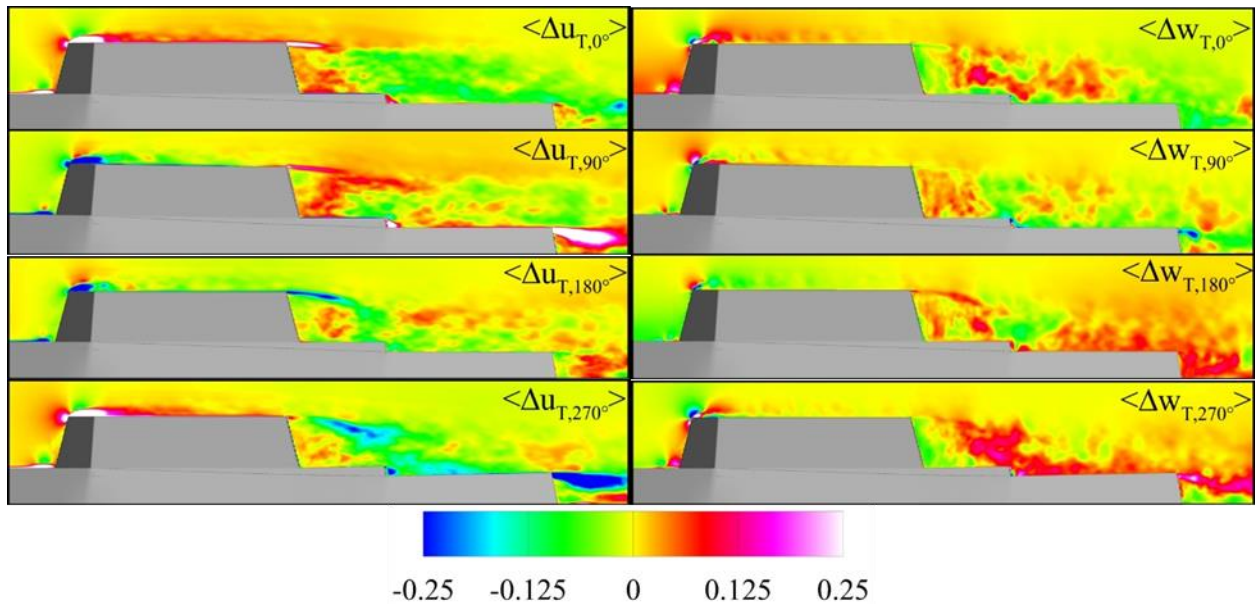
Figure 27: Phase-averaged mean streamwise and vertical velocity deviations from baseline for ONRT advancing at 15 knots in 15 knots wind, with waves and motions (WM/WW/15s, SS3).

Phase-locked RMS of the streamwise and vertical velocity fluctuations are shown in

Figures 28 and 29 for SS6 and SS3, respectively. For SS6 it can be seen that the region of higher

RMS fluctuations follows the same behavior as the phase-averaged velocity. As the ship pitches

up the region of higher RMS over the flight deck moves down in the Earth coordinate system

and is also accompanied by lower levels of RMS fluctuations overall. The turbulent region can be seen increasing in size as the ship pitches down and is largest at the 270 degree phase. For SS3 (Figure 29) the mid-flight deck is at its lowest position at the 90 degrees phase, which corresponds to decreased levels of RMS fluctuations in the streamwise direction, most noticeably directly behind the top of the superstructure. Slight increases in streamwise RMS fluctuations can be seen for phases 180 and 270 degrees (pitching down) but are much less significant than those seen for the same phases in SS6 condition. RMS fluctuations are largest at the 0 degree phase, when the mid deck displacement is approximately equal to zero. Due to differences in wave length the 90 degrees phase for SS6 and the 180 degrees phase for the SS3 are at approximately the same location in the wave cycle (mid deck moving up) and exhibit very similar behavior with the RMS fluctuations in the streamwise and vertical direction moving closer to the flight deck.
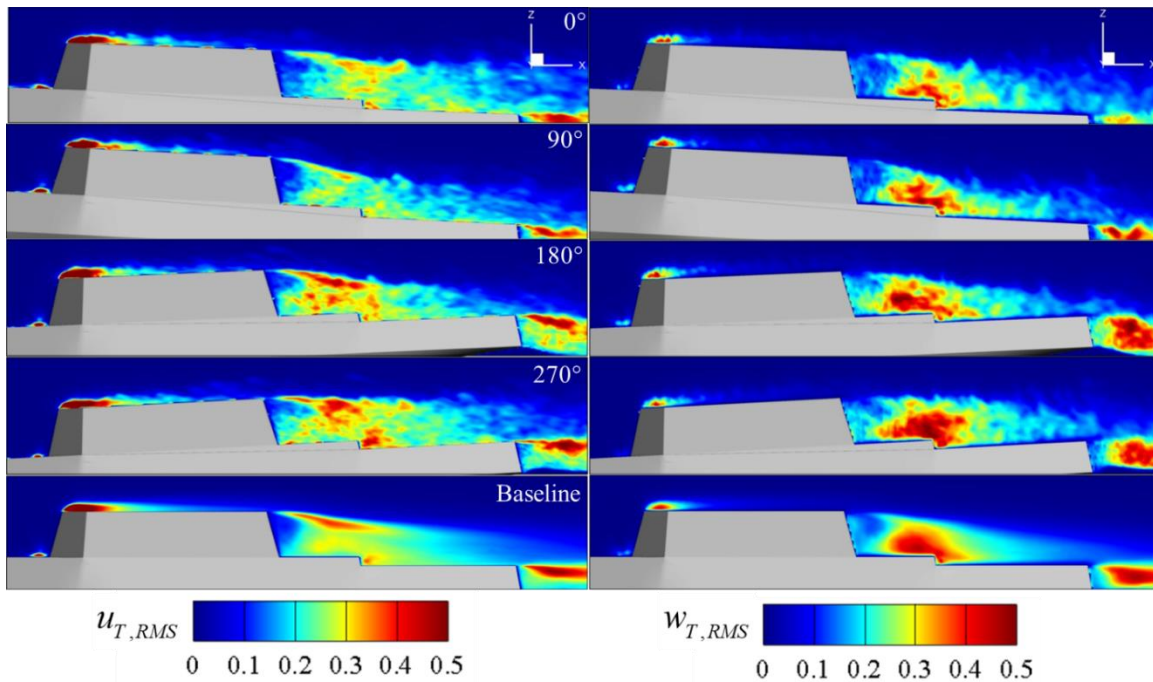
Figure 28: RMS of the phase-locked streamwise (left) and vertical (right) velocity fluctuations for the four quarter phases for ONRT advancing at 15 knots in 35 knots wind in waves with motions (WM/WW/35s). The total RMS for the baseline condition is shown at the bottom (NM/NW/35s).
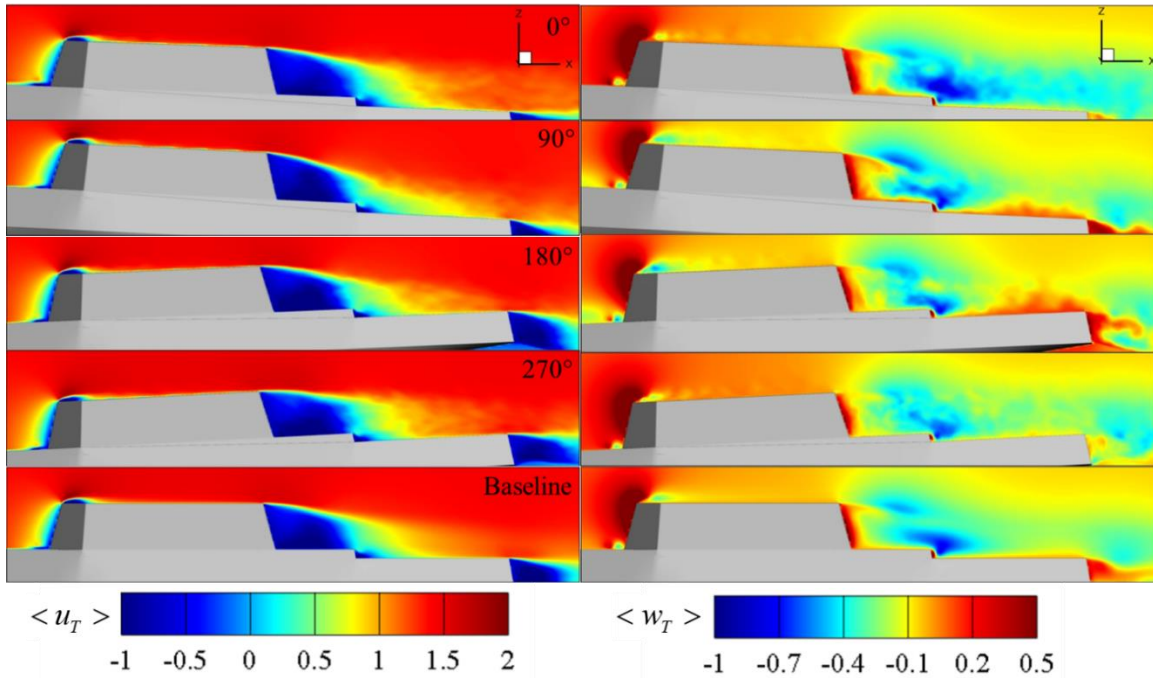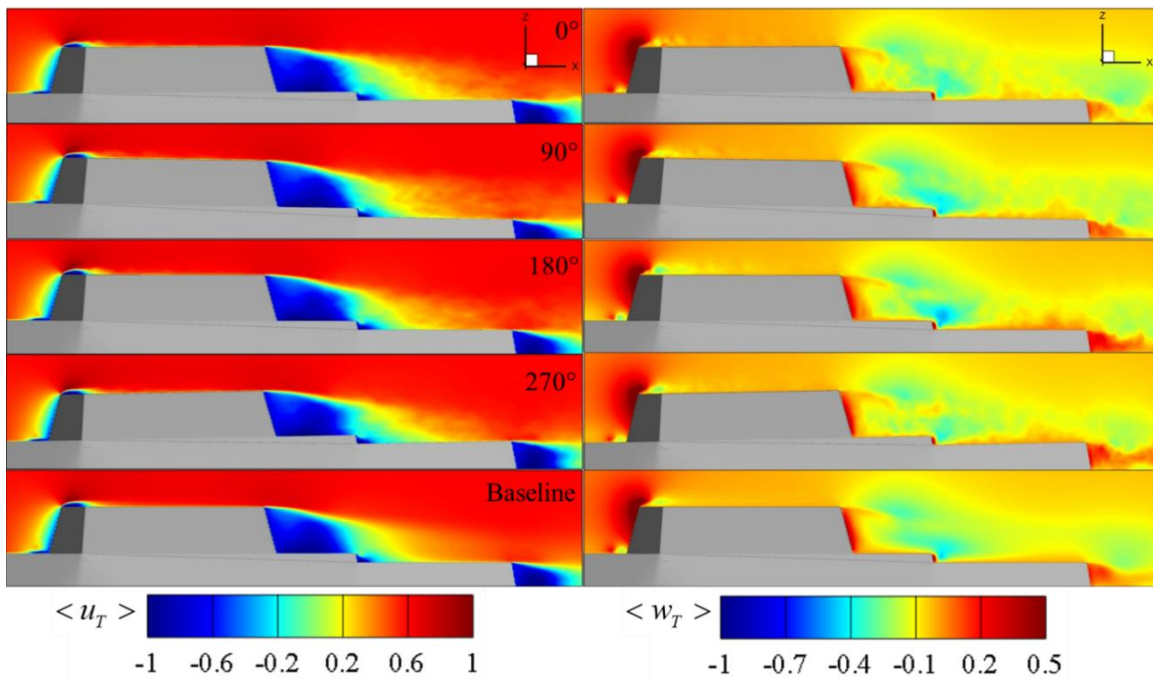
51
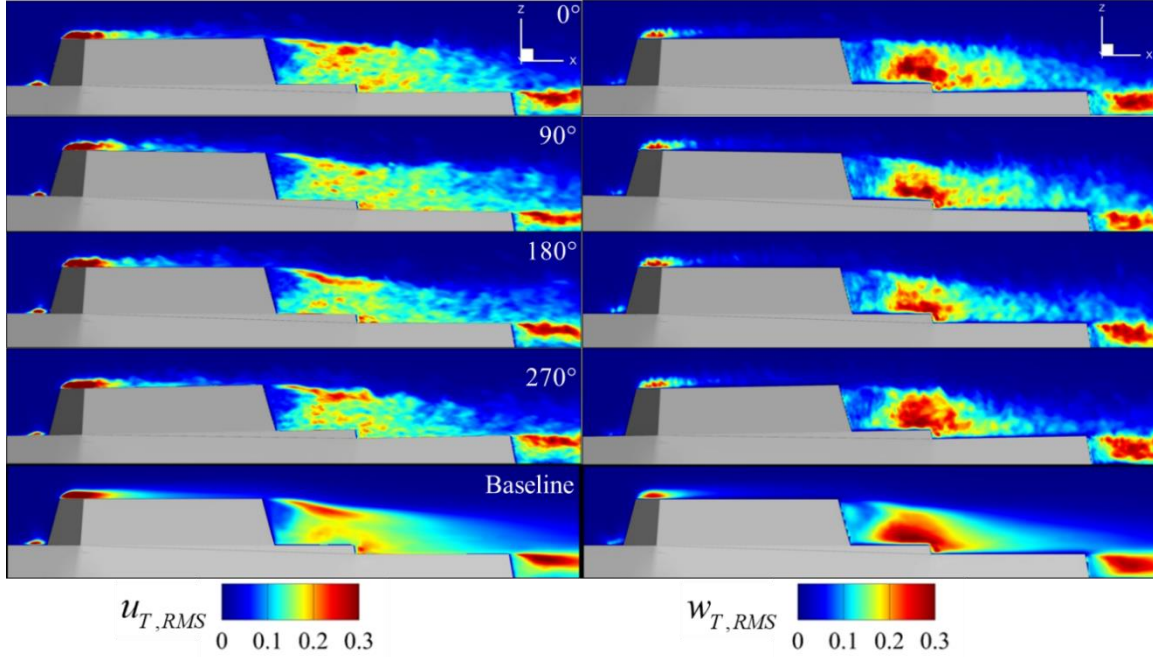
Figure 29: RMS of the phase-locked streamwise (left) and vertical (right) velocity fluctuations for the four quarter phases for ONRT advancing at 15 knots in 15 knots wind in waves with motions (WM/WW/15s). The total RMS for the baseline condition is shown at the bottom (NM/NW/15s).

The RMS fluctuations of the decomposed velocity in Equation (12) can better show the effects of motions and turbulent fluctuations on total RMS. Figures 30 and 31 show the magnitudes of the total RMS fluctuations of streamwise and vertical velocities for the baseline (NM/NW) and the case with motions and waves (WM/WW) in SS6 and SS3, respectively. For the cases with waves and motions the phase-averaged velocities $< \Delta u_T >_{RMS}$ and $< \Delta w_T >_{RMS}$, and turbulent fluctuations u'_{RMS} and w'_{RMS} are also shown.

The higher sea state case is analyzed first as the changes are more distinguishable due to the larger motions. For the case with motions a slight increase in the total streamwise velocity fluctuations throughout most of the domain can be seen, and is considerably higher in the shear layer directly downstream of the superstructure and the stern. Vertical velocity fluctuations also increase due to motions in the area above the flight deck but decrease in the recirculation region directly behind the superstructure. The RMS of the phase-averaged streamwise velocity

52

$(< u_T >_{RMS})$ shows very high values downstream of the top of the superstructure, in excess of $0.4U$ in the recirculation zone and still close to $0.1 \sim 0.2U$ over the flight deck. RMS of the phase-averaged vertical velocity $(< w_T >_{RMS})$ is also high over the flight deck, but the amplitude decays quickly with height. This is consistent with the observations from Figure 26. Fluctuations in $< u_T >$ and $< w_T >$ occur with the encounter frequency, corresponding to 0.113 Hz in SS6. This frequency is low enough that a pilot aware of these fluctuations should be able to respond with the proper commands to control the aircraft, as it falls within the range of frequencies known to affect pilot workload (0.1-2 Hz) (Thedin et al. 2018). The turbulent component of the total RMS fluctuations u'_{RMS} and w'_{RMS} can be compared to the RMS fluctuations of the baseline case without motions or waves. The RMS of the turbulent fluctuations is generally lower with motions than for the static ship case, indicating the motions and waves tend to inhibit turbulent fluctuations, in particular around the shear layer where points are exposed more frequently to the free stream that carries no turbulence in the simulation. $u_{RMS,R}$ and $w_{RMS,R}$, the linear superposition of the total RMS fluctuations from the baseline case (NM/NW/35$_S$) and the RMS fluctuations from the waves/motions (WM/WW/35$_S$) $< u_T >_{RMS}$ and $< w_T >_{RMS}$ as defined in Equation (15), are also shown in Figure 30, along with the cross-correlation term $< (u_T - \bar{u})u' >$. Notice that $u_{RMS,R}$ and $w_{RMS,R}$ produce good approximations to u_{RMS} and w_{RMS}, respectively, and that the cross correlation contributions for streamwise and vertical velocities, expressed as $sign\ [< (u_T - \bar{\bar{u}})u']\sqrt{2abs[< (u_T - \bar{\bar{u}})u' >]}$ for the streamwise component, is relatively small except in the shear layer above the flight deck and immediately downstream of the superstructure and stern, where it can reach 10% of the total RMS for streamwise and vertical velocities.

53
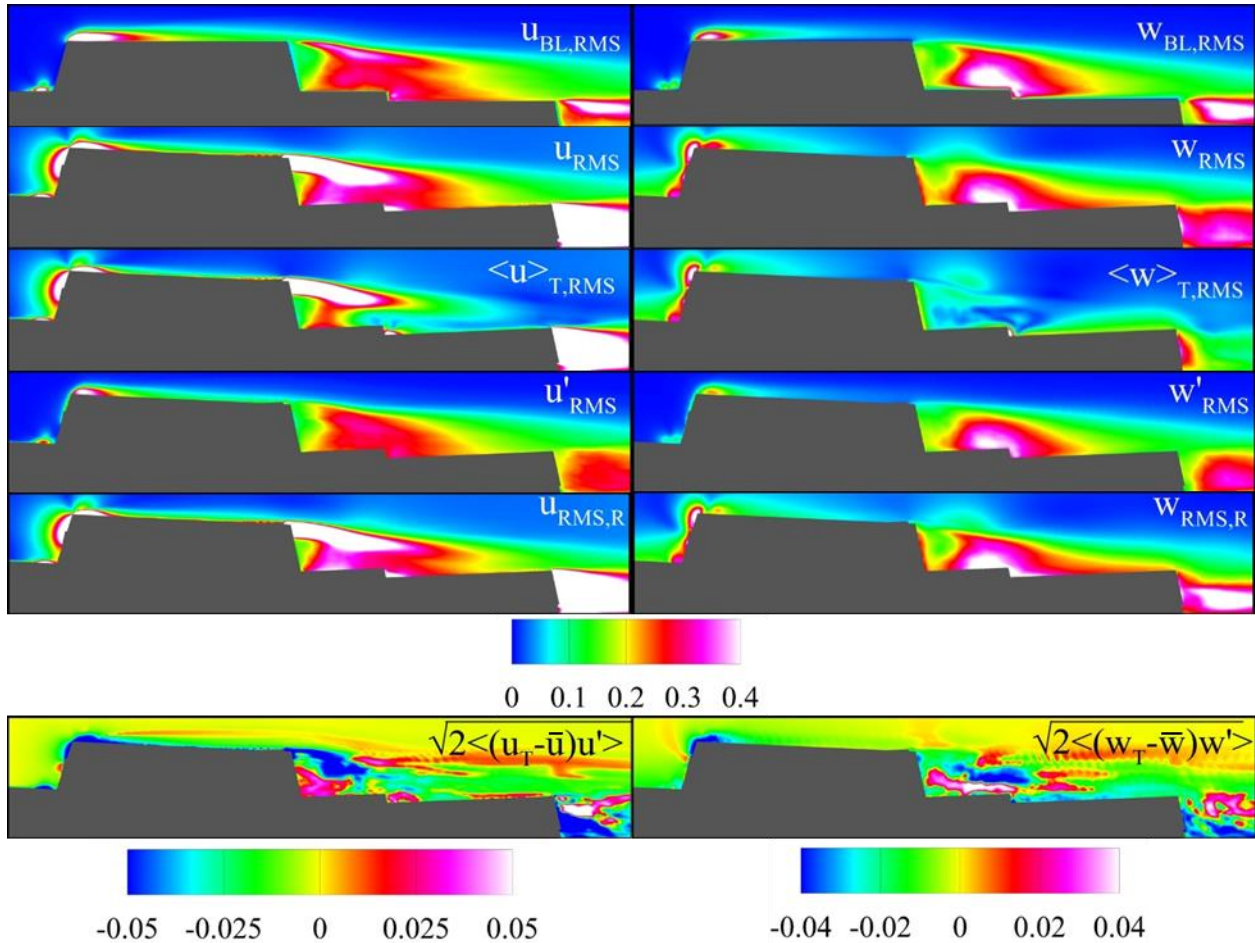
Figure 30: RMS of the fluctuations of streamwise (left) and vertical (right) velocity components for ONRT advancing at 15 knots in 35 knots wind in waves. From top to bottom: RMS of baseline condition (NM/NW/35s), RMS of total velocity, RMS of the phase-averaged velocity, RMS of the turbulent fluctuations, reconstructed RMS, and signed square root of the cross correlation (WM/WW/35s).

Figure 31 shows the same decomposition of the RMS velocity fluctuations for the SS3 condition. For the case with motions and waves (WM/WW/15$_S$) the total RMS velocity fluctuations in the streamwise direction, u_{rms}, shows a very slight increase in the shear layer directly behind the superstructure but also decreases in the recirculation region closer to the deck; this also occurs in the vertical fluctuations w_{RMS}. The RMS of the phase-averaged velocity $< u_T >_{RMS}$ and $< w_T >_{RMS}$ show that the contribution to the fluctuations from motions and waves is significantly less than the SS6 case, as expected. The wave/motion induced fluctuations in the streamwise direction do not extend as far down the length of the flight deck as they did for

the SS6 case, and there is also almost no contribution to the vertical velocity fluctuations above the flight deck. For the case with motions and waves the turbulent fluctuations u'_{RMS} and w'_{RMS} are very similar to the total RMS fluctuations u_{rms} and w_{RMS}, also showing that motions and waves have a very limited contribution. u_{rms} and w_{RMS} can be effectively approximated by $u_{RMS,R}$ and $w_{RMS,R}$, with only slight over predictions of the RMS fluctuations in the regions of the shear layer and in the recirculation region for the streamwise and vertical directions, respectively. This is caused by the decrease in turbulent fluctuations due to the motions and waves, which is not properly accounted for in the linear superposition, as discussed previously. The cross-correlation term shows a very significant decrease in contribution to the total RMS when compared to the SS6 case and does contain numerical noise due to being computed from single-precision solution files. Even with these precision issues clear trends can still be seen, with increase in the cross-correlation term in the regions of the shear layers off the superstructure and the stern. Also, there is a clear decrease when moving out of the region behind the superstructure and into the free stream. The cross-correlation contribution accounts for less than 1% of the total RMS of the velocity fluctuations in the streamwise and vertical directions at the highest levels, which is considerably less than the 10% seen for the SS6 condition.
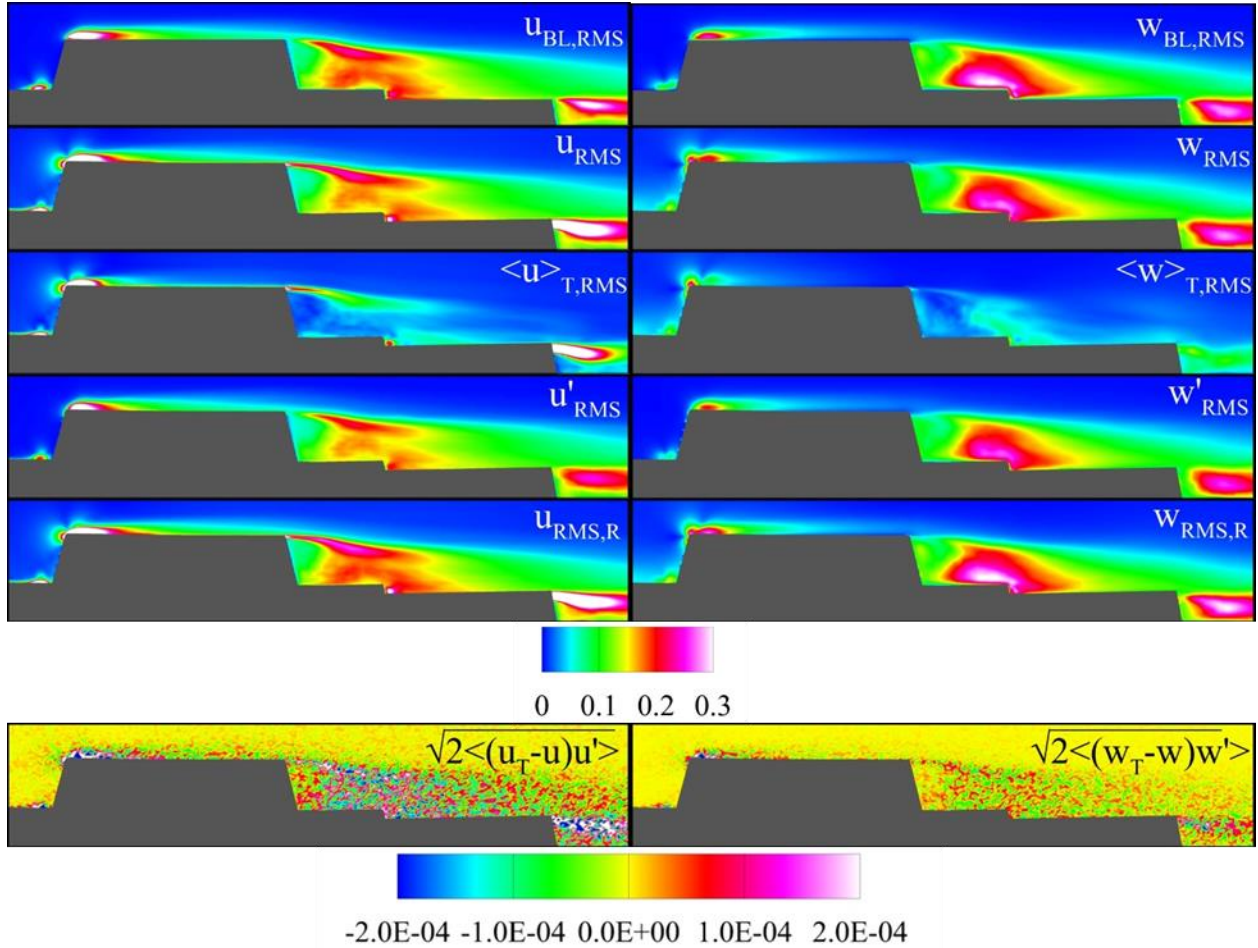
Figure 31: RMS of the fluctuations of streamwise (left) and vertical (right) velocity components for ONRT advancing at 15 knots in 15 knots wind in waves. From top to bottom: RMS of baseline condition (NM/NW/15s), RMS of total velocity, RMS of the phase-averaged velocity, RMS of the turbulent fluctuations, reconstructed RMS, and signed square root of the cross correlation (WM/WW/15s).

The accuracy of the reconstructed RMS fluctuations ($u_{RMS,R}$ and $w_{RMS,R}$) was quantified by computing the difference between these fluctuations and the total RMS fluctuations (u_{RMS} and w_{RMS}),

$$\Delta u_{RMS,R} = u_{RMS,R} - u_{RMS} \tag{16}$$

The results are shown in Figure 32 for both the SS6 and SS3 conditions. The figure shows that for the higher SS6 case larger differences occur in the shear layer, stretching into the flight deck region. For the SS3 condition the largest difference appears in the recirculation region behind the

56

superstructure where the reconstructed fluctuations over predict the actual fluctuations. In the region of the flight deck the error in the reconstructed RMS is larger for SS6 condition, which is under predicted by -0.035U (0.9 knots) in the shear layer region above the mid flight deck location. This equates to approximately 30% local error. The error comes from this region being exposed to both low levels of turbulent fluctuations in the free stream and high levels of turbulent fluctuations in the recirculation region as the ship pitches and heaves. This analysis shows that RMS fluctuations due to motions and waves cannot be recovered by taking the linear superposition of the baseline (static) turbulent fluctuations and the fluctuations directly attributed to motions and waves to recover the total fluctuations when the ship is operating in waves with resulting motions, due to the non-linearity of the problem. This error in the reconstruction may not be of importance for larger craft such as the SH-60 as it attributed to higher frequency fluctuations.
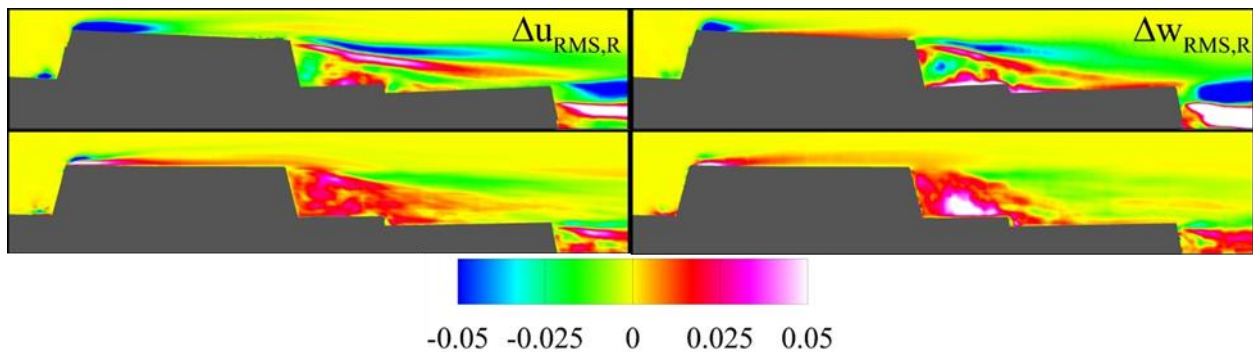
Figure 32: Difference between reconstructed RMS and RMS of total velocity for SS6 (top row) and SS3 (bottom row).

4.3.3 Velocity decomposition above the flight deck

In order to study the effects of waves and motions on the phase-averaged streamwise and vertical velocities a single test point was analyzed more in depth. This point is located 30 ft above the mid-flight deck of the static ship and is relevant for a helicopter hovering or approaching before landing. The point is also located close to the shear layer, which separates

57

the wake and free stream. The phase-averaged velocities $< u_T >$ and $< w_T >$ for three encounter periods are shown in Figures 33 and 34, respectively, for 35 knots wind condition (SS6), and in Figures 35 and 36, for 15 knots wind conditions (SS3). As mentioned in §4.1.2, proper convergence at each phase would require significantly more computational time so a low pass filter was used to remove any high frequency fluctuations still remaining in the phase-averaged velocity signal.

For the case with the milder motions in SS3, the peak-to-peak amplitude of the streamwise velocity with waves and motions (labeled WM/WW in the figures) reaches $0.07U$ (Figure 35), increasing to $0.25U$ for the case with larger waves and motions in SS6 (Figure 33). These corresponds to $0.059U_{rel}$ and $0.125U_{rel}$ for SS3 and SS6, respectively. Overall, the motion-induced fluctuations seen in the smaller waves (SS3) are less than 2 knots peak-to-peak in streamwise velocity and 1 knot peak-to-peak in vertical velocity, small enough to be handled by most aircraft.

Waves alone affect the streamwise velocity considerably for the SS6 case. In Figure 33 it is shown that waves affect the streamwise velocity in counter phase with the motions. As expected, in the case with motions and no waves (WM/NW) when the deck rises the shear layer translates upward and the test point is more deeply submerged into the wake, resulting in a decrease in streamwise velocity. The opposite effect occurs when the deck sinks. In the presence of waves only (NM/WW), as the wave crest passes the flight deck there is an acceleration of the flow that lowers the location of the shear layer, resulting in an increase of the streamwise velocity at the test point. As a result of the competing effects of waves and motions, the case with motions and waves (WM/WW) exhibits a smaller velocity fluctuation amplitude than the case with only motions, 6.25 knots versus 10 knots. This relates to what was mentioned in §4.3.2

58

(Figure 23) where it was shown that larger streamwise fluctuations reached farther into the flight

deck region for the case with only motions. The same trend is not shown in the SS3 case but the

effects from waves are very small at 30 ft above the flight deck and the overall streamwise

fluctuations are considerably smaller. This makes it difficult to isolate where the difference in

fluctuations between the WM/NW and WM/WW cases is coming from. Phase-averaged vertical

velocities in SS6, shown in Figure 34, are in phase for the cases NM/WW, WM/NW, and

WM/WW, but the individual effects of waves and motions do not add up linearly. The peak-to-

peak amplitude of the vertical velocity fluctuations induced by waves and motions is

approximately 2.5 knots, in phase with the displacements of the flight deck.
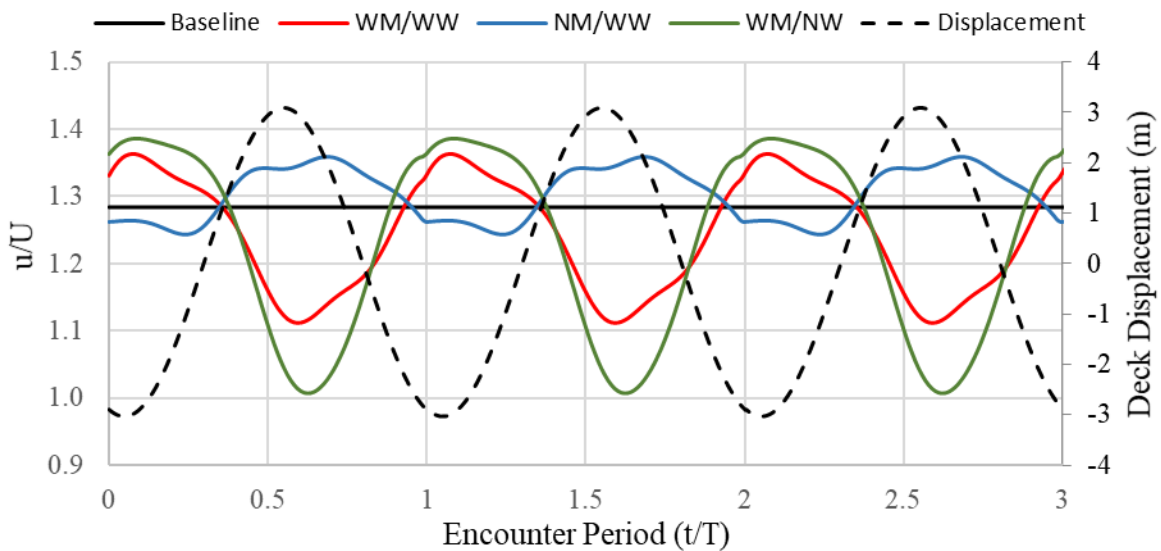
Figure 33: Phase averaged velocity ($<u>_T$) at a point 30 ft above the mid-flight deck location for all cases with a ship speed of 15 knots and wind speed of 35 knots (NM/NW/35$_S$, WM/WW/35$_S$, NM/WW/35$_S$, WM/NW/35$_S$).
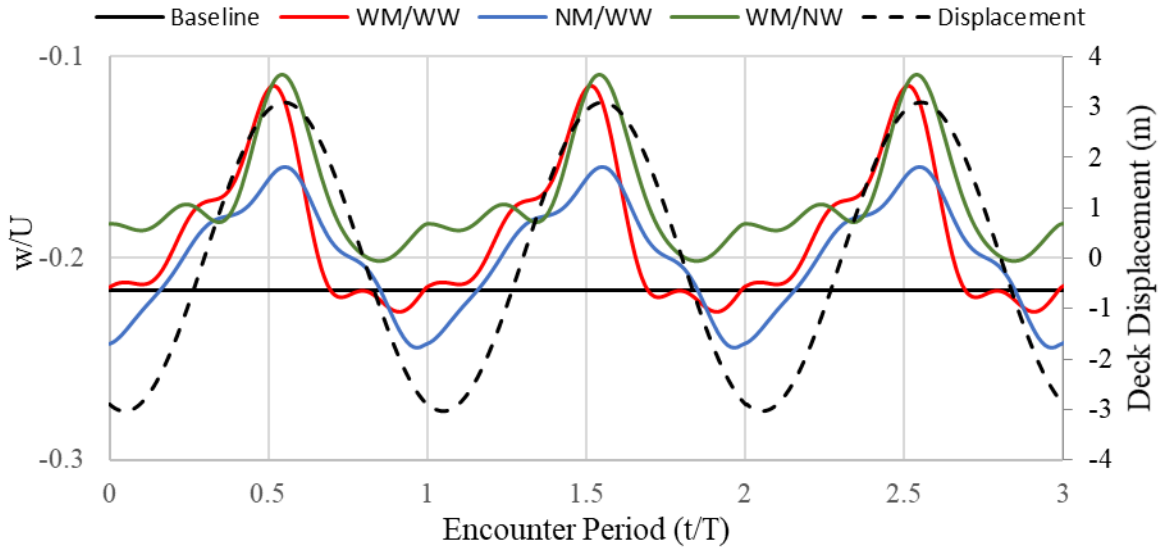
Figure 34: Phase averaged velocity ($<w>_T$) at a point 30 ft above the mid-flight deck location for all cases with a ship speed of 15 knots and wind speed of 35 knots (NM/NW/35$_S$, WM/WW/35$_S$, NM/WW/35$_S$, WM/NW/35$_S$).
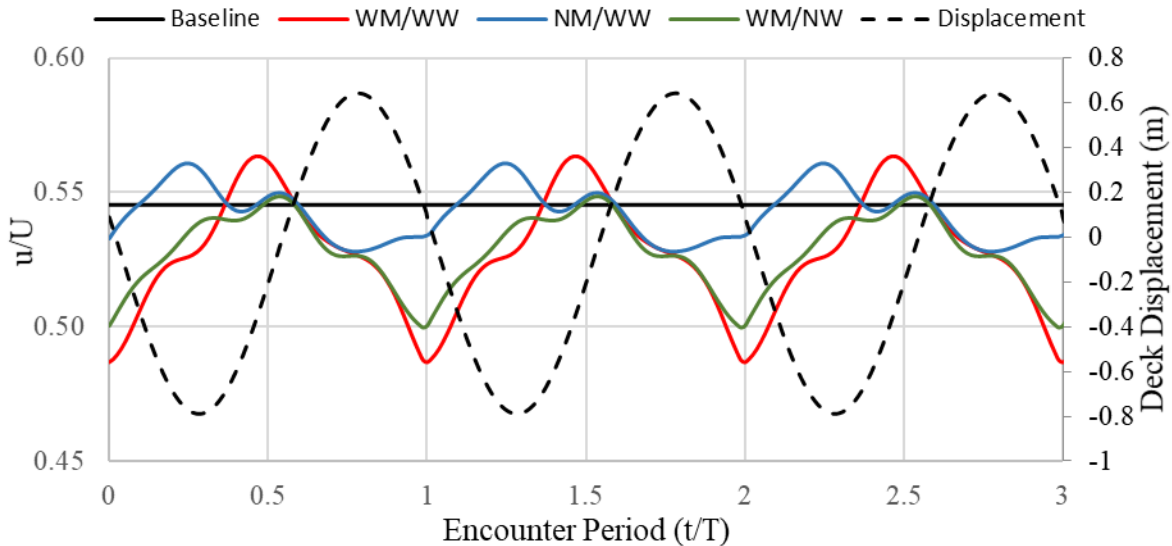
Figure 35: Phase averaged velocity ($<u>_T$) at a point 30 ft above the mid-flight deck location for all cases with a ship speed of 15 knots and wind speed of 15 knots (NM/NW/15$_S$, WM/WW/15$_S$, NM/WW/15$_S$, WM/NW/15$_S$).

60
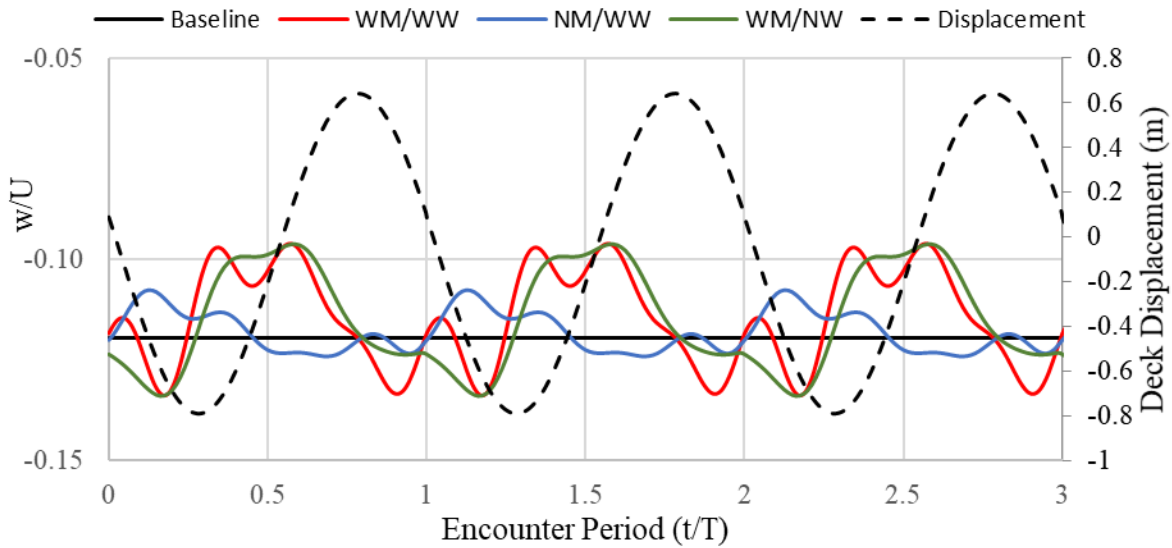
Figure 36: Phase averaged velocity ($<w>_T$) at a point 30 ft above the mid-flight deck location for all cases with a ship speed of 15 knots and wind speed of 15 knots (NM/NW/15$_S$, WM/WW/15$_S$, NM/WW/15$_S$, WM/NW/15$_S$).

In order to see how the position of the point with respect to the ship changes the effects of motions and waves, the same phase-averaged plots are shown in Figures 37 and 38 for a point 22 ft above the flight deck for the 35 knots wind condition (SS6). The lower point experiences slower and more negative average streamwise and vertical velocities, respectively, as the point is deeper into the wake of the superstructure. Figure 37 shows that the phase-averaged streamwise velocity experiences the same trends shown for the 30 ft point in Figure 33, but at this point the peak-to-peak fluctuations for the NM/WW case are significantly higher. The comparison shows that as the free surface moves closer to the test point its local streamwise velocity is much more affected by the waves, as expected. The opposite is true for in the vertical velocity, as the peak-to-peak fluctuations for the NM/WW decrease significantly for the 22 ft point. It is presumed that the vertical velocity fluctuations are dominated by the ship motions and not the wave motion/deformation as you move close to the flight deck. This is shown in Figure 38 as the WM/WW case is very similar to the WM/NW.

61
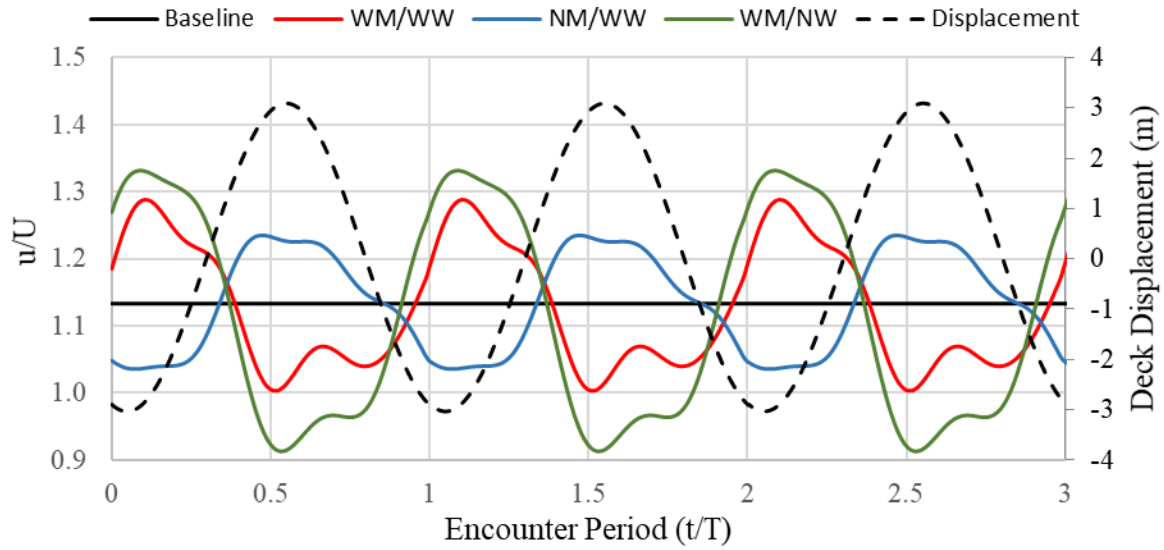
Figure 37: Phase averaged velocity ($<u>_T$) at a point 22 ft above the mid-flight deck location for all cases with a ship speed of 15 knots and wind speed of 35 knots (NM/NW/35$_S$, WM/WW/35$_S$, NM/WW/35$_S$, WM/NW/35$_S$).
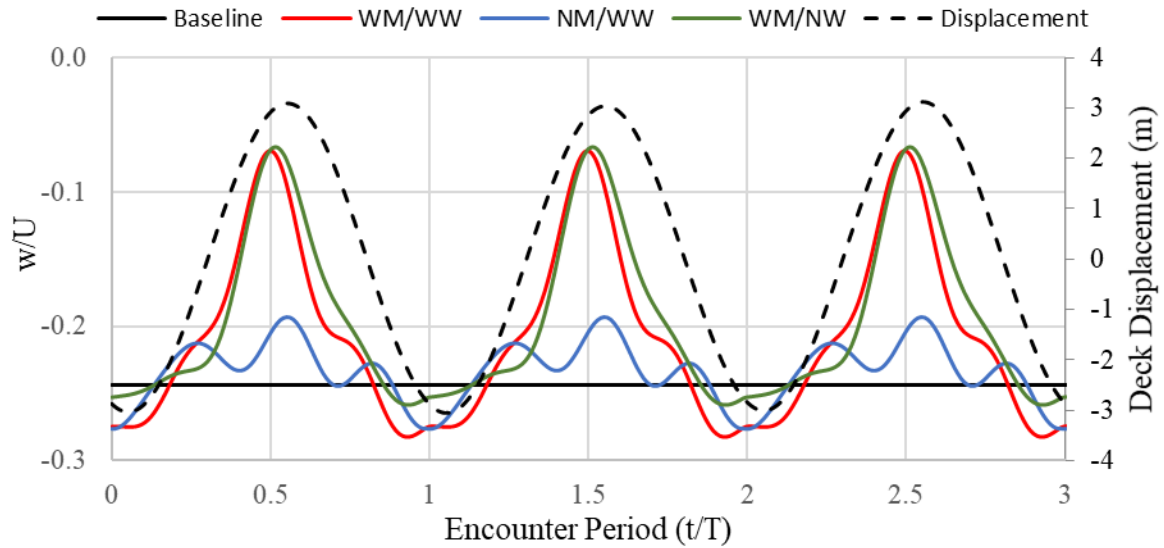
Figure 38: Phase averaged velocity ($<w>_T$) at a point 22 ft above the mid-flight deck location for all cases with a ship speed of 15 knots and wind speed of 35 knots (NM/NW/35$_S$, WM/WW/35$_S$, NM/WW/35$_S$, WM/NW/35$_S$).

Chapter 5. EFFECTS OF WAVES AND MOTIONS ON A HELICOPTER

5.1 Simulation Design and Setup

5.1.1 Geometries and conditions

The operation of a helicopter in the region of the ONRT flight deck was analyzed in order to better quantify the effects of wave-induced motions on the dynamic interface. For the simulations studying the effects on helicopter operation a generic helicopter based on the US Navy Sikorsky SH-60 Seahawk was used as the test aircraft, shown in Figure 39. The geometry is significantly simplified in order to reduce computational cost and discretization complexity. The basic dimensions and rotor speeds for the helicopter can be found in Table 8. This type of aircraft commonly operates on surface combatants similar to the DDG-1000 making the coupled simulation realistic to real world operations.
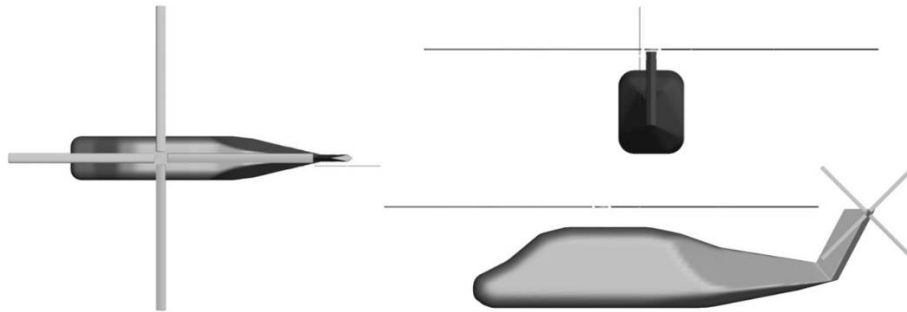
Figure 39: Generic helicopter model used for simulations, based on the Sikorsky SH-60 Seahawk.

Table 8: Helicopter model dimensions and operational conditions. Model dimensions are based on the Sikorsky SH-60 Seahawk.

Length (m)		16.23
Width (m)		2.36
Height (m)		5.18
Gross Weight (kg)		8,739
Rotor Diameter (m)	Main	16.36
	Tail	3.35
Rotor Speed (RPS)	Main	4.3
	Tail	12.9

The same methodology discussed in §4.1.2 is used for the simulations shown in Table 9 and the sea state conditions tested are the same as those shown in Table 5. For all the cases the helicopter is fixed at a position 30 ft (9.144 m) above the static ship's flight deck, this position is maintained for the free helicopter cases as well. When the ship is free to pitch and heave the location of the helicopter with reference to the ONRT changes as its flight deck moves up and down with the head waves. Though the forces exerted on the ship by the helicopter down wash are resolved the forces are much smaller than those exerted by the water, resulting in motions that are almost identical for the cases with and without the helicopter (see Figure 18). The helicopter main and tail rotors operate at fixed rotational speeds, with the main rotor collective pitch of 13.3 degrees set such that thrust and weight balance with the helicopter operating behind the ONRT in 35 knots head wind and the tail pitch is set at a fixed pitch of 3.15 degrees, to guarantee that it produces thrust reacting to the airwake. These main and tail rotor pitch angles are then kept consistent for all the other cases. No cyclical is applied to the main rotor pitch, this results is a net axial and side force on the body.

The full simulation matrix is shown in Table 9. The helicopter alone was simulated for both wind speed conditions in order to establish a baseline for the forces on the body when it is operating away from the ship. For the cases with the helicopter geometry only the same 15 knots velocity against the wind is imposed, this is done to preserve the same relative velocity between the free surface and the wind. The no motions or waves cases with only the helicopter differ from the other baseline conditions as the single-phase level set approach in REX neglects the effect of air flow in the water, so the free surface is not affected by the helicopter downwash for these simulations.

64

Table 9: Simulation matrix for studying effect of waves and motions on a helicopter.

Case	U_{Ship} (knots)	U_{Wind} (knots)	Relative Speed (knots), Re	Motions/Waves	Case Name
ONRT + Helicopter	15	15	30 1.6×10^8	No Motions/No Waves	Baseline: NM/NW/15_{S+H}
				Predicted/SS3	WM/WW/15_{S+H}
		35	50 2.6×10^8	No Motions/No Waves	Baseline: NM/NW/35_{S+H}
				Predicted/SS6	WM/WW/35_{S+H}
Helicopter	15	15	30 1.6×10^8	No Motions/No Waves	NM/NW/15_H
		35	50 2.6×10^8	No Motions/No Waves	NM/NW/35_H

5.1.2 Simulation design
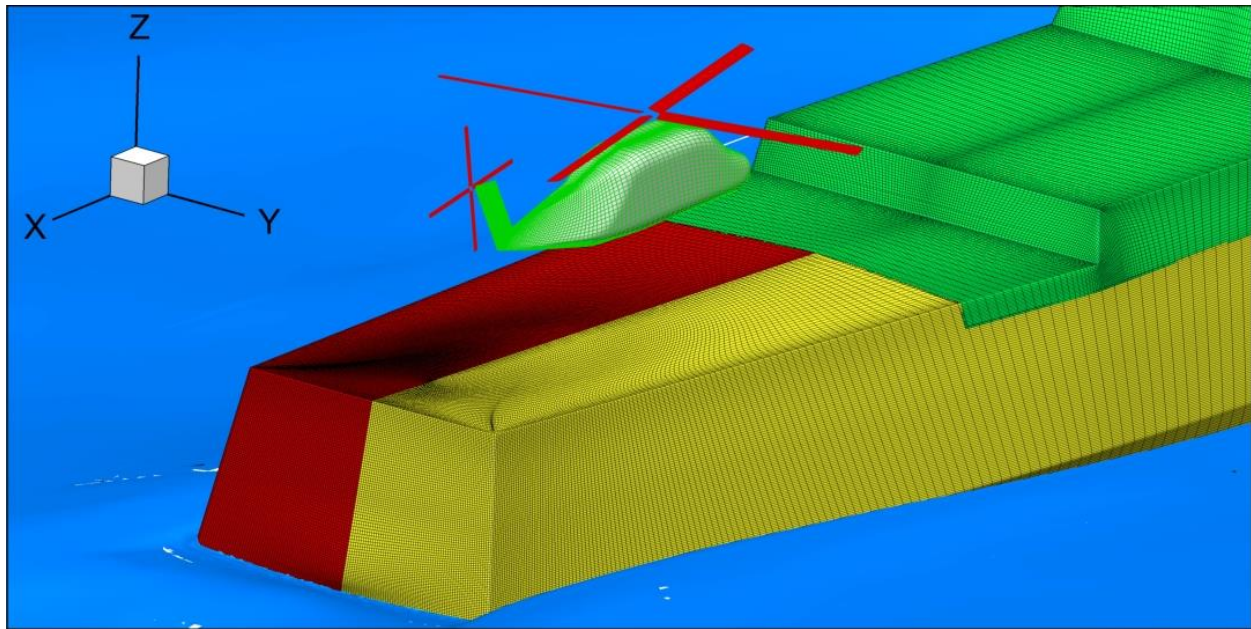
Figure 40: Overset grid topology for the helicopter geometry with the ONRT geometry overset.

For the "ONRT + Helicopter" cases all the grids used in the "ONRT" cases, see Table 7, are maintained with the addition of 19 structured blocks. The additional grids include two double-o grids for the starboard and port sides of the helicopter fuselage, 8 double-o grids for the pressure and suction sides for each of the four main rotor blades, 8 double-o grids for the pressure and suction sides for each of the four tail rotor blades, and one Cartesian refinement

65

around the helicopter. For the "Helicopter" cases all the same grids are used with exception of the hull grids, superstructure and the free surface refinement. The "ONRT + Helicopter" cases, which contain all 25 structured blocks, have a total of 78M grid points. All the grids used for these simulations are listed in Table 10 and the overset grid used for the helicopter geometry is shown in Figure 40.

Table 10: Grid system used to simulate the ONRT along with the helicopter.

Grid	Dimensions	Reference Frame	Size
Port Hull	397 x 121 x 207	Ship	9.9M
Starboard Hull	397 x 121 x 207	Ship	9.9M
Superstructure	329 x 101 x 169	Ship	5.6M
Port Fuselage	151 x 61 x 51	Helicopter	0.5M
Starboard Fuselage	151 x 61 x 51	Helicopter	0.5M
Main Rotor Pressure	4 x 101 x 61 x 51	Helicopter	4 x 0.3M
Main Rotor Suction	4 x 101 x 61 x 51	Helicopter	4 x 0.3M
Tail Rotor Pressure	4 x 101 x 61 x 51	Helicopter	4 x 0.3M
Tail Rotor Suction	4 x 101 x 61 x 51	Helicopter	4 x 0.3M
Helicopter Ref.	181 x 151 x 101	Earth	2.7M
Airwake Ref.	739 x 245 x 152	Earth	27.5M
Free Surface Ref.	384 x 92 x 140	Earth	4.9M
Background	256 x 179 x 239	Earth	10.9M

For the simulations with the helicopter the time step was set based on the rotational speed of the main and tail rotors as well as the wave encounter frequency. The time step was set such that the main rotor rotates approximately 2 degrees per time step and the tail rotor rotates 6 degrees per time step. Past grid studies show that the azimuthal advance per time step for the main rotor is consistent with appropriate simulation of marine propellers (Chase and Carrica 2013), and similar to the main and tail rotor values of 1 and 5 degrees per time step used by Crozon et al. (2018) for a Sea King Helicopter. The time step was then slightly modified to ensure that one wave encounter period is resolved by an integer number of time steps. This resulted in a dimensionless time step of roughly 10^{-4} for each of the cases. Each time step results

66

in the encounter period being resolved by between 6000 and 6800 time steps for SS3 and SS6, respectively. Volume solutions were written every 50 time steps, resulting in 120 or 136 volume solutions per encounter period. As discussed by Crozon et al. (2018), the time step restriction imposed by the helicopter rotors makes the computations very expensive, limiting the number of conditions that could be tested. Each of the simulations with ONRT and helicopter in waves took approximately 300,000 total CPU hours to complete. The simulations with only the ship do not have the time step restriction imposed by the helicopter rotors, for these simulations the time step is simply set based on the wave encounter period. The simulations with motions and waves were run for 13 encounter periods, 10 of which were used for analysis, based on the high computational expense for each of the simulations. As mentioned previously, hundreds of encounter periods would need to be computed in order to compute phase dependent statistics properly, which is not feasible at this time.

5.2 One-way Coupling

One-way coupling is a simplified approach which uses the simulated flow behind the ship and a disk actuator model of the helicopter rotor to predict the thrust produced by a specified rotor. The one-way coupling was used to measure the effects of waves and motions on three different rotor sizes, all having the same geometry with only different diameters. The geometry and largest rotor size are from the generic SH-60 Seahawk with dimensions shown in Table 8. Two smaller rotors were studied as well with rotor diameters of 50% (8.17 m) and 4.5% (0.74 m) of the SH-60 diameter. The medium sized rotor (50%) is representative of a Robinson R22 helicopter and the smallest (4.5%) an autonomous drone. This approach ignores any effects from the fuselage as well as the interaction between the rotor downwash and the airwake.

5.2.1 One-way coupling methodology

Performance curves for the rotor were obtained from the CFD computations for different blade angles α and advance coefficients J, defined as

$$J = \frac{w}{nD} \tag{17}$$

where w is the local advance velocity (vertical velocity unaffected by the rotor), and n and D are the rotor rotational speed in revolutions per second (RPS) and diameter, respectively. For this approach horizontal velocity effects on rotor performance are ignored. The thrust coefficient, is then computed as

$$K_T(J, \alpha) = \frac{T}{\rho n^2 D^4} \tag{18}$$

where T is the vertical rotor thrust. The reference hovering thrust coefficient in no wind condition ($K_{T,0}$) is obtained using $J = 0$ and finding the collective pitch angle that produces thrust equal to the standard operational weight for the SH-60 Seahawk, 8739 kg. The same pitch angle is then used for the smaller rotors as well. Rotational speeds of the smaller rotors increase as a function of the diameter size and were computed as

$$n = \frac{n_{SH60}}{(D/D_{SH60})} \tag{19}$$

in order to maintain the same average K_T.

Figure 41 shows the performance curve and iso-surfaces of Q-criterion displaying vortical structures for two advance coefficients with a blade pitch of 6 degrees. From $J = -0.2$ to -0.08 the rotor operates in vortex ring state (VRS), an unstable condition characterized by the formation of a large vortex directly above the rotor, separate of the rotor tip vortices. This condition results in large instabilities where lift decreases sharply as the descent velocity (or

68

external upward flow) increases, further decreasing lift until a new equilibrium condition develops at a much lower advance coefficient.
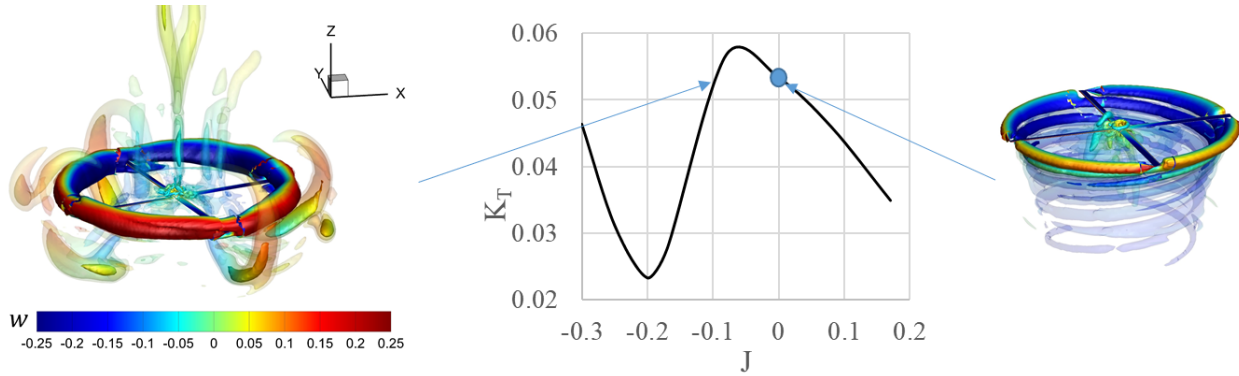
Figure 41: Performance curve and vortical structures for J=-0.08 (left) and J=0 (right) for α=6 degrees.

The idealized uniform flow condition used to compute the performance curve does not occur in the highly turbulent wake of a ship. As a first approximation, it is assumed that every section in the rotor disk has a local performance curve as shown in Figure 41, and using the instantaneous velocity field from the full-scale ONRT simulations a local advance coefficient is computed at every point over the entire disk area for each time step. Using the performance curve along with the local advance coefficient a local thrust coefficient is obtained. Weighting based on disk actuator theory is determined for each point using the equation

$$w_i = \frac{r_i\sqrt{1-r_i}}{\sum_{i=1}^{N} r_i\sqrt{1-r_i}} \tag{20}$$

where r_i is the local radius, so the weighting only varies in the radial direction of the disk. The total thrust produced by the disk at each time step is then computed using the local weight coefficient and thrust coefficient as shown below.

$$T = \sum_{i=1}^{N} w_i K_i^T \rho n^2 D^4 \tag{21}$$

69

This methodology is shown in Figure 42, which shows the baseline average of the local advance and thrust coefficients for the case with no motions and the quarter phase-averages for the condition with the ONRT advancing at 15 knots in 35 knots head winds (SS6). The figure shows how the local K_T varies over the area of the disk based on the corresponding local J value. Figure 42 also shows a clear increase in K_T values for the 180 degree phase, this phase corresponds to the flight deck moving in the positive vertical direction. The smaller magnitude vertical velocities induced by the ship at this phase (Figure 24) result in the increase in K_T.
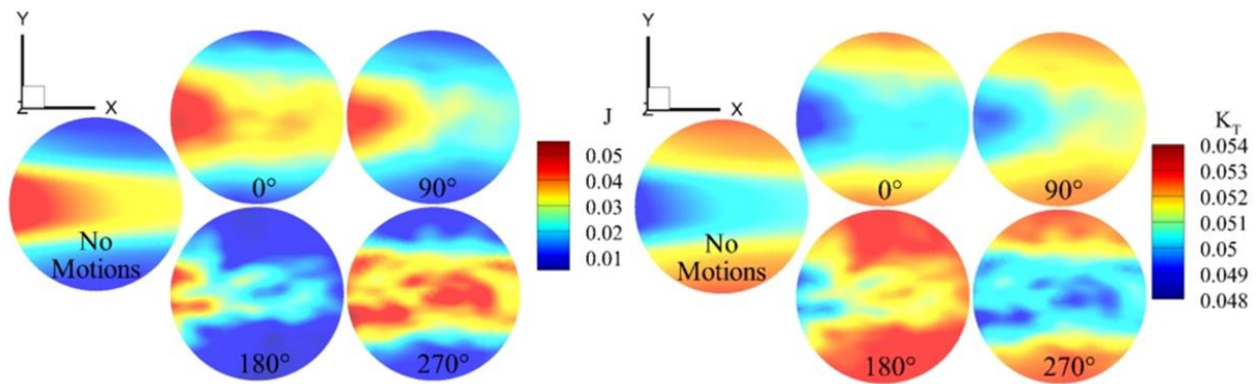
Figure 42: Local advance (left) and thrust (right) coefficients on the rotor disk of diameter D for the case with no motion (NM/NM/35$_S$, left) and for the four quarter phases for the case with motions (WM/WW/35$_S$, right).

5.2.2 Effects of motions/waves and rotor size

Figure 43 show scatter plots representing the average advance coefficient and thrust coefficients of the rotor disk for every five time steps (10.71 Hz) of the ONRT advancing at 15 knots in 35 knots head winds (SS6), for the larger rotor corresponding to the SH-60 helicopter, and for the smaller rotors of the R22 and drone. Both plots show that variations in advance coefficient over the disk surface do not result in any extreme variation in thrust as K_T mostly follows the performance curve. The effects of motions on the SH-60 rotor can be seen on the left as the distribution of J and K_T values increases noticeable for the case with motions. The RMS of the K_T fluctuations increases from 2.7×10^{-4} for the baseline case (NM/NW/35$_S$) to 5.9×10^{-4} for

70

the same wind speed with motions and waves (WM/WW/35$_S$). This level of fluctuations does not result in negative advance coefficients as the average vertical velocity remains negative (J>0) and VRS does not occur. The plot on the right shows the effect of rotor size on the thrust fluctuations seen while operating behind the ONRT with motions and waves. The small rotor, with a disk size that is comparable to the size of turbulent structures detached from the superstructure, experiences negative advance coefficients in the VRS range. This is not due to any movement in the blade itself, but the ascending flow induced by ship motions and turbulence.
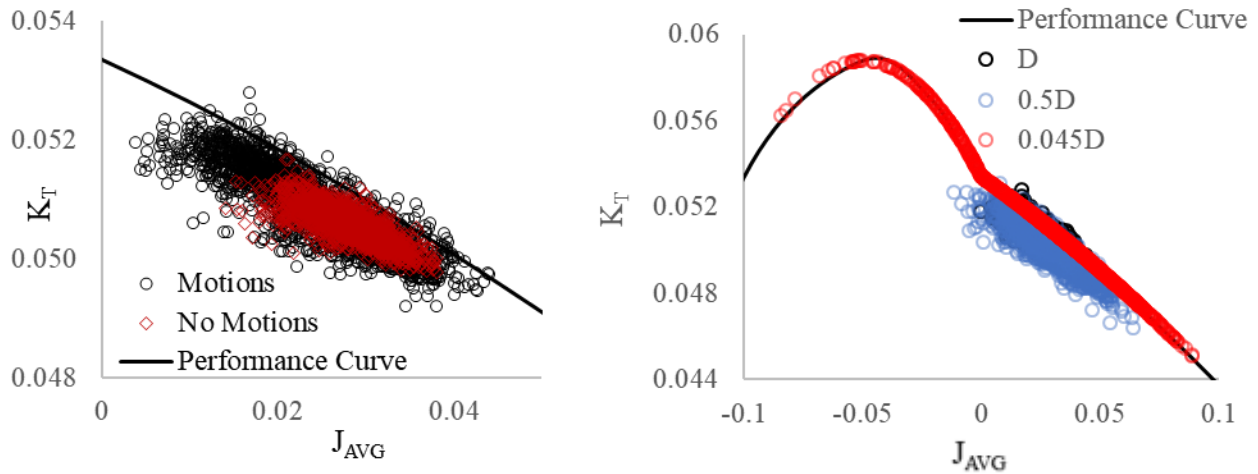
Figure 43: Actual performance curve for non-uniform flow field for a rotor corresponding to SH-60 (diameter D) for baseline (NM/NW/35$_S$) and in SS6 waves (WM/WW/35$_S$, left) and in SS6 waves (WM/WW/35$_S$) for diameters D, 0.5D and 0.045D (right).

The time history of the total thrust over several encounter periods is shown in Figure 44, for all rotors operating in the airwake of the ONRT in waves (WM/WW/35$_S$). The vertical force is normalized by T_0, the reference thrust in the absence of external flow with that same blade pitch angle. The figure shows that all rotors experience a decrease in average thrust, as $J > 0$ due to the presence of an average downflow from the ship airwake. All blade sizes show a clear fluctuation in thrust that is similar to the 8.85s wave encounter period for the ONRT advancing at 15 knots in SS6 waves. Thrust fluctuation amplitudes reach approximately ±2% of T_0 for the

71

largest rotor, +2/-5% for the intermediate rotor and +11/-9% for the smallest rotor. Increases in thrust correspond to positive displacement in the flight deck (pitching down) and results in higher frequency fluctuations for the smaller rotor as the rotor is fully immersed in the turbulent airwake. The same behavior is not seen in the larger rotors as these smaller scale turbulent structures are filtered out over the larger rotor disk area, this phenomenon is clearly shown in Figure 45. The power spectrum density (PSD) of the normalized thrust fluctuations for all rotor sizes is shown in Figure 45, as the sample frequency is 10.71 Hz the highest frequency that can be resolved is 5.35 Hz (Nyquist frequency). All rotor sizes show a clear peak at the wave encounter frequency (f_e = 0.118 Hz) as well as twice f_e. This second harmonic could be due to a less negative vertical velocity which takes place twice per encounter period (Figure 24); in general, it can also be an expression of the decomposition of the complex, non-sinusoidal velocity field. As mentioned previously the smallest dimeter rotor is much more affected by the high frequency small scale fluctuations in the airwake which is shown in Figure 45 as the spectral energy density decays much slower at higher frequencies in comparison to the two larger rotors. The same trend is seen comparing the decay of the R22 (0.5D) rotor to the SH-60 (D).
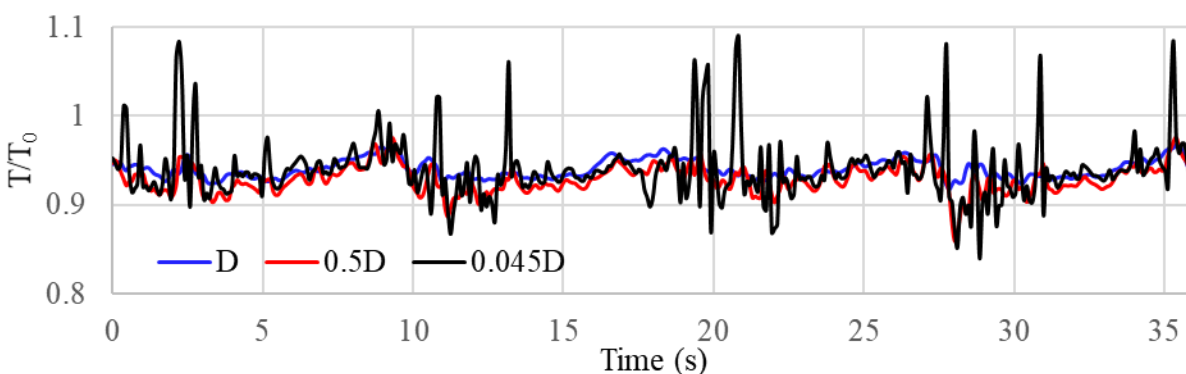
Figure 44: Thrust fluctuations for a helicopter hovering 30 ft (9.144 m) above the center of the flight deck for ONRT advancing at 15 knots in 35 knot winds in waves (WM/WW/35$_S$).
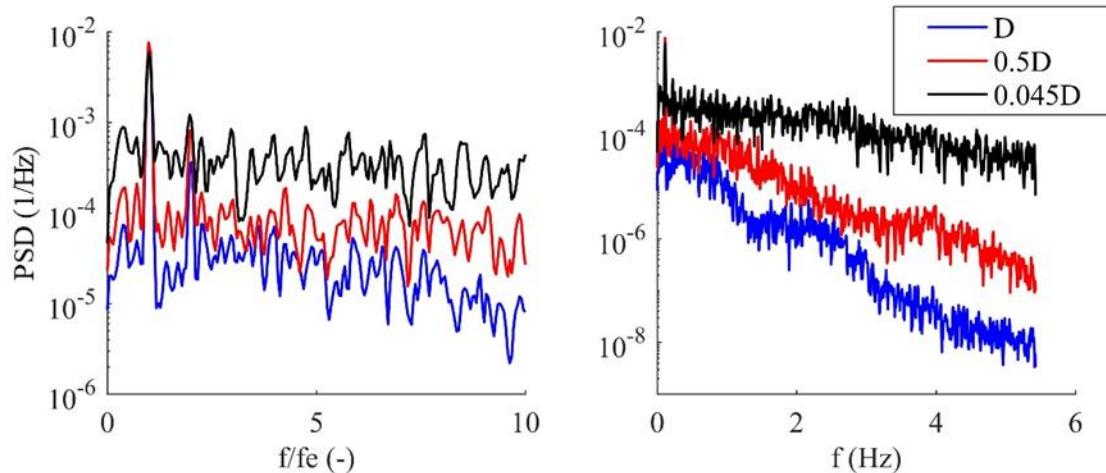
Figure 45: Frequency response corresponding to T/T_o in Figure 44 (WM/WW/35$_S$).

5.3 Two-way Coupling

In this section analysis focuses on the generic SH-60 helicopter operating 9.144 m (30 ft) over the flight deck of ONRT for the nominal conditions in SS3 and SS6 described in Table 5. In this case the helicopter operational weight used is 8,739 kg. Notice that since no cyclical or tail rotor control is applied the helicopter is not in equilibrium, resulting in non-zero side and streamwise forces and roll, pitch and yaw moments. Since this study is interested in analyzing mostly fluctuations around the reference state with the helicopter operating in uniform flow (no turbulence, no ship airwake), ignoring these forces is reasonable.

5.3.1 Flow field effects

Instantaneous views of the flow field for each of the quarter phases for the helicopter hovering over the flight deck of the ONRT in SS6 (WM/WW/35$_{S+H}$) and SS3 (WM/WW/15$_{S+H}$) conditions is shown in Figure 46. The pictures display the interaction between the helicopter and the ONRT airwake as structures can be seen being pulled in to the main rotor blades throughout the wave cycle. For the higher sea state (SS6) a large change in location of the helicopter with respect to the ship can be seen throughout the wave encounter period, periodically exposing the helicopter to more or less structures generated by the ship's superstructure. Overall, the large tip

73

vortices and other structures generated by the helicopter do not appear to be heavily affected by

the ship motions and remain somewhat constant throughout the wave encounter period.
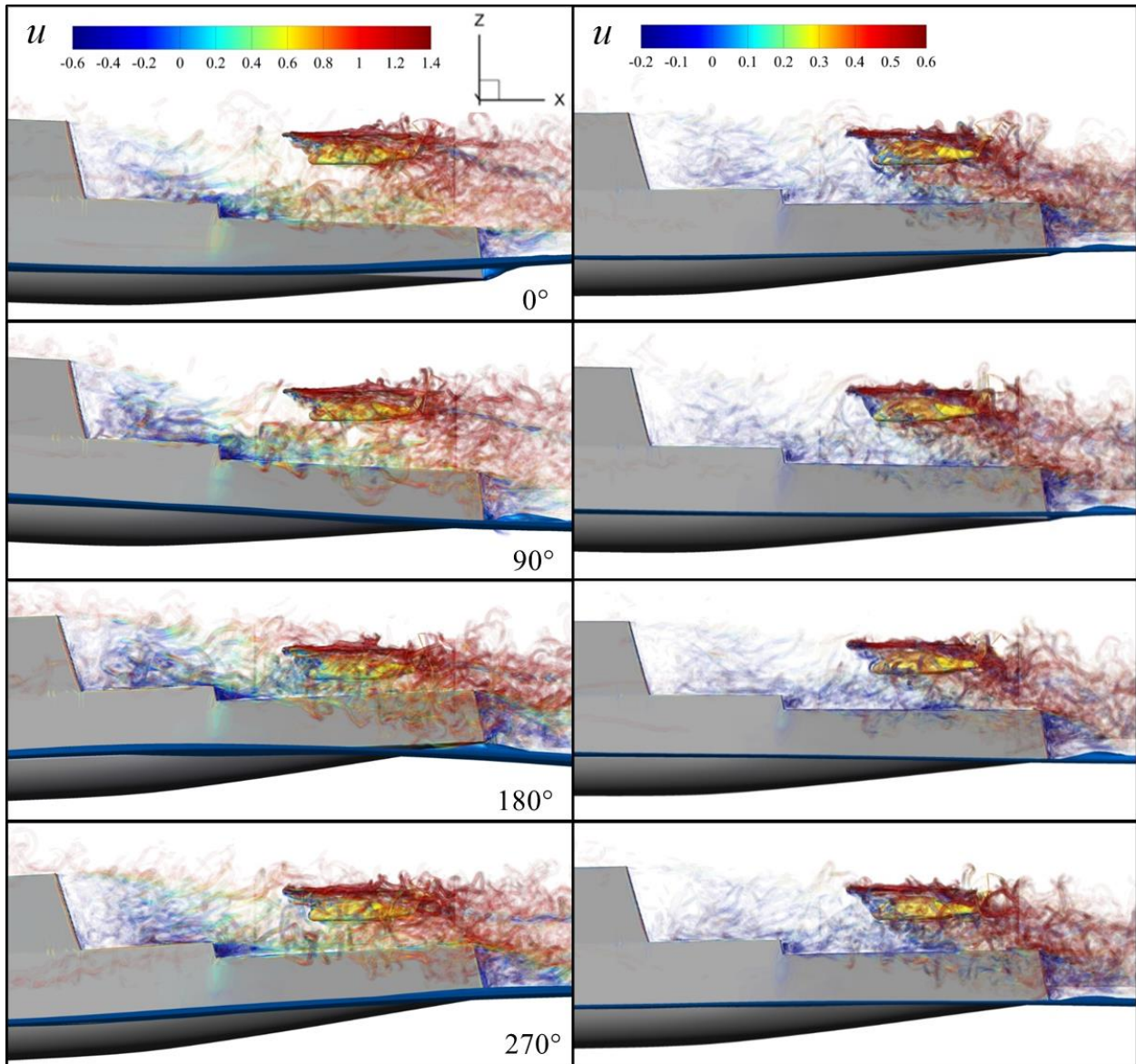
Figure 46: ONR Tumblehome and helicopter advancing at 15 knots into 35 knots head wind (WM/WW/35$_{S+H}$, left) and 15 knots head wind (WM/WW/15$_{S+H}$, right). The four quarter phases are shown from top to bottom. Four iso-surfaces of Q from 5000 to 150000 are used to visualize vortical structures.

Figures 47 and 48 show the phase-average velocities ($< u_T >,< w_T >$) for the quarter phases as well as the baseline average velocities ($< u_{BL} >,< w_{BL} >$) for the ONRT advancing at 15 knots into either 15 or 35 knots head wind (SS3 and SS6). By comparing these figures to those without the helicopter (Figures 24 and 25) it can be seen that flow induced by the helicopter rotors modifies the airwake significantly. An immediate consequence of the presence of the helicopter is the suction of fluid from the free stream by the main rotor, causing a high streamwise velocity wake downstream of the helicopter for both cases. Strong negative downflow is also induced by the main rotor pressure side. The main rotor ingests some of the airwake flow which extends the recirculation region further away from the ship's deck. The large vertical velocity seen above and in front of the helicopter for each case is caused by the large tip vortices generated by the main rotor blades. The average flow field for SS3 is not significantly changed throughout the wave encounter period and is very similar to the baseline condition due to the small ship motions, this is not the same for the SS6 condition. The helicopter can be seen moving in and out of the large shear layer shed from the superstructure, changing the streamwise velocity seen by the main rotor from 0.5-1.2U. Similar behavior is shown in the vertical velocity averages, as the ship pitches downward (flight deck moving up) during the 90 to 180 degree phases the vertical velocity near the ship changes from negative to positive, approximately $\pm 0.2U$. Comparing Figures 47 and 48 it can be seen that the angle at which the main rotors downwash is convected away from the fuselage is related to the relative velocity between the ship/helicopter and the head wind (U_{rel}), as expected. The more vertical angle of the downwash for the slower speed case (U_{rel} = 30 knots) may lead to more interaction with the ship airwake.

75

Figure 47: Phase-averaged streamwise (left) and vertical (right) velocities for the four quarter phases for SH-60 and ONRT advancing at 15 knots in 15 knots wind in waves with motions (WM/WW/15$_{S+H}$). The baseline condition is shown at the bottom (NM/NW/15$_{S+H}$).

Figure 48: Phase-averaged streamwise (left) and vertical (right) velocities for the four quarter phases for SH-60 and ONRT advancing at 15 knots in 35 knots wind in waves with motions (WM/WW/35$_{S+H}$). The baseline condition is shown at the bottom (NM/NW/35$_{S+H}$).

Figures 49 and 50 show the phase-averaged RMS of velocity fluctuations ($< u_{T,RMS} >, <$ $w_{T,RMS}$) and the baseline RMS of velocity $(< u_{BL,RMS} >, < w_{BL,RMS} >)$ for SS3 and SS6, respectively. For the SS3 condition the RMS induced by the helicopter is significantly higher than that of the ship airwake. The airwake RMS of the both the streamwise and vertical directions only reaches approximately $0.3U$ in the region of strong recirculation directly behind the superstructure of the ship while the RMS of rotor downwash is $>0.4U$ in both directions. Moving to the higher SS6 condition the RMS fluctuations of the flow upstream of the helicopter is more comparable in magnitude to those downstream. For the phases with the ship pitching up (0/90 degrees) the helicopter is the furthest away from the ship and the RMS of the flow ahead of the helicopter is approximately 0.2-$0.3U$. When the ship is pitching down (180/270 degrees) the helicopter is closest to the flight deck and the RMS in both directions increases significantly. As the helicopter moves closer to the flight deck there is much more interaction between the flight deck and the rotor downwash, this interaction increases the RMS from 0.2-$0.3U$ to 0.4-$0.5U$. This behavior is consistent with results from the ship only simulations which saw increased RMS fluctuations with negative pitch at SS6, see Figure 28.

77
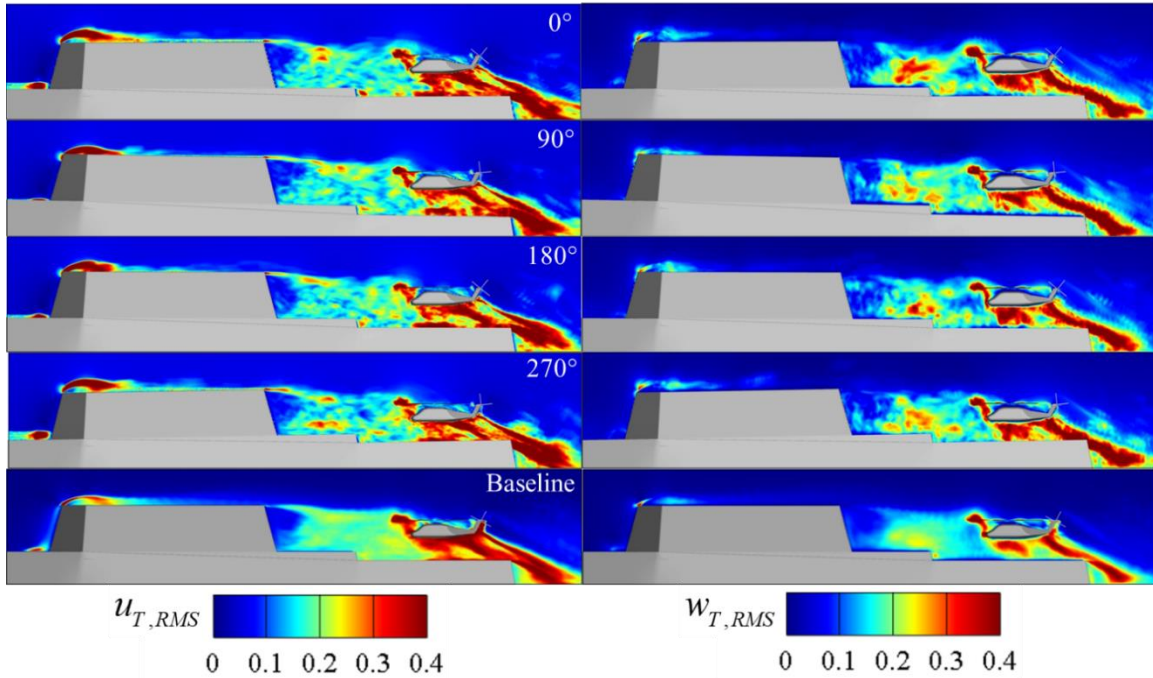
Figure 49: RMS of the phase-locked streamwise (left) and vertical (right) velocity fluctuations for the four quarter phases for SH-60 and ONRT advancing at 15 knots in 15 knots wind in waves with motions (WM/WW/15$_{S+H}$). The total RMS for the baseline condition is shown at the bottom (NM/NW/15$_{S+H}$).
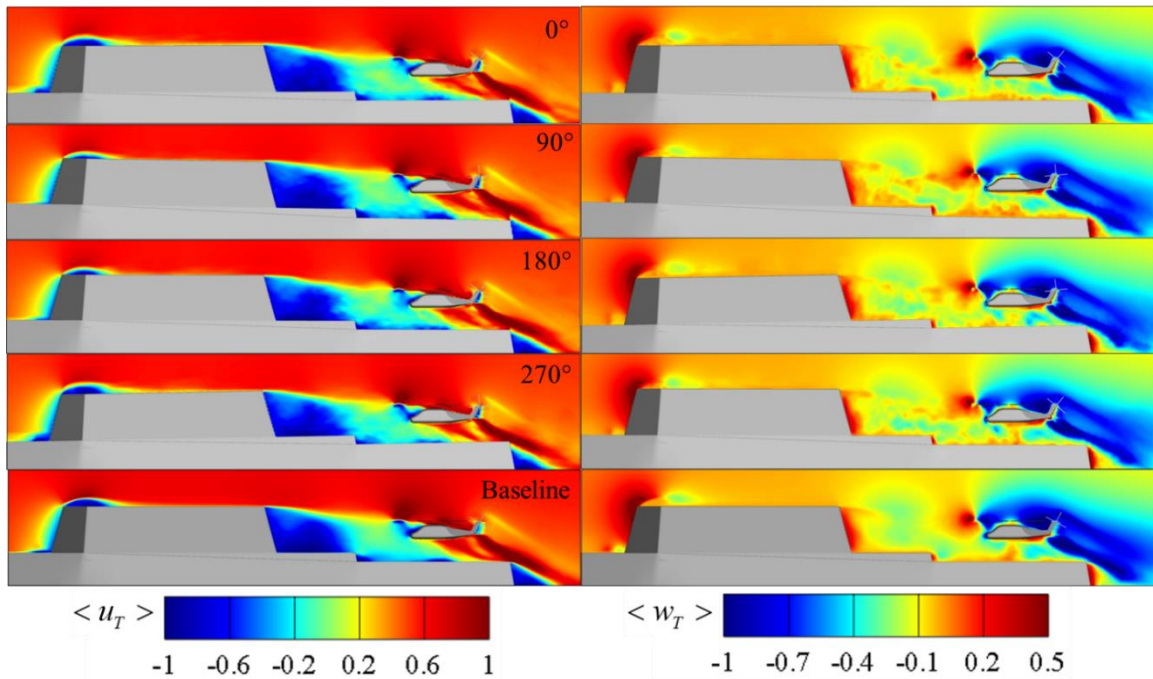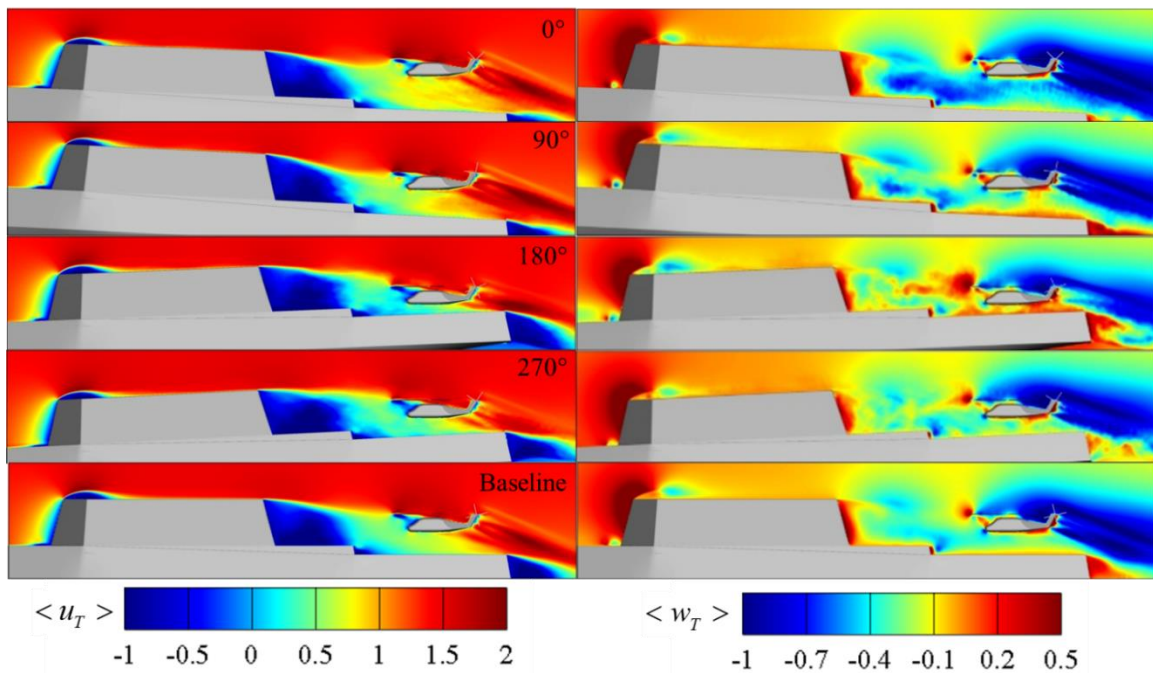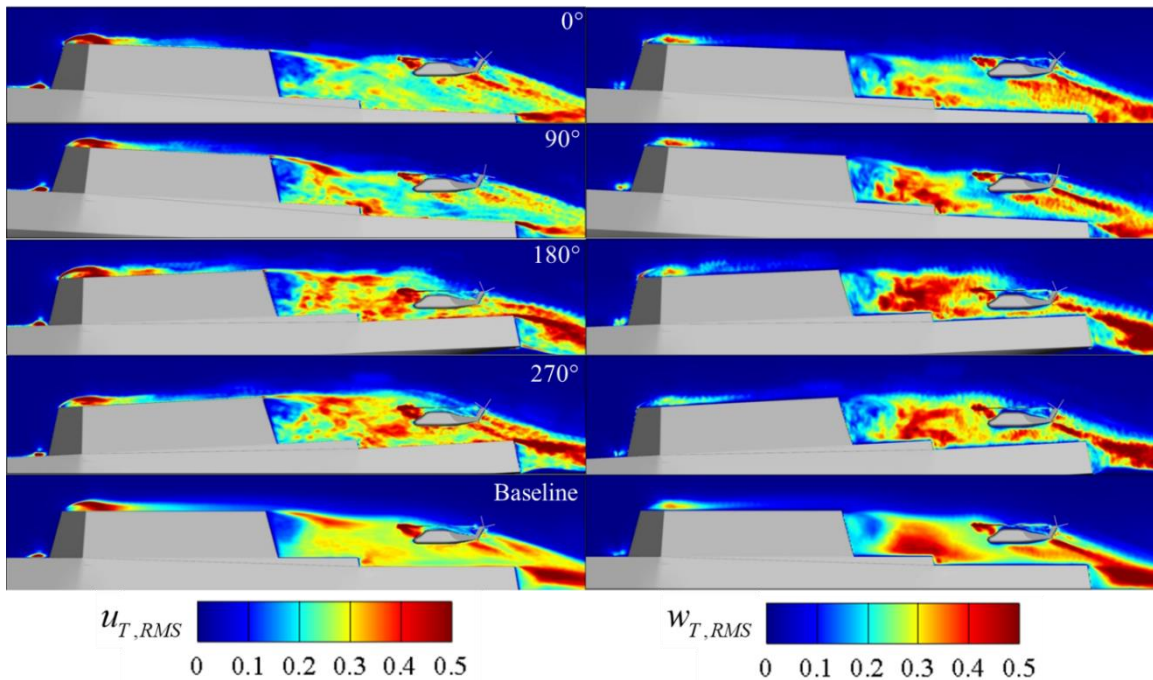

Figure 50: RMS of the phase-locked streamwise (left) and vertical (right) velocity fluctuations for the four quarter phases for SH-60 and ONRT advancing at 15 knots in 35 knots wind in waves with motions (WM/WW/35$_{S+H}$). The total RMS for the baseline condition is shown at the bottom (NM/NW/35$_{S+H}$).

78

Figure 51 shows the changes in mean streamwise and vertical velocities and the RMS of their fluctuations at two cross section x/L=0.8 (in the flight deck upstream of the helicopter) and x/L=0.98 (slightly upstream of the stern) for cases with the helicopter with respect to the cases without the helicopter in calm water and SS6 waves. As expected, the presence of the helicopter results in massive changes downstream at the stern (x/L=0.98), affecting the mean streamwise and vertical velocities by ± 80% and 100% of the reference velocity (U=25 knots), respectively. The main effects of the presence of the helicopter on the velocity field upstream of the aircraft is a reduction or reversal of the mean streamwise velocity, as previously discussed in reference to Figures 24 and 48, which reaches $0.3U$, and an increase of the mean vertical velocity reaching about $0.2U$. This change in vertical velocity is caused by the suction of the rotor and decreases the downflow significantly on the center plane at x/L=0.6. The RMS of the velocity fluctuations increase by approximately $0.1U$ and $0.2U$ for the streamwise and vertical components, respectively, or about 30%, see Figures 28 and 50. With the addition of motions and waves the increased vertical velocity in front of the helicopter rotor diffuses further into the regions outside of the deck. Also, increased levels of RMS fluctuations in the streamwise direction are generated by the pumping of the ships flight deck, these can be seen interacting with the fluctuations generated by the main rotor blade. The main change in the flow downstream of the helicopter is the increase in size of flow features, showing that the flow induced by the rotors moves with the ship motions and waves.
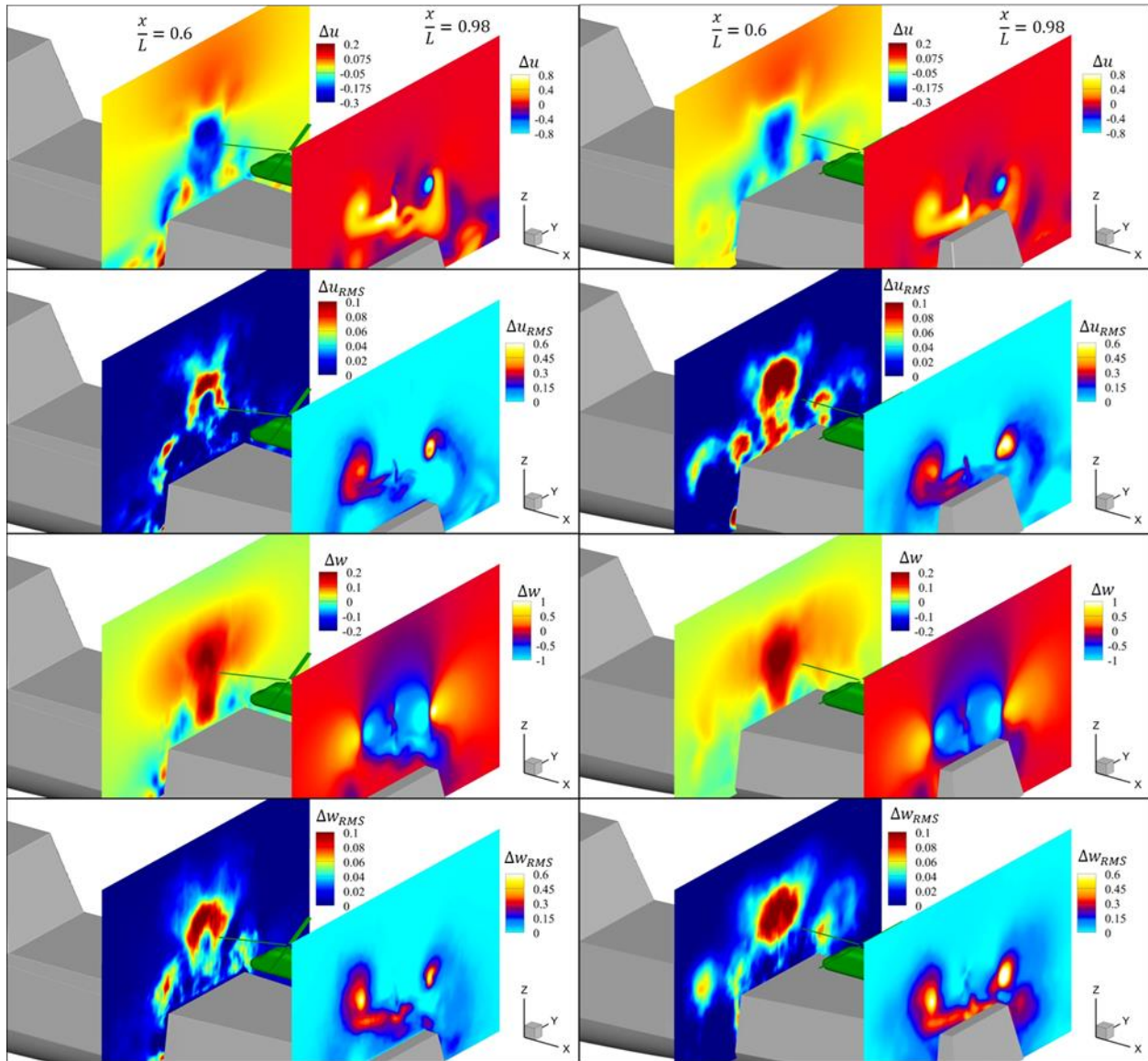
Figure 51: Differences in mean velocities and RMS of their fluctuations for cases with helicopter respect to the cases without helicopter in calm water (NM/NW/35$_{S+H}$, NM/NW/35$_S$, left) and in SS6 waves (WM/WW/35$_{S+H}$, WM/WW/35$_S$, right).

5.3.2 Forces on the helicopter body

Integrated forces over the entire helicopter body and a time history of these values for a period equivalent to one wave encounter period are shown in Figures 52 and 53 for SS3 and SS6, respectively. The figures include the forces for the helicopter only (NM/NW/XX$_H$), no motions or waves (NM/NW/XX$_{S+H}$), and with motions and waves (WM/WW/XX$_{S+H}$) cases. The black line is an instantaneous time history and the red line is a moving average of the same signal with

80

a period approximately equivalent to the blade passage period in order to highlight the lower

frequency force fluctuations that are more likely to affect the control of the aircraft.
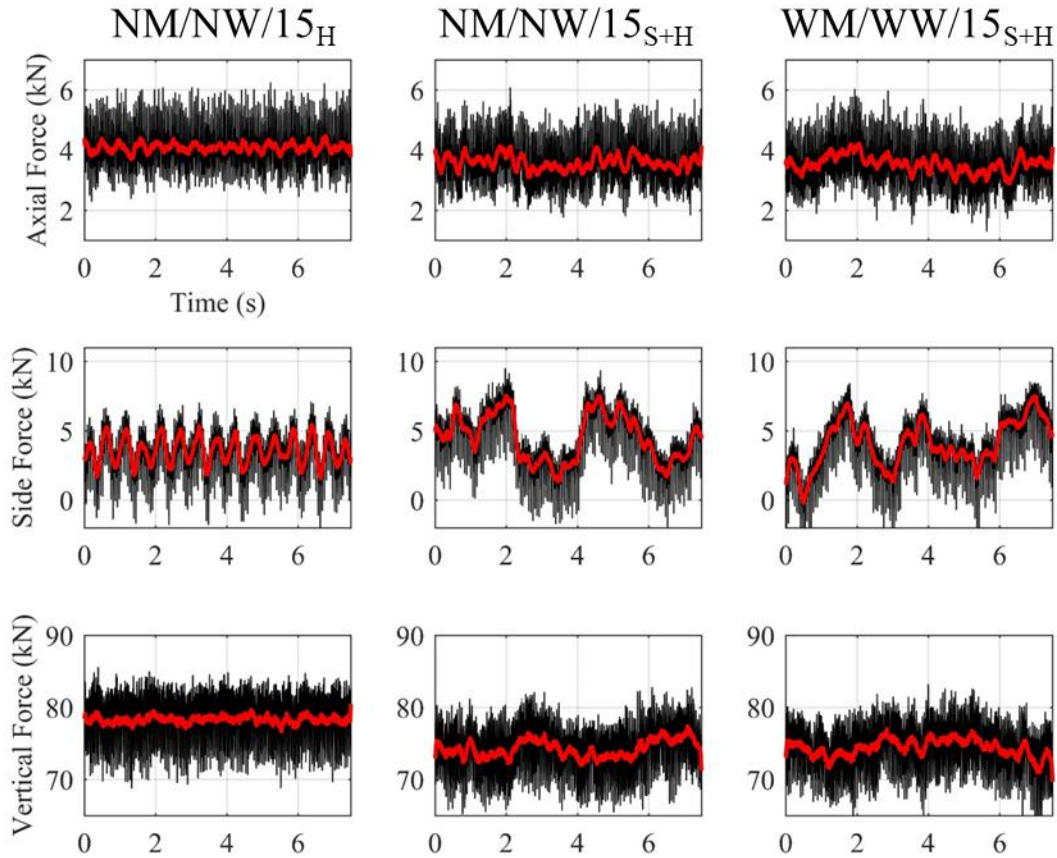
Figure 52: Instantaneous forces on helicopter for ONRT and/or SH-60 advancing at 15 knots in 35 knots head winds for all cases. Time period is equal to the wave encounter period.
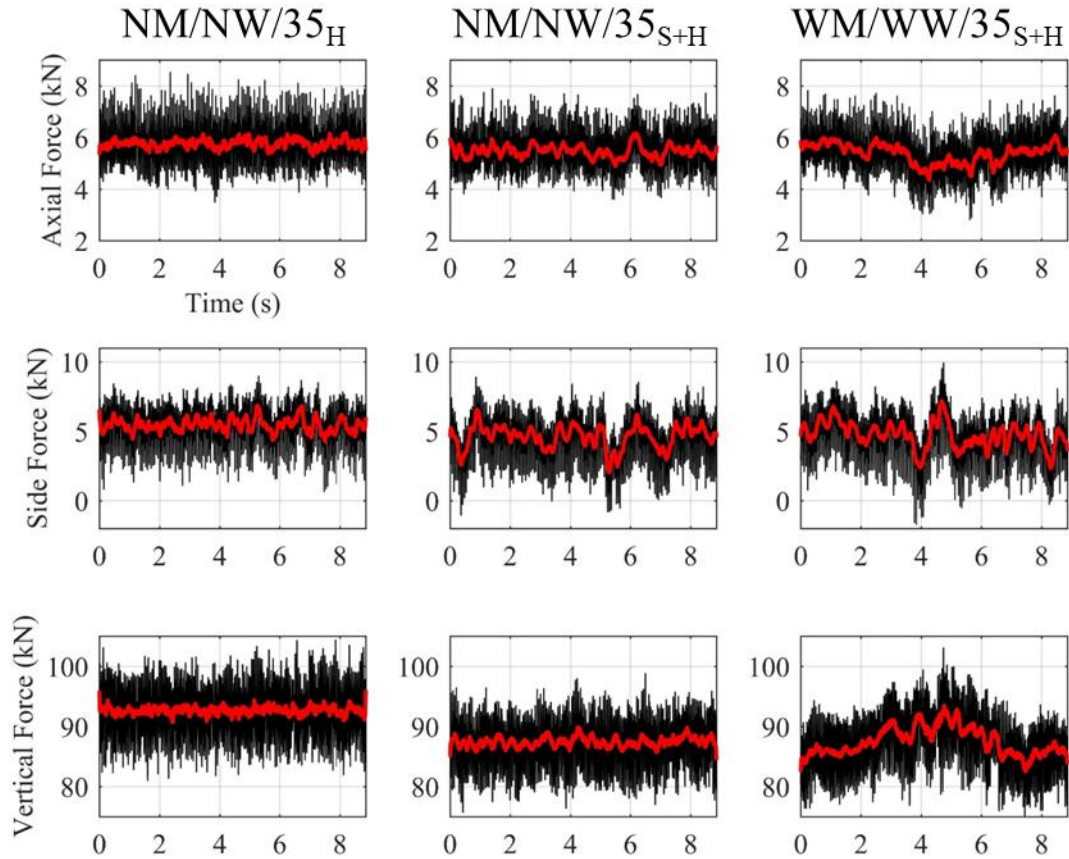
Figure 53: Instantaneous forces on helicopter for ONRT and/or SH-60 advancing at 15 knots in 35 knots head winds for all cases. Time period is equal to the wave encounter period.

Instantaneous views of the flow field for the helicopter advancing at 30 and 50 knots are shown in Figure 54. The lift is higher on the starboard side of the helicopter, as the blade is moving forward on that side and thus the relative velocity is higher. As expected, the effect increases with helicopter speed. At the lower speed, vortices shed from the starboard high-lift side of the rotor periodically cross the nose of the fuselage and are responsible for the low-frequency side and axial force fluctuations shown in Figure 52 for helicopter only condition. The vortices appear to break down sporadically when the helicopter is operating over the flight deck of the ONRT, strong low frequency fluctuations are still present but are not as steady and is assumed to be a result of the interaction with the turbulent airwake. These vortices are not present in the condition of higher speed operation for any of the cases.

82
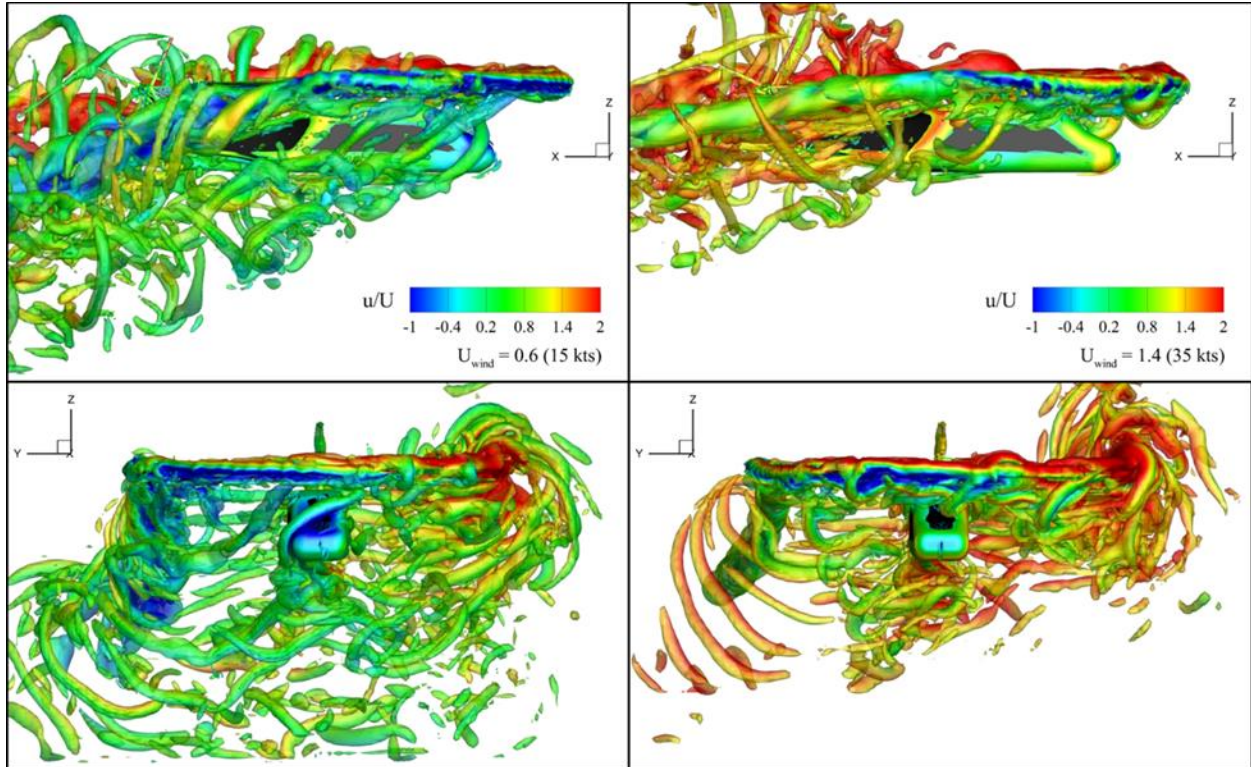
Figure 54: Side (top) and front (bottom) views of helicopter advancing at 15 knots into 15 knots (NM/NW/15$_H$, left) and 35 knots (NM/NW/35$_H$, right) winds. Vortical structures shown as iso-surfaces of $Q = 20000$.

Table 11 lists the mean and RMS values of the forces shown in Figures 52 and 53, the moving average of the signal was used to compute these statistics in order to exclude the contribution from higher frequency vibrational fluctuations. Both the 15 and 30 knots wind speed conditions show an increase in the thrust produced by the helicopter for the condition when the helicopter is not operating in uniform incoming flow. The vertical velocity behind the superstructure of the ship is negative in average, this leads to a more positive advance coefficient (J, Equation 17) when operating behind the ship. The average vertical force for the cases with the ONRT decreases by approximately 5% for both wind speed conditions. The effect of a higher advance coefficient is shown by the performance curve in Figure 41. With the addition of motions, the RMS of the vertical force fluctuations increases for both the SS3 (WM/WW/15$_{S+H}$) and SS6 (WM/WW/35$_{S+H}$) conditions. The effect is much more significant for the higher sea

state condition with the vertical force RMS increasing from 0.58 kN to 2.61 kN. Overall, both

cases show the same trend, the RMS fluctuations of forces in all directions increases when

operating in the airwake of the ONRT and this increase is amplified with the addition of motions.

Table 11: Average and RMS of the forces on the helicopter body in all direction for all the cases with helicopter.

Wind	Case	Stat	Axial Force (kN)	Side Force (kN)	Vertical Force (kN)
15 knots	NM/NW/15$_{S+H}$	Mean	3.60	4.95	73.84
		RMS	0.24	1.53	1.04
	WM/WW/15$_{S+H}$	Mean	3.56	4.65	74.03
		RMS	0.27	1.46	1.13
	NM/NW/15$_H$	Mean	4.09	3.57	78.28
		RMS	0.13	0.93	0.46
35 knots	NM/NW/35$_{S+H}$	Mean	5.45	4.66	87.10
		RMS	0.23	1.02	0.99
	WM/WW/35$_{S+H}$	Mean	5.37	4.61	87.67
		RMS	0.37	1.10	2.61
	NM/NW/35$_H$	Mean	5.76	5.46	92.64
		RMS	0.15	0.46	0.58

Figure 55 and 56 show spectrum of the dimensionless forces normalized by the helicopter

weight (F_i/W_0) for the three conditions and both wind speeds. Both SS3 and SS6 cases with

motions and waves show a clear peak at the wave encounter frequency for all forces in both

conditions. The additional low frequency content shown in the side force for SS3 is believed to

originate from the breakdown of the phenomenon shown in Figure 54 and discussed previously.

Clear peaks are also present at the blade passage frequency, four times the main rotor frequency,

and two and three times the blade passage frequency. The main peak at the blade passage

frequency is due to the large change in thrust as the blades experience a decrease in velocity

relative to the wind as they pass from starboard to port, which occurs once per rotation per blade.

This effect is the strongest in the vertical direction as expected. The peak at twice the blade

passage frequency is due to changes in thrust as the blades navigate through the wake of the ship

and the tail rotor, producing a second force fluctuations occurring once per rotation per blade, but approximately 90 degrees out of phase with the fluctuations previously described. The peak at three times the blade passage is due to the tail rotor that rotates at three times the main rotor frequency and is the strongest in the side-to-side direction. Higher harmonics are also present with decaying amplitude, as shown in Figure 57, likely caused by higher-order interactions between the main and tail rotors. For instance, there are four main rotor blades crossing the tip vortices of the tail rotor per main rotor rotation, while there are 12 instances of the tail rotor blades crossing the main rotor tip vortices in the same period, resulting in a peak at 16 times the main rotor frequency, present in both Figures 55 and 56.
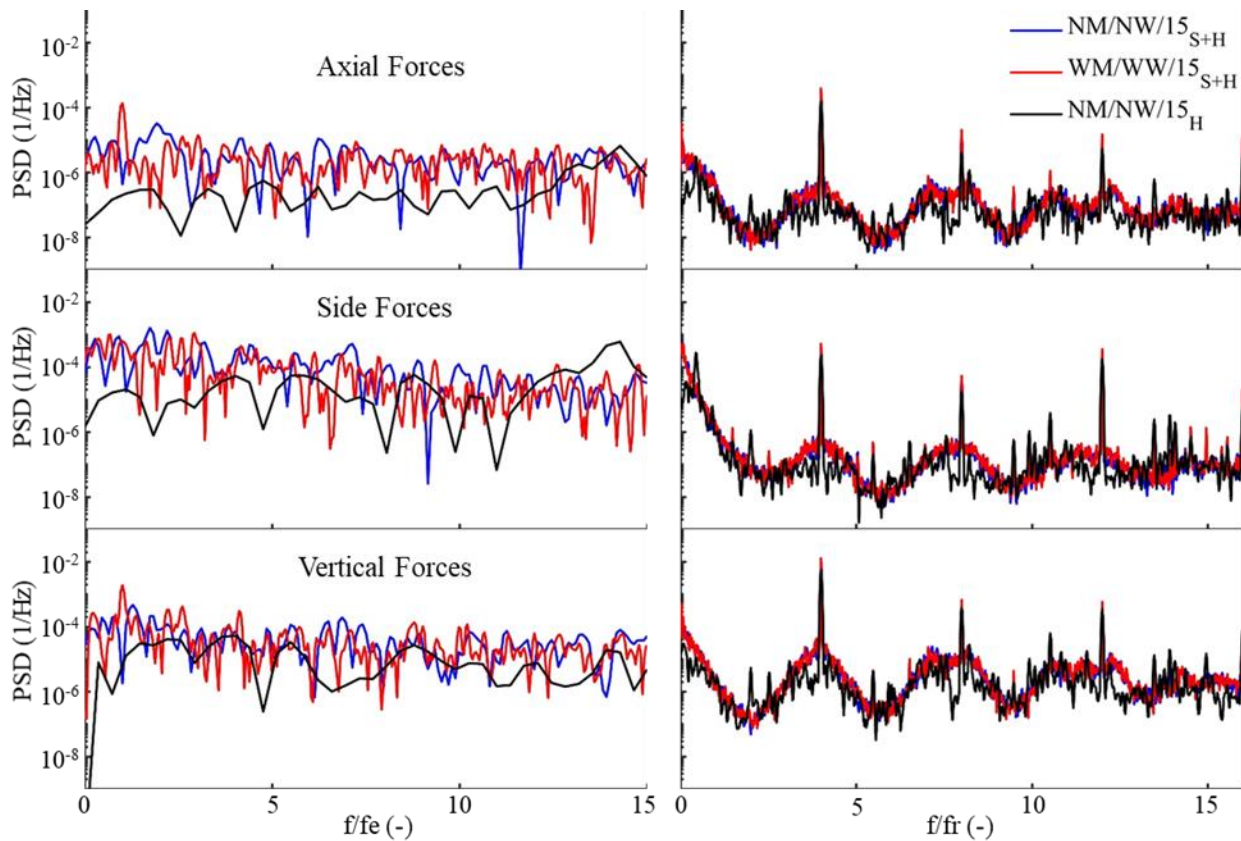
Figure 55: Power spectral density of all forces in SS3 condition (NM/NW/15$_{S+H}$, WM/WW/15$_{S+H}$, NM/NW/15$_H$). The frequency for the plots on the left is normalized by the wave encounter frequency, and by the main rotor rotational frequency for the plots on the right.
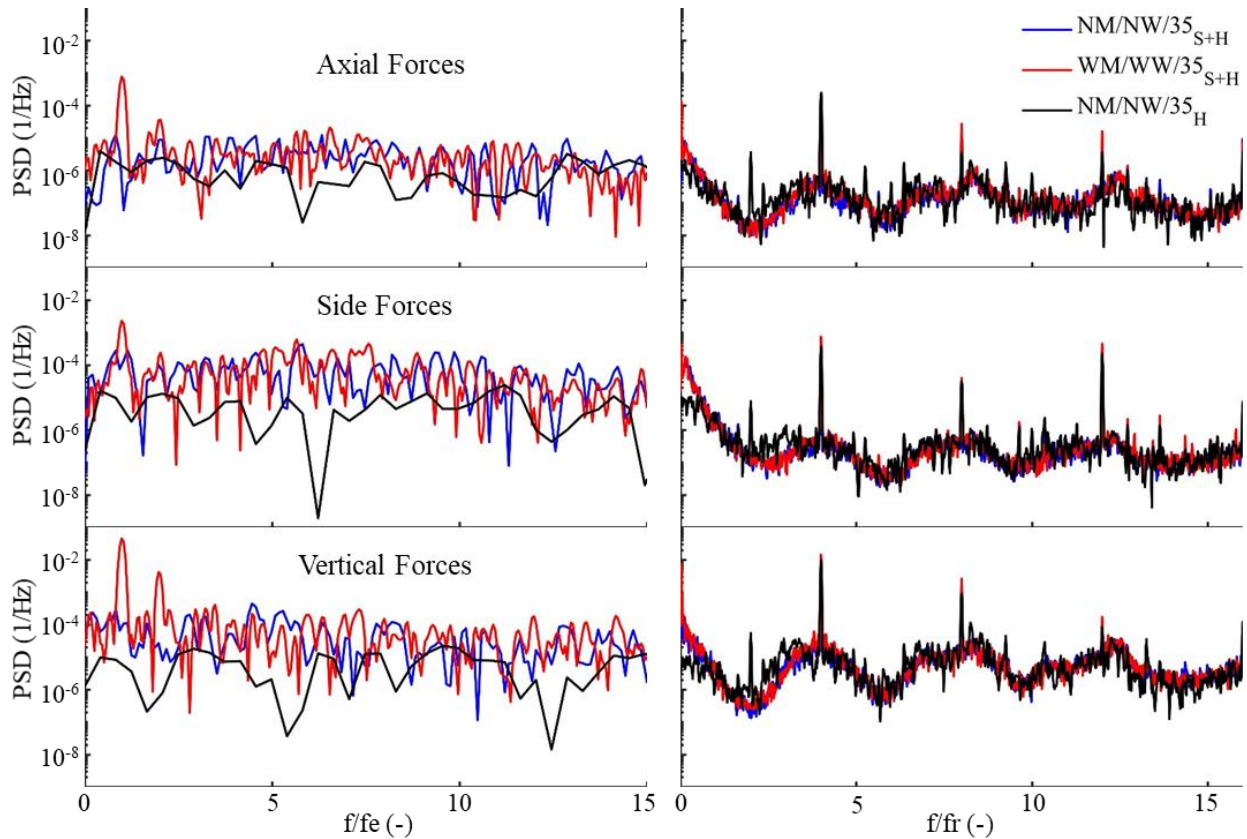
Figure 56: Power spectral density of all forces in SS6 condition (NM/NW/35$_{S+H}$, WM/WW/35$_{S+H}$, NM/NW/35$_H$). The frequency for the plots on the left is normalized by the wave encounter frequency, and by the main rotor rotational frequency for the plots on the right.

The broadband turbulence of the airwake is shown as a decaying tail from approximately 0.5 to 10 Hz in Figure 57. Higher frequencies associated with smaller vortices, affect less of the total helicopter force and decay quickly at 60 dB/decade, or an exponent of -3.4. Interactions of the blades with larger vortices from the airwake and the helicopter main rotor itself (Hariharan et al. 2014) results in a variety of frequencies around the blade passage frequency and its higher harmonics previously discussed. These interactions quickly decay at higher frequencies. Overall, the difference between SS3 (WM/WW/15$_{S+H}$) and SS6 (WM/WW/35$_{S+H}$) are only significantly different at frequencies lower the start of the linear decay at 0.5 Hz. The effect from the larger waves of SS6 is reflected in the higher amplitude response at the first harmonic of the encounter frequency when compared to SS3. Also, the increase in side force low frequency content for the

SS3 condition due to the interaction of structures shed from the main rotor and the fuselage (see

Figure 54) is clearly visible.
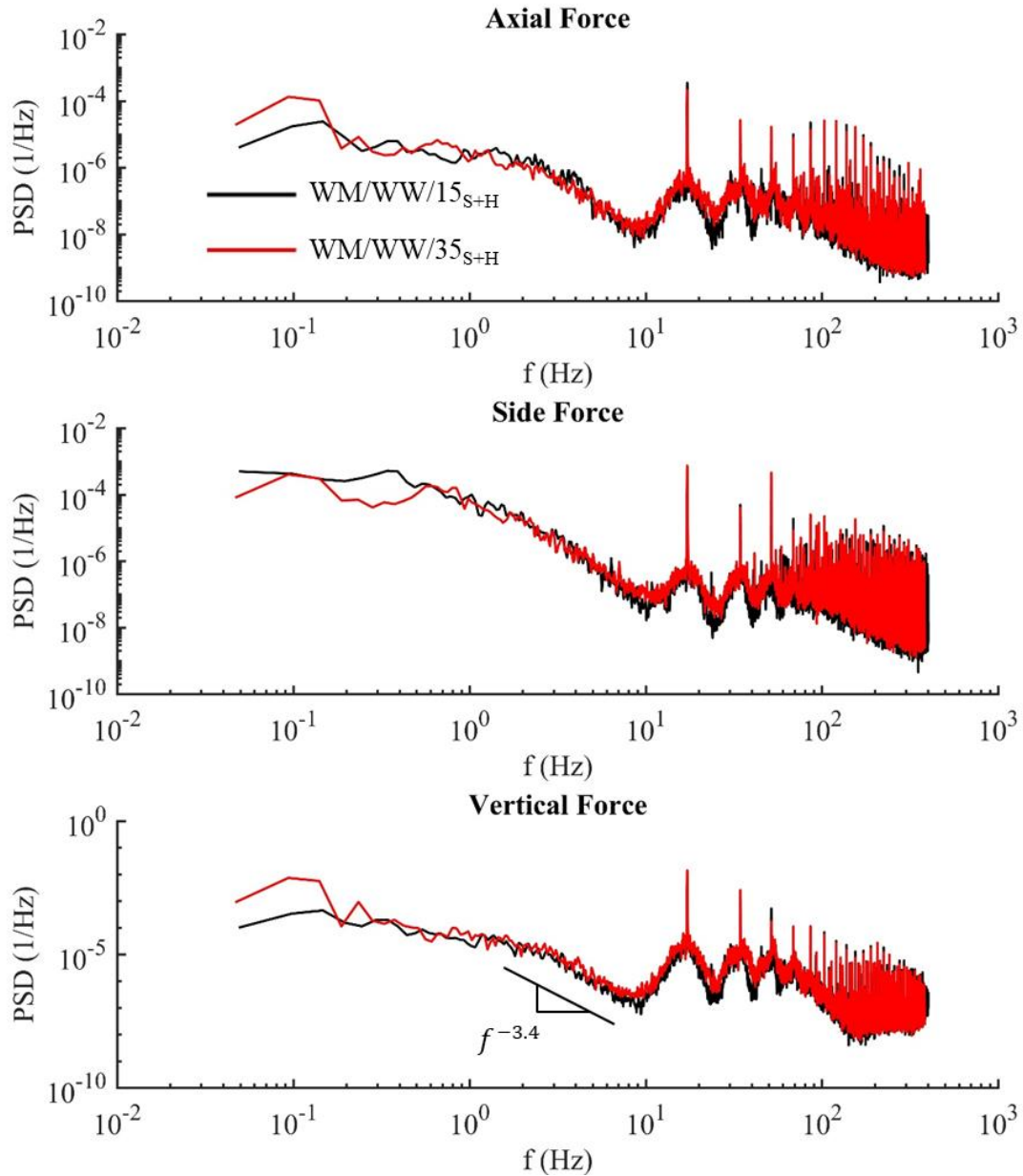
Figure 57: Power spectral desnity for all the forces on the heclicopter body for the SS3 and SS6 coniditons (WM/WW/15$_{S+H}$ and WM/WW/35$_{S+H}$).

5.4 One-way vs. Two-way Coupling

As previously discussed, and shown in Figure 51 the downwash for the fully discretized helicopter rotor in the two-way coupling approach significantly modifies the airwake over the flight deck of ONRT. Figure 58 shows the frequency response of the normalized thrust of the one-way (actuator disk) and two-way (discretized rotors and fuselage) coupling approaches when operating in the airwake of the ONRT advancing at 15 knots in 35 knots head wind and SS6 waves ($WM/WW/35_S$ and $WM/WW/35_{S+H}$). The figure shows that the one-way coupling approach is able to recover the strong response seen at the wave encounter frequency (0.113 Hz) as well as the second harmonic, both shown in the response of the two-way coupling approach. The magnitudes of these responses are under predicted by the one-way coupling approach and is assumed to be a result of the effect the streamwise flow has on the angle of attack for the blades that is not accounted for. When the flight deck is moving up the shear layer contracts exposing the blades to higher streamwise velocities increasing the thrust produced, any response from this is not accounted for in the one-way coupling approach. Moving to higher frequencies the one-way coupling model can be seen decaying much quicker in spectral energy than the two-way coupling approach. At 2 Hz, which is at the high end of the frequency range expected to affect pilot workload (Thedin et al. 2018), the response seen in the two-way coupling is two orders of magnitude greater than the response from the one-way coupling approach. As mentioned previously, Figure 46 shows vortical structures generated by the ONRT superstructure being ingested by the main rotor of the helicopter periodically in the two-way coupling approach, it is believed that this interaction accounts for some of the increase in low frequency response. The two-way coupling model also includes a fully discretized fuselage and tail rotor so any interactions between the ship airwake wake and these geometries and the flow induced by them is not accounted for in the one-way coupling approach.
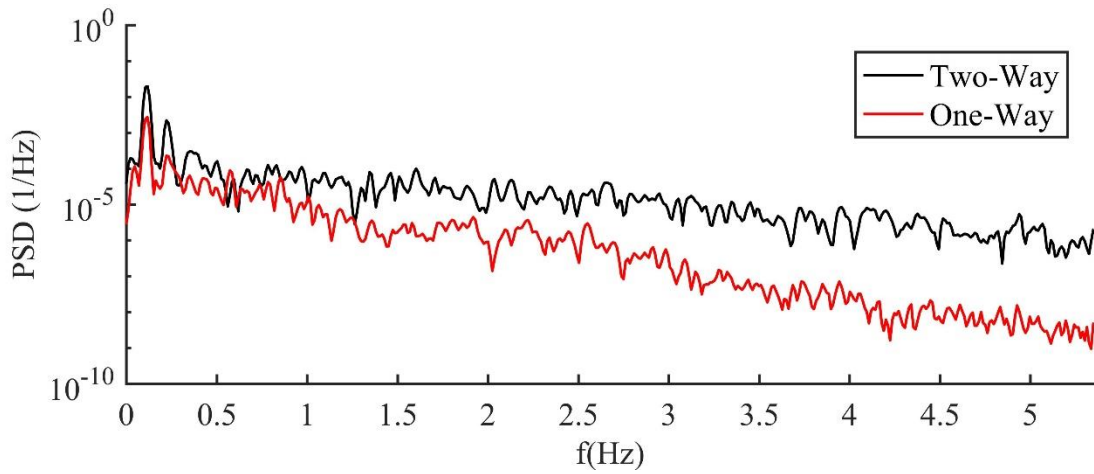
88

Figure 58: Frequency response of thrust coefficient T/T_0 for the one-way and two-way coupling approaches. Both are for the ONRT advancing at 15 knots in 35 knots head wind (WM/WW/35_S and WM/WW/35_{S+H}).

Chapter 6. CONCLUSIONS AND FUTURE WORK

6.1 Summary of Conclusions

Static single-phase simulations were conducted in order to characterize the effect of Reynolds number on the airwake of the ONR Tumblehome geometry and measure the accuracy of the CFD simulations. By analyzing the flow at a low Reynolds number (Re=$3.2x10^4$) robust flow structures were identified in the regions of flow separation at the front of the superstructure as well as behind each of the back-facing steps in the aft region of the ONRT which are mostly maintained at higher Reynolds numbers. It was shown that as the grid system is refined the level of small-scale structures that are resolved increases significantly, causing these robust structures to break down faster than those seen in the coarse grid system, resulting in differences in the mean flow structures between grids. The results from the Reynolds number analysis showed that the low Reynolds airwake has significant differences compared to the model-scale (Re=$1x10^6$) and full-scale (Re=$1.3x10^8$) in the recirculation zone and shear layer behind the superstructure of the ONRT. In the mid-flight deck region (*x/L*=0.883) mean velocity and fluctuations were very similar across all Reynolds numbers tested, this area is of particular interest regarding flight operations. Overall, the model-scale and full-scale solutions are very similar with the main difference seen in the region of separation at the front sides of the superstructure. This means that model-scale experiments and simulations have the capability to serve as an accurate representation of the full-scale airwake of the ONRT depending on the specific region of interest.

Model-scale (Re=$1x10^6$) experiments done at the University of Iowa were used to measure the accuracy of the CFD simulations conducted using three different grids with systematic levels of refinement. Qualitative comparison of the mean flow in the region behind the superstructure showed good agreement for all grid sizes, with the largest difference seen in

90

the vertical flow of the recirculation zone which was shown to be highly unsteady and three dimensional. Line plots showed that the CFD results tended to over predict the magnitude of velocity fluctuations measured during experiments, especially in the regions of increased fluctuations (i.e. directly behind superstructure and near shear layer). These differences were almost 50% in some areas, specifically in the vertical direction. It was also shown that in certain areas such as near the shear layer from the superstructure that increased levels of refinement did results in better agreement between CFD and experiments when comparing velocity fluctuations. Lastly, the agreement between CFD and experiments improved significantly in the mid-flight deck region which is where the velocity data from full-scale simulations was used to measure the effect of the airwake on a helicopter.

The effects of motions and waves on the airwake were analyzed for two different sea state conditions, sea state 3 and 6. Effects of motions and waves were separated by performing simulations with and without motions and waves as well as with motions only and waves only. Also, effects of waves and motions were quantified by performing a triple velocity decomposition which separates periodic fluctuations caused by waves and motions from turbulence. Results show that mild wave amplitudes, equivalent to sea sate 3, result in small changes with respect to the airwake of a ship advancing in calm water. At an increased wave amplitude, equivalent to sea state 6, the periodic fluctuations induced by waves and motions increase significantly, resulting in significantly larger fluctuations in the flight deck region, overall. It was also found that for the sea state 6 condition the streamwise velocity fluctuations 30 ft above the flight deck of the ONRT from motions work in counter phase of the fluctuations caused by wave-induced free surface deformation. The same phenomenon was also observed in other aft regions near the superstructure. This could result in the over prediction of low

91

frequency velocity fluctuations in this region if simulations were done with only imposed motions and did not resolve the corresponding free surface waves. For smaller motions such as those seen for the sea state 3 conditions it is most likely acceptable to neglect motions for flow simulators. For the higher sea state 6 conditions effects from the larger amplitude waves and motions should most likely not be ignored for flow simulators. Lastly, a decomposition of the RMS of the velocity fluctuations shows that an approximate RMS magnitude can be found using the linear superposition of the baseline RMS fluctuations and the low frequency RMS fluctuations caused by motions and waves, but does not recover the true magnitude of RMS fluctuations due its non-linear behavior.

One-way and two-way coupling was used to analyze the effects on a helicopter operating in the airwake of the ONRT. The one-way approach models the helicopter as an actuator disk that produces thrust based on a performance curve operating in the airwake which is computed without the helicopter. The study shows that effects of motions and waves for the larger sea state 6 are considerable. Rotors of the size of SH-60 (large), R22 (small) and a drone (very small) were studied, showing that low-frequency fluctuations caused by waves and motions are equally felt by all craft, but higher frequencies due to the airwake are filtered by larger rotors. A comparison of the one-way and two-way approaches shows that the one-way coupling approach under predicts the low frequency response from motions and waves as well as higher frequencies. The one-way approach offers a simple and significant way to approximate the effects from the airwake on the rotor for maneuvering and control strategies. The main effect ignored by the one-way approach is interaction between the rotor and fuselage, which is likely a reasonable approach for the smallest craft but not for the other geometries. The two-way coupling analysis includes simulations of the SH-60 based helicopter alone, and the SH-60 and

92

ONRT in calm water and in sea state 3 and 6 wind and waves. Comparison to the cases without the helicopter show that the presence of the helicopter over the flight deck of the ONRT significantly modifies the airwake. When operating behind the ONRT the helicopter body is subjected to low-frequency force fluctuations caused by motions, waves, and vortices generated by the ship's superstructure, these fluctuations decay quickly at higher frequencies. The increase in low-frequency force fluctuations for all cases with the helicopter operating over the flight deck are in the range know to increase pilot work load (0.1-2 Hz). A wide spectrum response around the blade passage frequency (17.2 Hz) and higher harmonics is observed as the blades interact with the mean flow field and the turbulent fluctuations in the wake, resulting in high-frequency force fluctuations that will cause vibrations in the craft.

Overall, simulation of the dynamic interface is very complex and computationally expensive. This study shows that a reduced order model where only the baseline velocity fluctuations are computed and periodic fluctuations due to wave-induced motions are added can produce an accurate representation of the velocity fluctuations which would be resolved by directly computing the flow field in motions and waves. This has the ability to significantly reduce the overall computational expense and complexity of dynamic interface simulations without substantially impacting the accuracy. Also, this study offers some guidelines on what level of motions should be included in pilot simulators and which can be ignored based on their limited impact on the airwake behavior.

6.2 Suggested Future Work

Comparison of experimental data to CFD simulations shows significant differences in the levels of fluctuations seen in the chaotic recirculation region behind the superstructure of the ONRT. All simulations are resolved using the same DDES turbulence model, future simulations

should be done using different turbulence models such as pure LES to determine effects of turbulence modeling in the resulting flow field. The airwake of the ONRT is analyzed for cases with head waves and winds with only pitching and heaving for the cases with motions, future analysis should be done in oblique wind and waves with the introduction of rolling motions as well. Oblique winds will significantly affect the large recirculation zone behind the superstructure as well as the shear layer coming from the top of the superstructure. The same decomposition method presented could be used for the oblique flow cases. The study also concluded that sea state 3 waves could most likely be neglected in flight simulators while sea state 6 waves should be included. Simulations with waves similar to sea state 4 and 5 should be done to offer more specific guidance on a range of sea conditions that will significantly modify the airwake of the ONRT. For the simulations with the helicopter and ONRT the helicopter is fixed at a position over the flight deck, future simulations could be done with the implementation of a flight controller for the helicopter in order to more accurately predict which fluctuations will significantly impact the stability of a hovering aircraft in this region.

REFERENCES

Arney AM, 1994a. FFG-7 ship motion and airwake trial: Part 1: Data processing procedures. *DSTO-TR-0039*, Melbourne, Australia.

Arney AM, 1994b. FFG-7 ship motion and airwake trial. Part 2: removal of ship motion effects from measured airwake data. *DSTO-TR-0093*, Melbourne, Australia.

Buchholz J, Martin JE, Krebill A, Dooley G, Carrica PM, 2018. Structure of a Ship Airwake at Model Scale and Full Scale. *2018 AIAA Aerospace Sci. Meet.*, Kissimmee, FL.

Bhushan S, Xing T, Carrica PM, Stern F, 2009. Model- and full-scale URANS Simulations of Athena resistance, powering and seakeeping, and 5415 maneuvering. J. Ship Res. 53, 179-198

Carrica PM, Wilson, RV, Stern F, 2007a. An unsteady single-phase level set method for viscous free surface flows. *Int. J. Num. Meth. Fluids* 53, 229–256.

Carrica PM, Wilson RV, Noack RW, Stern F, 2007b. Ship motions using single-phase level set with dynamic overset grids. *Comput. Fluids* 36, 1415–1433.

Carrica PM, Huang J, Noack R, Kaushik D, Smith B, Stern F, 2010. Large-scale DES computations of the forward speed diffraction and pitch and heave problems for a surface combatant. *Comput. Fluids* 39, 1095–1111.

Carrica PM, and Li J, 2017. A local vortex tube identification method, *Journal of Fluid Mechanics*.

Chase N, Carrica PM, 2013. CFD Simulations of a Submarine Propeller and Application to Self-Propulsion of a Submarine. *Ocean Eng.* 60, 68-80.

Crozon C, Steijl R, Barakos GN, 2014. Numerical study of helicopter rotors in a ship wake. *J. Aircraft* 51, 1813-1832.

Crozon C, Steijl R, Barakos GN, 2018. Coupled flight dynamics and CFD – demonstration for helicopters in shipborne environment. *The Aeronautical J.* 122, 42-82.

Dooley G, Carrica PM, Martin JE, Krebill A, Buchholz J, 2019. Effects of waves, motions and atmospheric turbulence on ship airwakes. *2019 AIAA Aerospace Sci. Meet.*, San Diego, CA.

Forrest JS, Owen I, 2010. An investigation of ship airwakes using Detached-Eddy Simulation. *Comput. Fluids* 39, 656-673.

Forsythe JR, Lynch CE, Polsky S, Spalart P, 2015. Coupled flight simulator and CFD calculations of ship airwake using HPCMP CREATE-AV Kestrel. *53rd AIAA Aerospace Sci. Meet.*, Kissimmee, FL.

Hariharan N, Egolf A, Sankar L, 2014. Simulation of rotor in hover: current state and challenges. *2014 AIAA SciTech Forum*, National Harbor, MD.

Hunt JCR, Wray A, and Moin P, "Eddies, stream, and convergence zones in turbulent flows," *Center for Turbulence Research Report CTR-S88*.

Lewis EV (Editor), 1989. Principles of Naval Architecture Volume III: Motions in Waves and Controllability. *The Society of Naval Architects and Marine Engineers*, Jersey City, NJ.

Li J & Carrica PM, 2018. An approach to couple velocity/pressure/void fraction in two-phase flows with incompressible liquid and compressible bubbles. *International Journal of Multiphase Flow*, Vol. 102, 2018, pp. 77-94.

Li J, Yuan B, Carrica PM, 2018, Modeling Bubble Entrainment and Transport for Ship Wakes: Progress using Hybrid RANS/LES Methods, *32nd Symposium on Naval Hydrodynamics,* Hamburg, Germany.

Martin JE, Kim Y, Kim DY, Li J, Wilson RV, Carrica PM, 2018, Boundary Layer Transition Models for Naval Applications: Capabilities and Limitations, *32nd Symposium on Naval Hydrodynamics,* Hamburg, Germany.

Menter FR, 1994. Two-Equation Eddy Viscosity Turbulence Models for Engineering Applications. *AIAA J.* 32, 1598-1605.

Noack RW, Boger D, Kunz R, Carrica PM, 2009. Suggar++: An improved general overset grid assembly capability Improved General Overset Grid Assembly Capability, *AIAA Paper 2009-3992*. doi:10.2514/6.2009-3992

Polsky SA, 2002. A computational study of unsteady ship airwake. *40$_{th}$ AIAA Aerospace Sciences Meeting and Exhibit*, Reno, NV.

Polsky SA, Imber R, Czerwiec R, Ghee T, 2007. A Computational and Experimental Determination of the Air Flow around the Landing Deck of a US Navy Destroyer (DDG): Part II. *37th AIAA Fluid Dynamics Conference and Exhibit*, Miami, FL.

Sadat-Hosseini H, Carrica PM, Stern F, Umeda N, Hashimoto H, Yamamura S, Mastuda A, 2011. CFD, system-based and EFD study of ship dynamic instability events: surf riding, periodic motion and broaching. *Ocean Eng*. 38, 88-110

Sydney AJ, Ramsey JP, and Kimmel KR, 2016. Experimental investigation of the turbulent aerodynamic environment produced by a generic ship, *54th AIAA Aerospace Sciences Meeting*, 4-8 January 2016, San Diego, CA. AIAA Paper 2016-1071.

Thedin R, Kinzel MP, Horn JF, Schmitz S, 2018. Coupled simulations of atmospheric turbulence modified ship airwakes and helicopter flight dynamics. *J. Aircraft*. Tokyo 2015: Workshop on CFD in Ship Hydrodynamics, Japan.

Xing T, Carrica PM, Stern F, 2010. Large-Scale RANS and DDES Computations of KVLCC2 at Drift Angle 0 Degree, *CFD Workshop Gothenburg 2010*, Gothenburg, Sweden.

97